A Tunable Collagen Microfiber Platform for Engineered Cardiac Tissue

by

Nicholas J. Kaiser

A dissertation submitted to the faculty of the

Biomedical Engineering graduate program at

Brown University, a joint program in the Division of Biology and

Medicine and the School of Engineering

May 2019

This dissertation by Nicholas J. Kaiser is accepted in its present form by the Biomedical Engineering graduate program, a joint program in the Division of Biology and Medicine and the School of Engineering, as satisfying the dissertation requirements for the degree of Doctor of Philosophy.

Date______________ ____
Kareen L. K. Coulombe, Advisor

Recommended to the Graduate Council

Date______________ ____
Christian Franck, Reader

Date______________ ____
Edith Mathiowitz, Reader

Date______________ ____
Jeffrey R. Morgan, Reader

Date______________ ____
George D. Pins, Reader

Approved by the Graduate Council

Date______________ ____
Andrew G. Campbell, Dean of the Graduate School

CURRICULUM VITAE

Education: **Brown University**, Providence, RI
Ph.D. in Biomedical Engineering, expected May 2019

Boston University, Boston, MA
B.S. in Biomedical Engineering, May 2010

Technical Competencies:

- Assay Development
- Design of Experiments
- Mechanical Characterization
- Collagen Isolation/Processing
- Electron Microscopy
- Mammalian Cell Culture
- Stem Cell Culture
- Primary Cell Isolation
- Immunohistochemistry
- Soft Lithography
- Animal Surgery
- Tissue Dissection
- CAD and FEM
- 3D Printing
- Laser Cutting

Software Competencies:

- MS Office Suite
- MS Project
- MS Visio
- Adobe Illustrator
- MATLAB
- GraphPad Prism
- Design-Expert
- Minitab
- Image-Pro
- ImageJ
- Bluehill (Instron)
- Arduino
- Python
- R
- SolidWorks
- ABAQUS

Industry Experience:

Histogenics **02/2014 – 09/2014**
Process Development Engineer *Waltham, MA*

- Led the development and optimization of a process to manufacture a porous collagen tissue scaffold for an autologous cellular cartilage product
- Designed and executed DOE studies to identify and optimize critical process parameters
- Designed bench top assays to evaluate and characterize collagen scaffold materials
- Trained R&D support staff on the execution of novel assays and protocols
- Designed and implemented an automated image analysis method to collect quantitative data from optical microscopy images
- Authored reports and presentations to communicate process development progress

Organogenesis **07/2012 – 02/2014**
Product Development Engineer I *Canton, MA*

- Developed cell based biologic and medical device products

- Led large scale *in vitro* studies based on mammalian cell and tissue culture
- Utilized advanced DOE methodologies to design efficient experiments
- Developed and implemented novel assays for cell line characterization
- Evaluated outside technologies based on scientific merit and fit-to-business
- Wrote reports and presentations on findings for a variety of audiences
- Executed protocols and collected data following cGMP documentation practices

Allergan **05/2011 – 07/2012**
Associate Biomedical Engineer *Medford, MA*

- Supported R&D and marketing teams with the testing of implantable medical devices
- Interfaced with surgeons, veterinarians, histopathologists, and vendors
- Managed all preclinical study documentation, vendor contracts, and specimens
- Led in the creation of new protocols, reports, and procedures
- Assisted with surgery and sample collection for six large animal studies
- Performed advanced image analysis and mechanical testing of tissues and devices
- Oversaw analyses performed by external and internal laboratory staff

C.R. Bard (now Becton Dickinson) **06/2010 – 05/2011**
Tissue Regeneration Intern *Warwick, RI*

- Designed and implemented novel experimental procedures related to tissue scaffold characterization *in vitro* and *in vivo*
- Oversaw data collection and provided technical support in preclinical and cadaver labs
- Authored reports and presentations to communicate with R&D, marketing, and sales

Academic Projects:

Brown University, Coulombe Lab – Providence, RI
Development of an anisotropic scaffold for cardiac tissue, 09/2014 – Present

- Lead the design, development, and DOE optimization of a blended collagen and fibrin natural polymer hydrogel for cardiac tissue engineering applications
- Lead the design, development, and optimization of a device to produce organized collagen microfiber meshes for tissue engineering and biomaterial applications
- Demonstrate feasibility for a collagen and fibrin tube seeded with cardiomyocytes and endothelial cells for perfusion studies
- Manage the projects of senior undergraduate and Master of Engineering students

Boston University, Wong Lab – Boston, MA
Creating a Tissue Engineered Blood Vessel on a Silk Scaffold, 5/2009 – 5/2010

- Assessed the characteristics of synthesized silk necessary to create a viable platform for mammalian cell growth
- Studied how silk matrix patterns affect mammalian cell growth kinetics
- Assembled microfluidic devices composed of a silicone polymer via soft lithography

- Characterized silk based on molecular structure and mechanical properties

The Broad Institute of MIT and Harvard – Boston, MA
A Systems Biology Approach to Tuberculosis, 9/2009 – 5/2010

- Re-annotated the *M. tuberculosis* genome using data from RNA-sequence analysis
- Designed a conditional random field operon prediction model in Java
- Analyzed and improved the model by comparing operon predictions to findings made by other research groups

Publications:

Kaiser, N.J., Bellows, J.A., Kant, R.J., Coulombe, K.L.K., *Digital Design and Automated Fabrication of Bespoke Collagen Microfiber Scaffolds*, Tissue Engineering Part C, 2019 (in press).

Kaiser, N.J., Kant, R.J., Minor, A.J., Coulombe, K.L.K., *Optimizing Blended Collagen-Fibrin Hydrogels for Cardiac Tissue Engineering with Human iPSC-derived Cardiomyocytes*, ACS Biomaterials Science & Engineering, 2018.

Kaiser, N.J., Munarin, F., Coulombe, K.L.K., *Custom Engineered Tissue Culture Molds from Laser-etched Masters*, Journal of Visualized Experiments, 2018.

Munarin, F., Kaiser, N.J., Kim, T.Y., Choi, B.R., Coulombe, K.L.K., *Laser-Etched Designs for Molding Hydrogel-Based Engineered Tissues*, Tissue Engineering Part C, 2017.

Kaiser, N.J., Coulombe, K.L.K., *Physiologically inspired cardiac scaffolds for tailored in vivo function and heart regeneration*, Biomedical Materials, 2015.

ACKNOWLEDGEMENTS

I would like to thank every current and previous member of the Coulombe lab (as so far, I've met everyone!) for creating a truly wonderful, collaborative work environment that I look forward to being a part of every day. I attribute a great deal of my successes to the help I've received from the members of the Coulombe lab team, especially Jeev, whose confocal mastery has been a key contribution to my most recent publications, Jess, who probably prepared at least half of the collagen meshes evaluated in this thesis with a persistently positive outlook, Fabiola, who always had a spare plate of cardiomyocytes when I needed them most, and Cassady, for always taking ownership of the many lab logistics and operations and helping to guide the Coulombe lab into what it is today. I'd also like to thank all my close friends at Brown, inside and outside of the BME program, who together will surely make me miss Providence as much as I missed Boston five years ago.

To Kareen, I can't thank you enough for your endless guidance and support throughout my research journey over the past five years. You convinced me in our first meeting that you would be an excellent manager and mentor, and you have succeeded in fulfilling that promise every day since.

To my dissertation committee members (Christian Franck, Ph.D., Edith Mathiowitz, Ph.D., Jeffery Morgan, Ph.D., and George Pins, Ph.D.), thank you for all the informed guidance, advice, direction, and time that you so generously contributed to this project. There is no question that this thesis project, as well as my own abilities as a researcher, are greatly improved as a result.

To my mom and dad, it has been a long road to get here and I wouldn't have been able to do it without your endless and unconditional love and support. It was the passion for science that you instilled in me when I was very young that defines who I am today.

Finally, and most importantly, to my wonderful wife Pinar. It's been a wild trip – but we're both now poised to be college graduates, again. Your endless support through all the trials and tribulations (and editing) of this process has made it all possible. I am so grateful to have you in my life – I couldn't have done it without you!

TABLE OF CONTENTS

LIST OF TABLES

LIST OF FIGURES

ABBREVIATIONS

2D – Two Dimensional
3D – Three Dimensional

μg – Micrograms
μL – Microliters
μm – Micrometers

ANOVA – Analysis of Variance
CDM3 – Cardiac Differentiation Media 3
CI – Confidence Interval
CM – Cardiomyocyte
cTnT – Cardiac Troponin T
CVD – Cardiovascular Disease
Cx – Connexin
DAPI - 4′,6-diamidino-2-phenylindole
df – Degrees of Freedom
DMEM – Dulbecco's Modified Eagle Medium
DOE – Design of Experiments
ECM – Extracellular Matrix
F_{max} – Peak Force
GSK3 – Glycogen Synthase Kinase 3
HEPES – 4-(2-hydroxyethyl)-1-piperazineethanesulfonic acid
hESC – Human Embryonic Stem Cells
Hz – Hertz
hiPSC – Human Induced Pluripotent Stem Cells
hiPSC-CMs – Human Induced Pluripotent Stem Cell-Derived Cardiomyocytes
iPSC – Induced Pluripotent Stem Cells
IWP2 – Inhibitor of Wnt Production 2
kPa – Kilopascal
LAD – Left Anterior Descending (Coronary Artery)
LV – Left Ventricle
mg – Milligrams
mL – Milliliters
mm – Millimeters
mM – Millimolar
mN – Millinewtons
MPa – Megapascal
Pa – Pascal

PBS – Phosphate Buffered Saline
PDMS – Polydimethylsiloxane
RPMI – Roswell Park Memorial Institute (Medium)
RSM – Response Surface Methodology
SEM – Standard Error of the Mean
SMA – Smooth Muscle Actin
T_{50} – Time to 50% Relaxation
T_{90} – Time to 90% Relaxation
UTS – Ultimate Tensile Stress
V_{up} – Upstroke Velocity

CHAPTER 1: INTRODUCTION

2.1 Motivation: A global health burden

Affecting 110 million people and resulting in 8.9 million deaths worldwide in 2015 (12.2% of all deaths annually), ischemic heart disease (IHD) is a global problem[1,2]. IHD, which encompasses myocardial infarction (heart attack), angina, and sudden cardiac death, is caused by the development of atherosclerotic plaques that narrow, and sometimes entirely obstruct, coronary arteries. Following an ischemic event, surrounding cardiac tissue is starved of oxygen and essential nutrients typically provided by the flow of blood, and begins to die within minutes, often resulting in permanently decreased cardiac function[3,4]. The ubiquity of this disease has led to therapeutic advancements in a number of areas, including the development of angioplasty and stents designed to restore blood flow to affected coronary arteries as well as pharmacological treatments such as blood thinners, beta blockers, and angiotensin converting enzyme (ACE) inhibitors, which reduce the workload of the heart by lowering blood pressure[5–8]. While all these technologies can be effective in restoring blood flow and preventing further deterioration, they offer no benefit to cardiac tissue that has already died. Indeed, due to the body's own inability to restore cardiac tissue function through normal healing (caused in part by the extremely low proliferation rate of adult cardiomyocytes) and the dearth of restorative cardiac tissue treatments, all loss of function due to IHD is permanent[9]. The resulting decrease to heart function can cause feelings of breathlessness, reduce capacity for exercise and physical exertion, trigger depression, and decrease expected lifespan, thereby significantly reducing quality of life[10–12].

Leveraging recent advances in tissue engineering, stem cell technology, and material science, tissue engineered myocardium presents a compelling treatment option by offering the potential to restore function to a heart damaged by ischemic injury through the replacement of damaged tissue with healthy myocardium grown in vitro. However, there are several obstacles to overcome before engineered myocardium can become an effective therapeutic strategy, including improved alignment of resident cells, increased active force production, and better matching the passive mechanical properties of native myocardium[13–16]. Redesigning the scaffolds used to fabricate these tissues to better emulate the sophisticated mechanics of native myocardium offers a pathway to address these challenges.

Presently, most engineered human cardiac tissues are fabricated by embedding human induced pluripotent stem cell (hiPSC)-derived cardiomyocytes in a simple natural or synthetic polymer hydrogel. While this method is effective in producing beating cardiac tissues, emulation of the properties of native myocardial ECM is extremely limited, and as a result cardiomyocyte alignment is often poor and force production is reduced. More recent and sophisticated approaches have modulated gross tissue shape, creating stress fields during tissue compaction (the process through which resident cells remodel their extracellular matrix around them), in order to promote cardiomyocyte alignment[17–19]. However, this approach either restricts the shape of the cardiac tissue patches to thin strips, which is ill-suited for use over the area of the infarct, or requires the presence of fenestrations, further reducing the effective contractile forces generated by these tissues. Additionally, these simple hydrogel materials typically do not approach the passive stiffness properties of native myocardium.

Herein, we describe a body of work that first identified the roles of extracellular matrix composition and resident cell population on engineered cardiac tissue development and function, then developed and characterized a process for creating engineered cardiac tissues with embedded collagen microfiber meshes that yielded tissues with physiologically relevant mechanical anisotropy. Finally, we characterized the performance of these composite scaffold tissues in comparison to cardiac tissues prepared with the simple hydrogel scaffold format this is used ubiquitously. Through this work, a robust and versatile tissue engineering scaffold platform is realized that promises to advance the landscape of engineered tissue scaffolds for cardiac tissue engineering research and beyond.

2.2 Heart function is dependent on the myocardium

The human heart is composed of four chambers: the left and right atria and the left and right ventricles. The right atrium receives deoxygenated blood from the body through the inferior and superior vena cava and aids in filling the right ventricle. Conversely, the left atrium receives oxygenated blood from the pulmonary vein and aids in filling the left ventricle. During atrial contraction the left and right atria contract, pushing blood through the tricuspid valve on the right side and mitral valve on the left side, filling their respective ventricles. During ventricular contraction the tricuspid and mitral valves close, and deoxygenated blood is pushed through the pulmonary valve on the right side into the pulmonary system and lungs. Simultaneously, ventricular contraction on the left side of the heart pushes oxygenated blood through the aortic valve and into the aorta and the body's circulatory system. The constant work performed by the heart results in significant metabolic demand that is addressed by a vascular network called the coronary arteries, which range in diameter from ~4.5 mm in the large, main branch of the left anterior descending coronary artery (LAD) to ~5 μm in capillary beds[20,21].

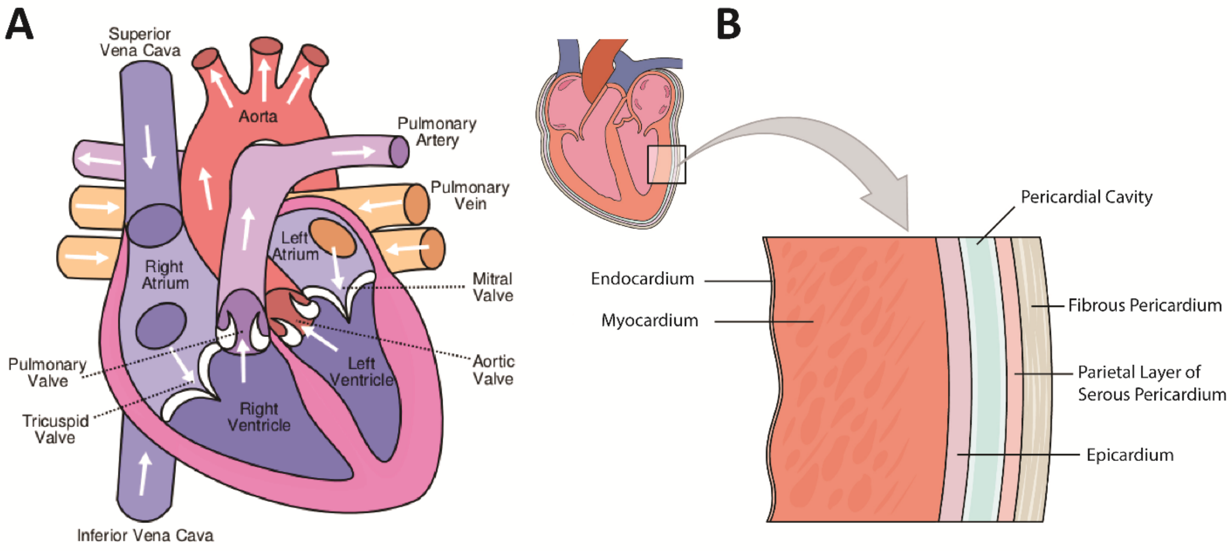

Image by Eric Pierce
Distributed under the GNU Free Documentation 1.2 License

Image by OpenStax College
Distributed under the Creative Commons Attribution 3.0 License

Figure 1. 1: Anatomy of the human heart. (A) Macroscopic cross section highlighting the chambers and valves of the human heart. (B) Microscale cross section highlighting the tissue layers that compose the heart wall and pericardium.

The heart wall that defines the four heart chambers is composed of three distinct tissue layers called the epicardium, the myocardium, and the endocardium[22] (Fig. 1.1). These layers are surrounded by additional layers of tissue that comprise the pericardium, which can be separated into the serous and fibrous pericardium. The epicardium is a thin outer layer composed primarily of connective tissue and fat, which serves to protect the heart from contact with the surrounding pericardial sac[23]. Conversely, the endocardium is the innermost layer of the heart wall, lining the chambers of the heart, and acting as a barrier in a similar fashion to the endothelium of the vascular system[24]. Between these layers, and comprising the majority of the wall thickness (total thickness ranging from 12 mm to 15 mm in the left ventricle of healthy adults, measured at the obtuse margin 1.5 cm below the mitral annulus[22]), lies the myocardium, which is responsible for generating the contractile forces that drive blood through the heart.

2.3 Myocardial structure and composition drive function

Native myocardium features a high degree of structural organization in all three dimensions that is critical to its function. A single, planar section of myocardium is composed of a dense network of cardiomyocytes connected directly to their neighbors via gap junctions. Each adult cardiomyocyte is roughly rectangular in shape, featuring a ~5:1 aspect ratio, with overall dimensions of ~20 µm x ~120 µm[22]. Ion exchange through the gap junctions of adjacent cardiomyocytes (and initiated by specialized pacemaker cells) is responsible for electrical activation in the form of depolarization, early repolarization, plateau, and repolarization which orchestrate contractile function[25]. Together, native cardiomyocytes form an electrically conductive network through gap junction connections to adjacent cardiomyocytes to generate contractile forces in a synchronized fashion.

Individual cardiomyocyte cells are surrounded by a connective tissue matrix called the endomysium, which aids the intercalated discs in attaching adjacent cardiomyocytes together[26]. Groups of aligned myocytes are further surrounded by the perimysium, an intricate, aligned meshwork composed of fibrous collagen that aggregates myocytes into myofibrils[27]. Finally, the perimysium is surrounded by another fibrous collagen network, called the epimysium, which aggregates myofibrils[28]. Together, these matrix components form a macroscopic material with a high degree of both structural and mechanical anisotropy. As a result, native adult rat myocardium has a tensile stiffness in the long fiber direction of approximately 30 kPa, and a tensile stiffness in the short fiber direction of approximately 15 kPa[29]. Adult myocardium has been found to generate forces on the order of 56.4±4.4 mN/mm^2 in rats and 44.0±11.7 mN/mm^2 in humans[30].

Importantly, these myocardial subsections are further organized into the macrostructure of the heart wall with respect to cardiomyocyte alignment. Cardiomyocyte and extracellular matrix fiber alignment in the heart wall together follow a spiral orientation starting at the apex of the heart and broadening towards the base. This alignment additionally gradually transitions when moving radially out from a chamber of the heart, through the thickness of the heart wall. This sophisticated directionality enables the heart to effect a macroscopic torsion similar to the wringing of a towel, maximizing ejection of blood from the left ventricle[31–33]. However, the tissue death and restructuring associated with ischemic heart disease disrupts this contractile action, further reducing heart function beyond the simple loss of functional cardiomyocytes[34–36].

2.4 Ischemic heart disease inhibits myocardial function

An ischemic event occurs when one of the coronary arteries becomes partially blocked or completely obstructed, typically due to the accumulation and rupture of coronary plaques[37,38]. The resulting blockage or restriction starves the surrounding tissue of blood (and therefore oxygen and glucose) resulting in rapid tissue death[39,40]. If the blockage is not cleared within as little as 20 minutes, a portion of the heart may become necrotic[41]. Over time the reduction in heart function due to death of the contractile cardiomyocytes is amplified by fibroblast infiltration into the ischemic region, followed by disorganized collagen deposition and the development of fibrotic scar tissue[42]. The loss of fibrous architecture resulting from scar development, as well as the stiff mechanical properties of the scar itself, together inhibit the sophisticated macrocontractile motion of the healthy heart, reducing the blood pumping efficiency of the heart, and thereby forcing the remaining heart tissue to work harder to maintain physiological homeostasis.

Rapid therapeutic interventions to remove the blockage or restriction responsible for the ischemic event, such as angioplasty, can ameliorate some of the damage that would otherwise occur, rescuing some of the threatened tissue. However, there is now clear evidence that some cell death following an ischemic event treated with angioplasty can be attributed to the circumstances of the therapeutic intervention itself[43–46]. Following establishment of the occlusion or restriction, downstream tissues become hypoxic, blood and tissue pH decreases, and systolic calcium levels become dysregulated[46]. Upon sudden removal of the occlusion or restriction, oxygenated blood immediately flows in to the previously hypoxic tissue, causing a sudden increase in blood and tissue pH, further dysregulation of calcium levels, and the production of reactive oxygen species[46]. These factors, as well as secondary effects related to the activation of apoptotic pathways, cytokine signaling via protein kinases, inflammation, and even epigenetic changes are called “reperfusion injury” and are responsible for the cell and tissue death that occurs as a result of angioplasty[46]. While there is no question that the total benefit angioplasty offers outweighs these negative side effects, these consequences eliminate the possibility of complete recovery when using this therapeutic approach.

Ischemic events can occur in tissue composing any chamber of the heart, but the vast majority of ischemic events occur in the left ventricle[47]. This is attributed to the greater size of the left ventricle relative to other chambers of the heart due to its outsized role in delivering blood to the body’s circulatory system, as well as the geometry of the coronary arteries which favors the right ventricle with collateral vasculature from the left coronary system[48]. For this reason, most academic research studying myocardial infarction in order to better understand the disease or for the development of therapeutics, focuses on models of left ventricular ischemia. Complete restoration of heart function in most patients who have suffered from IHD will require rescue and/or replacement of damaged left ventricular myocardial tissue.

2.5 Cardiac tissue engineering as a regenerative therapy

Due to the broad impact of IHD and the body's inability to regenerate or restore healthy heart tissue on its own, few diseases present a better target for the development of tissue engineered therapeutics than ischemic heart disease. For this reason, there has been an abundance of tissue engineering research focused on addressing this need over the past three decades[14,18,49–52]. Development in all aspects of the cells + scaffolds + signaling factors tissue engineering paradigm, as it relates to cardiac tissue fabrication, has led to great advances in the field. Within the past 10 years the development of induced pluripotent stem cell (iPSC) technology, as well as advances in the fields of stem cell differentiation and personalized medicine have created a feasible pathway for the fabrication of personalized, replacement cardiac tissue that could one day be used in the clinic[53–57]. Materials and methods research for creating cardiac tissue scaffolds has greatly expanded the variety and tunability of tissue platforms available to researchers, enabling more sophisticated control over tissue organization and mechanics[50,58–62]. Finally, improved understanding of cardiomyocyte signaling and maturation pathways has led to more refined approaches to direct cardiomyocyte phenotype[63–66]. Together, research progress from these subfields forms a robust toolset for designing and studying engineered cardiac tissues.

2.6 Sources of cardiomyocytes

Adult cardiomyocytes have an extremely low rate of growth and expansion (in vivo replacement rates as low as ~1%/year have been reported for humans over age 20[67–69]), such that expansion from a primarily cell source is impractical. For study in vitro, this leaves two options: isolation from a readily available source of young cardiomyocytes (such as fetal sources) or differentiation of cardiomyocytes from a stem cell source.

Neonatal rat hearts offer a readily available primary source of rat cardiomyocytes, and as a result a large body of cardiac tissue engineering research using these cells has been published. However, the utility of this cell source is limited, including the low expansion rate of these cells in culture, the logistical challenges related to maintaining a breeding colony as a source of rat pups, and most importantly, the lack of a clear translational path for the development of human therapeutics in the future.

Generation of cardiomyocytes from stem cells, first human embryonic stem cells (hESCs) and later induced pluripotent stem cells (iPSCs), addresses all of the aforementioned problems. Stem cell populations can be rapidly expanded prior to differentiation, enabling the production of hundreds of millions of cardiomyocytes from approximately 1 million iPSCs in less than 4 weeks[53,63]. Additionally, iPSC populations can be dedifferentiated from accessible donor sources, such as fibroblasts from a skin biopsy[70,71] or even renal epithelial cells from a urine sample[72–74], representing an autologous cell source that could be used therapeutically without further modification. A number of processes have been developed for the differentiation of cardiomyocytes from stem cell sources, and these can broadly be divided into the categories of co-culture with mouse visceral endoderm-like (END-2) stromal cells, embryoid body differentiation in suspension culture, and 2D monolayer differentiation[75]. All protocols emulate the developmental pathway of first inducing mesodermal differentiation, followed by commitment to the cardiac lineage[76,77], but differ in their strategies to influence the signaling pathways that direct differentiation. Early approaches utilized direct delivery of protein growth factors activin A and bone morphogenetic protein 4 (BMP4) to achieve this effect[78,79], but more conventional approaches leverage upstream WNT pathway modulation via small molecule activators and inhibitors to achieve the same effect with more consistent results[53,80]. Recent advances in cardiomyocyte differentiation approaches enable further improvements to cardiomyocyte purity yield and increased population specificity (e.g. ventricular vs. atrial cardiomyocytes and nodal cells) by pairing small molecule strategies with direct protein delivery[81–83] .

2.7 Scaffold materials for engineered cardiac tissue define function

With our growing understanding of cellular mechanotransduction through cell-cell, cell-matrix, and cell-substrate interactions, study of cell function and phenotype has begun to shift from exclusive consideration of cell monolayers in 2D culture on polystyrene, glass, or soft substrates to 3D cell culture formats. In the field of cardiac tissue engineering, this shift in cellular microenvironment has led to the evaluation of a wide variety of scaffold materials for engineered cardiac tissues, including synthetic polymers such as poly(lactic acid) (PLA), poly(glycerol sebacate) (PGS), poly(caprolactone) (PCL), and polyglycolic acid (PGA), as well as natural polymers such as collagen, fibrin, hyaluronic acid, chitosan, and silk. Generally, synthetic polymers are associated with desirable mechanical properties (capable of far exceeding the stiffness and ultimate tensile stresses of native myocardium) and are compatible with diverse fabrication techniques (including electrospinning and 3D printing), but suffer from limitations related to cell adhesion sites, immune response, and degradation and remodeling in vivo[84–89]. Conversely, natural polymers often have poor mechanical properties (less stiff and more fragile than native tissue, particularly in the hydrogel format) and have limited compatibility with aggressive fabrication techniques that may denature and damage the native protein structures, but feature excellent biocompatibility, density of cell adhesion sites, and degradation and remodeling in vivo[29,90–94]. In addition to the diversity in scaffold materials, a number of cardiac scaffold formats have also been explored, including fenestrated hydrogels designed to induce cardiomyocyte alignment via strain fields[17,19], sponges and foams of varying pore size and porosity[95–98], and aligned electrospun nanofiber mats[16,99–101].

In spite of the broad selection of scaffold polymers and formats available to cardiac tissue engineers, predominant research groups have largely converged on the use of simple collagen or fibrin hydrogels ranging in concentration from 0.5 to 1.5 mg/mL and from 2 to 4 mg/mL, respectively[91,102–106]. In spite of this convergence, there is little literature to justify the use of one formulation over the other, nor analysis of blended collagen and fibrin hydrogels[29]. While these simple natural polymer hydrogels do have a number of advantages, including a high density of cell adhesion sites, known metabolic degradation pathways, and ease-of-use in tissue casting methods, they deviate significantly from the mechanical and structural properties of native cardiac ECM.

2.8 Collagen is an attractive and versatile biomaterial

As the primary component of nearly every soft tissue extracellular matrix in the human body[107], collagen offers numerous benefits as a biomaterial for tissue engineering. All collagens are defined by their distinctive triple helix structure, but the composition of the individual chains varies among collagen types. A total of 29 collagen types can be found in tissues throughout the body, though a majority are only found in relatively small quantities. Conversely, collagen I, composed of two identical α1 chains and a single α2 chain, is the singular most ubiquitous protein in the entire animal kingdom as well as in humans, accounting for over 25% of total human protein mass (roughly 15% of body weight)[108].

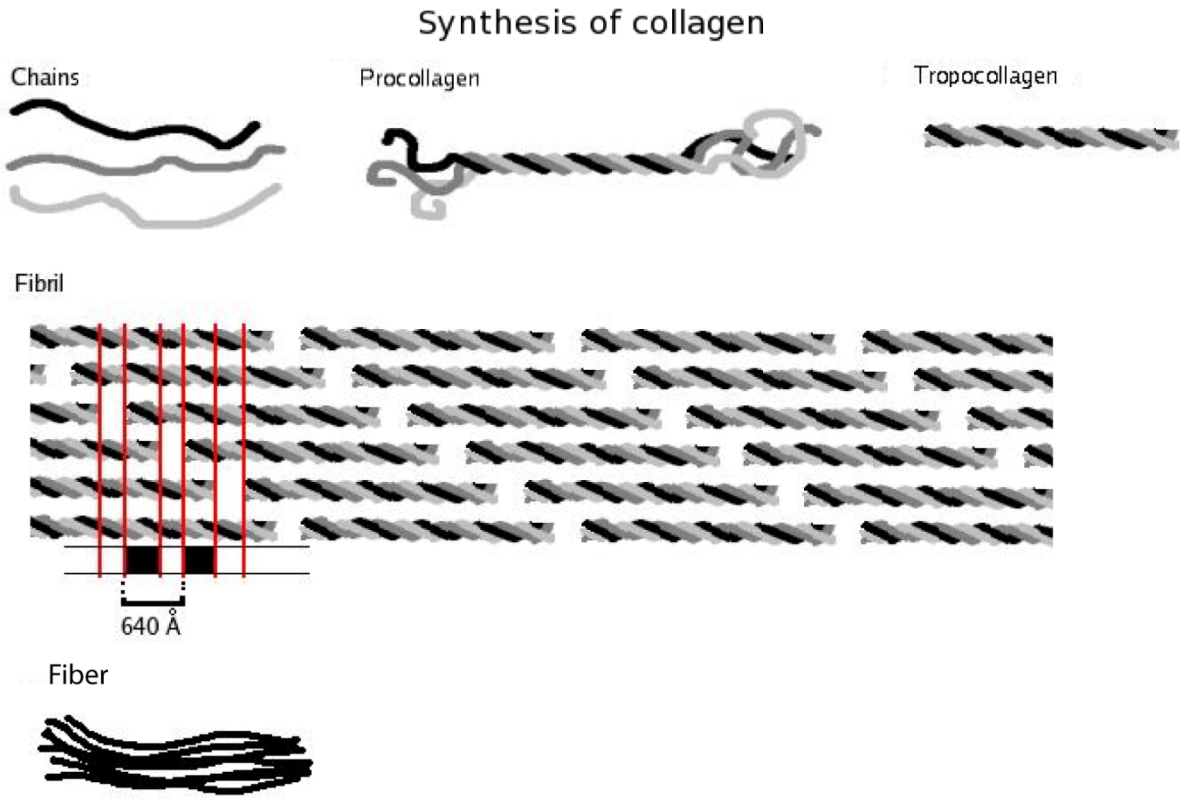

Image by Solitchka on fr.wikipedia, distributed under the GNU Free Documentation License (v1.2)

Figure 1. 2: Collagen formation, cleavage, and self-assembly.

Following transcription and translation, the procollagen α-chains that compose collagen I are modified in both the rough endoplasmic reticulum and the Golgi apparatus to enable the formation of triple helical procollagen, which is then transported to the extracellular space by secretory vesicles[109]. In the extracellular space, the exposed amino- and carboxy-propeptides of the procollagen molecules are cleaved, creating tropocollagen "monomers" ~300 nm in length (Fig 1.2)[109]. Guided by telopeptides[110,111], under physiological conditions these collagen monomers self-assemble first into fibrils with diameters as small as 30 nm and then into hierarchically organized fibers with staggered gaps between individual collagen molecules of ~67 nm and diameters as large as 20 μm[112,113].

Collagen I is immediately attractive as a biomaterial in part because it has known metabolic clearance pathways in vivo, and collagen-based biologic and medical device therapeutic products have received approval for commercial sale by the US Food and Drug Administration (FDA)[91,114,115]. From a cellular perspective, collagen features a high density of cell adhesion sites available for integrin binding (such as α1β1, α2β1, and α11β1), promoting cell adhesion and signaling via mechanotransduction pathways[116,117]. Additionally, collagen I can easily be remodeled by resident cells via cellular force generation as well as matrix metalloproteinases (MMPs), a characteristic that has been associated with improved tissue integration and immune response in vivo[90,118]. Critically, however, these desirable bioactive characteristics can easily be diminished or destroyed by degradation of molecular collagen integrity, either through denaturation or excessive crosslinking[90,119–121].

2.8.1 Electrospun Collagen

Electrospinning enables the production of nanoscale fibers that emulate the fibrous structure present in native extracellular matrix (20 nm to 8 um)[122]. Standard electrospinning methods involve dissolving a natural or synthetic polymer in a volatile solvent and extruding this solution through an electrically charged needle[123,124]. A grounded or oppositely charged plate, cylinder, or other collection device is placed opposite the needle exit, attracting the charged polymer stream as it exits the needle tip. As the polymer solution travels through the air, the volatile solvent evaporates, leaving behind polymer nanofibers ranging in thickness from 175 to 350 nm depending on parameters including solution flow rate, applied voltage, and distance between the extrusion and collection points[125]. Nanofibers landing on simple planar surfaces collect into randomly oriented overlapping meshes or mats, which have been extensively evaluated as biomaterials[126,127]. More sophisticated approaches use a grounded rotating fixture, enabling the collection of nanofiber geometries with varying degrees of directional orientation[58,128–130].

Due to the versatility of the technique and interest in the development of nanoscale patterned materials for manipulating cell microenvironments, electrospun fibers and meshes have shown promise in diverse cardiac tissue engineering applications including fabrication heart valves[87,131,132], myocardium[16,133,134], and aorta[135–137]. The ability to manipulate parameters with resolution on the nanoscale, including fiber diameter and pore size, offers a very precise method for manipulating cell-scaffold interactions. Electrospinning with synthetic materials such as PCL, PGS, and poly(lactic-co-glycolic acid) (PLGA) has been most broadly investigated in this space due to the increased tunability of the synthetic polymers to suit the electrospinning format, compatibility with the required solvents, and superior mechanical properties which greatly facilitate collection of intact nanofibers[87,127,138–141].

While electrospinning has been attempted with natural polymers with some success, other studies have indicated that the volatile solvents required for electrospinning of unblended natural polymers can denature fragile protein structures[119,125]. In the case of collagen only electrospinning, this yields gelatin nanofibers, a natural polymer with less desirable cell adhesion and mechanical properties for tissue engineering applications[119]. Recent methods have achieved nanoscale control of collagen while maintaining collagen integrity following electrospinning by blending or conjugating it with a synthetic polymer, but this approach necessarily reduces the density of collagen cell adhesion sites and may alter other desirable characteristics such as mechanical properties and the in vivo degradation rate[142–144]. Electrospinning also suffers from a high sensitivity to environmental factors, including humidity and temperature, requiring tight control over these parameters in order to yield consistent results, thereby restricting the accessibility of the technique to labs with specialized environmental control chambers. Finally, the necessarily rapid speed of electrospun fiber production (2 to 15 m/s, depending on desired alignment)[145] makes the fabrication of meshes and mats with patterns more sophisticated than general axial alignment extremely challenging[146,147].

2.8.2 Wet Spun Collagen

Wet spinning is a method of producing polymer fibers that has been used to produce fibers from synthetic polymers, such as acrylic, rayon, and spandex, for over 100 years. More recently, the same approach has been applied to produce collagen microfibers. First described by Pins et. al. in 1997, collagen in an acid solution can be neutralized while traveling in a coaxial flow system, resulting in the precipitation and polymerization of the collagen from solution[148]. Incubation in a neutral pH salt solution can enable collagen self-assembly over time, resulting in a collagen microfiber with properties similar to those found in unprocessed collagen. This wet spinning process was advanced in 2011 by Caves et al.[149] through the development of a process to enable continuous collection of wet spun collagen microfibers. With the addition of an automated spooling device and the implementation of a revised incubation protocol, fibers with lengths of up to 60 m could be produced, enabling the fabrication of aligned fiber structures.

A major advantage the collagen wet spinning offers over collagen electrospinning is the purity and integrity of the collagen itself. The solvents required for collagen only electrospinning that degrade the collagen during processing are not necessary for collagen wet spinning, which utilizes only collagen dissolved in a weak acid, buffer solutions, and alcohol. Differential scanning calorimetry (DSC), transmission electron microscopy (TEM), and second harmonic generation (SHG) imaging have all been utilized to confirm that collagen secondary and tertiary molecular structure is preserved following extrusion wet spinning processes[119,149,150].

Importantly, the microfiber wet spinning process also enables increased control over the mesh designs that are produced. Due to the slower rate of fiber production and larger size of the fibers themselves, individual fibers can be placed with greater precision and are less susceptible to factors that make nanofibers challenging to work with, such as fragility and static attraction[149–151]. This feature allows for either the collection of continuous spools of collagen microfiber threads that can later be fabricated into meaningful structures, or for the immediate fabrication of mesh scaffolds with controlled geometries during the fiber fabrication process. Collagen wet spinning is limited as a scaffold fabrication method primarily by the minimum fiber diameter that can be produced (~25 μm), as well as the much slower rate of fiber production (~60 m/hr) compared to electrospinning[149].

2.9 Project Objective and Hypothesis

Due to the critical role of extracellular matrix cues in tissue development, and the significant deviation of current conventional cardiac tissue scaffolds from the properties of native myocardium, we hypothesized that a cardiac tissue scaffold that approaches the mechanical and structural anisotropy of native myocardium may improve resident cardiomyocyte alignment and tissue contractile force. To evaluate this hypothesis, we developed a three-tiered approach to the investigation, design, fabrication, and evaluation of a more physiologically relevant cardiac tissue scaffold platform.

2.9.1 Specific Aim 1: Identify optimal conditions for creating functional engineered cardiac tissues using iPSC-CMs and blended collagen and fibrin hydrogels.

Natural polymer hydrogels are used ubiquitously as scaffold materials for cardiac tissue engineering and more broadly for soft tissue engineering due to FDA approval, minimal immunogenicity, and well-defined physiological clearance pathways. However, the relationships between natural polymer hydrogels and resident cell populations in directing the development of engineered tissues are poorly defined. This is of particular concern for tissues prepared with iPSC-derived cell populations, in which population purity and batch-to-batch variability become additional critical factors to consider. Herein, the design space for a blended fibrin and collagen scaffold is characterized for applications in creating engineered myocardium with human iPSC-derived cardiomyocytes. Stiffness values of the acellular hydrogel formulations considered approach those of native myocardium in compression but deviate significantly in tension when compared to rat myocardium in both transverse and longitudinal fiber orientations. A response surface methodology approach to understanding the relationship between collagen concentration, fibrin concentration, seeding density, and cardiac purity found a statistically significant predictive model across three repeated studies that confirms that all of these factors contribute to tissue compaction. In these constructs, increased fibrin concentration and seeding density were each associated with increased compaction, while increased collagen concentration was associated with decreased compaction. Both the lowest (24.4% cTnT+) and highest (60.2% cTnT+) cardiomyocyte purities evaluated were associated with decreased compaction, while the greatest compaction was predicted to occur in constructs prepared with a 40-50% cTnT+ population. Constructs prepared with purified cardiomyocytes (≥75.5% cTnT+) compacted and formed syncytia well, although increased fibrin concentration in these groups was associated with decreased compaction, a reversal of the trend observed in unpurified cardiomyocytes. This study demonstrates an analytical approach to understanding cell-scaffold interactions in engineered tissues and provides a foundation for the development of more sophisticated and customized scaffold platforms for human cardiac tissue engineering. *Kaiser, N. J., Kant, R. J., Minor, A. J. & Coulombe, K. L. K. Optimizing Blended Collagen-Fibrin Hydrogels for Cardiac*

*Tissue Engineering with Human iPSC-derived Cardiomyocytes. ACS Biomaterials Science & Engineering **5**, 887–899 (2019).*

2.9.2 Specific Aim 2: Develop and characterize a low-cost, facile method for fabricating scaffolds with anisotropic mechanical properties capable of emulating soft tissue.

A great variety of natural and synthetic polymer materials have been utilized in soft tissue engineering as extracellular matrix materials. Natural polymers, such as collagen and fibrin hydrogels, have experienced especially broad adoption due to the high density of cell adhesion sites compared to their synthetic counterparts, ready availability, and ease of use. However, these and other hydrogels lack the structural and mechanical anisotropy that define the extracellular matrix in many tissues, such as skeletal and cardiac muscle, tendon, and cartilage. Herein, we present a facile, low-cost, and automated method of preparing collagen microfibers, organizing these fibers into precisely controlled mesh designs, and embedding these tissues in a bulk hydrogel, thus creating a composite biomaterial suitable for a wide variety of tissue engineering and regenerative medicine applications. With the assistance of custom software tools described herein, mesh patterns are designed via a digital graphical user interface and translated into protocols that are executed by a custom mesh collection and organization device. We demonstrate a high degree of precision and reproducibility in both fiber and mesh fabrication, evaluate single fiber mechanical properties, and provide evidence of collagen self-assembly in the microfibers under standard cell culture conditions. This work offers a powerful and flexible platform for the study of tissue engineering and cell material interactions as well as the development of therapeutic biomaterials in the form of custom collagen microfiber patterns that will be accessible to all through the methods and techniques described here. *Kaiser, N. J., Bellows, J. A., Kant, R. J., & Coulombe, K. L. K. Digital Design and Automated Fabrication of Bespoke Collagen Microfiber Scaffolds. Tissue Engineering: Part C, 2019, Accepted 4/1/19*

2.9.3 Specific Aim 3: Evaluate the architecture and performance of tissues prepared with the composite scaffold platform in vitro and in vivo.

Conventional engineered cardiac tissues often utilize simple collagen or fibrin hydrogels as a scaffold material due to their biocompatibility, known in vivo degradation process, and ease of use. Recent approaches have iterated on this format by manipulating tissue shape, promoting the alignment of cardiomyocytes along stress fields that develop during stretch or tissue remodeling, and thereby emulating some of the structural organization present in native myocardium. Cardiac tissues fabricated with embedded collagen microfiber meshes offer a means of providing similar directional cues to resident cells without the need for fenestrations or other constraints on tissue shape, while also creating an anisotropic mechanical microenvironment that emulates native myocardium. The active and passive functional performance of composite cardiac tissues prepared with parallel and overlapping 30-degree fiber arrays was compared to that of fiber-free constructs prepared with an induced stress field via compaction in vitro. Embedded collagen microfibers significantly modulated tissue compaction, thereby influencing tissue development as assessed by immunohistochemical markers of cardiomyocyte phenotype and maturity. No significant differences were observed between groups with respect to tensile stiffness, and all composite tissue groups approached Young's modulus values typical of adult myocardium (ranging from 33.64±6.44 kPa to 56.64±14.79 kPa). While no significant differences in contractile force were observed between sample groups, positive trends in parallel fiber construct force production relative to fiber-free controls were observed. This study demonstrates that embedded collagen microfibers can modulate engineered cardiac tissue function and development and justifies further evaluation of cardiac tissues with embedded parallel fiber mesh designs.

2.10 References

1. World Health Organization. *The Global Burden of Disease: 2004 Update*. (2008).

2. Wang, H. *et al.* Global, regional, and national life expectancy, all-cause mortality, and cause-specific mortality for 249 causes of death, 1980–2015: a systematic analysis for the Global Burden of Disease Study 2015. *The Lancet* **388**, 1459–1544 (2016).

3. Kajstura, J. *et al.* Coronary artery constriction in rats: necrotic and apoptotic myocyte death. *The American Journal of Cardiology* **82**, 30K-41K (1998).

4. Konstantinidis, K., Whelan, R. S. & Kitsis, R. N. Mechanisms of Cell Death in Heart Disease. *Arterioscler Thromb Vasc Biol* **32**, (2012).

5. Vaccarino, V. *et al.* Presentation, management, and outcomes of ischaemic heart disease in women. *Nature Reviews Cardiology* **10**, 508–518 (2013).

6. Kaski Juan-Carlos, Crea Filippo, Gersh Bernard J. & Camici Paolo G. Reappraisal of Ischemic Heart Disease. *Circulation* **138**, 1463–1480 (2018).

7. Kandaswamy, E. & Zuo, L. Recent Advances in Treatment of Coronary Artery Disease: Role of Science and Technology. *Int J Mol Sci* **19**, (2018).

8. Dababneh, E. & Goldstein, S. Chronic Ischemic Heart Disease Selection of Treatment Modality. in *StatPearls* (StatPearls Publishing, 2019).

9. Buja, L. M. The Pathobiology of Acute Coronary Syndromes. *Tex Heart Inst J* **40**, 221–228 (2013).

10. Moryś, J. M., Bellwon, J., Höfer, S., Rynkiewicz, A. & Gruchała, M. Quality of life in patients with coronary heart disease after myocardial infarction and with ischemic heart failure. *Arch Med Sci* **12**, 326–333 (2016).

11. Goreishi, A., Shajari, Z. & Mohammadi, Z. Chronic Ischemic Heart Disease Affects Health Related Quality of Life. *Cardiol Res* **3**, 264–270 (2012).

12. Westin, L. *et al.* Quality of life in patients with ischaemic heart disease: a prospective controlled study. *J. Intern. Med.* **242**, 239–247 (1997).

13. Parker, K. K. & Ingber, D. E. Extracellular matrix, mechanotransduction and structural hierarchies in heart tissue engineering. *Philos Trans R Soc Lond B Biol Sci* **362**, 1267–1279 (2007).

14. Vunjak-Novakovic, G. *et al.* Challenges in Cardiac Tissue Engineering. *Tissue Engineering Part B: Reviews* **16**, 169–187 (2009).

15. Zhang, Y. S. *et al.* From cardiac tissue engineering to heart-on-a-chip: beating challenges. *Biomed. Mater.* **10**, 034006 (2015).

16. Kai, D., Prabhakaran, M. P., Jin, G. & Ramakrishna, S. Guided orientation of cardiomyocytes on electrospun aligned nanofibers for cardiac tissue engineering. *J. Biomed. Mater. Res.* **98B**, 379–386 (2011).

17. Bian, W., Jackman, C. P. & Bursac, N. Controlling the structural and functional anisotropy of engineered cardiac tissues. *Biofabrication* **6**, 024109 (2014).

18. Tiburcy, M. *et al.* Defined Engineered Human Myocardium with Advanced Maturation for Applications in Heart Failure Modelling and Repair. *Circulation* **135**, 1832–1847 (2017).

19. Munarin, F., Kaiser, N. J., Kim, T. Y., Choi, B.-R. & Coulombe, K. L. K. Laser-Etched Designs for Molding Hydrogel-Based Engineered Tissues. *Tissue Eng Part C Methods* **23**, 311–321 (2017).

20. Potter, R. F. & Groom, A. C. Capillary diameter and geometry in cardiac and skeletal muscle studied by means of corrosion casts. *Microvasc. Res.* **25**, 68–84 (1983).

21. Dodge, J. T. J., Brown, B. G., Bolson, E. L. M. & Dodge, H. T. Lumen Diameter of Normal Human Coronary Arteries: Influence of Age, Sex, Anatomic Variation, and Left Ventricular Hypertrophy or Dilation. *Circulation* **86**, 232–246 (1992).

22. Ho, S. Y. Anatomy and myoarchitecture of the left ventricular wall in normal and in disease. *European Journal of Echocardiography* **10**, iii3–iii7 (2009).

23. Masters, M. & Riley, P. R. The epicardium signals the way towards heart regeneration. *Stem Cell Res* **13**, 683–692 (2014).

24. Pérez-Pomares, J. M., González-Rosa, J. M. & Muñoz-Chápuli, R. Building the vertebrate heart - an evolutionary approach to cardiac development. *Int. J. Dev. Biol.* **53**, 1427–1443 (2009).

25. Nerbonne, J. M. & Kass, R. S. Molecular physiology of cardiac repolarization. *Physiol. Rev.* **85**, 1205–1253 (2005).

26. Criscione, J. C., Rodriguez, F. & Miller, D. C. The myocardial band: simplicity can be a weakness. *Eur J Cardiothorac Surg* **28**, 363–364; author reply 364-367 (2005).

27. Anderson, R. H., Ho, S. Y., Redmann, K., Sanchez-Quintana, D. & Lunkenheimer, P. P. The anatomical arrangement of the myocardial cells making up the ventricular mass. *Eur J Cardiothorac Surg* **28**, 517–525 (2005).
28. Weber, K. T. Cardiac interstitium in health and disease: The fibrillar collagen network. *Journal of the American College of Cardiology* **13**, 1637–1652 (1989).
29. Kaiser, N. J., Kant, R. J., Minor, A. J. & Coulombe, K. L. K. Optimizing Blended Collagen-Fibrin Hydrogels for Cardiac Tissue Engineering with Human iPSC-derived Cardiomyocytes. *ACS Biomater. Sci. Eng.* **5**, 887–899 (2019).
30. Hasenfuss, G. *et al.* Energetics of isometric force development in control and volume-overload human myocardium. Comparison with animal species. *Circulation Research* **68**, 836–846 (1991).
31. Vandenboom, R. & Metzger, J. M. A “Wringing” Endorsement for Myosin Phosphorylation in the Heart. *Molecular Interventions* **2**, 422 (2002).
32. Davis, J. S. *et al.* The Overall Pattern of Cardiac Contraction Depends on a Spatial Gradient of Myosin Regulatory Light Chain Phosphorylation. *Cell* **107**, 631–641 (2001).
33. Fuchs, E. *et al.* Cardiac rotation and relaxation in patients with chronic heart failure. *European Journal of Heart Failure* **6**, 715–722 (2004).
34. Kroeker, C. A., Tyberg, J. V. & Beyar, R. Effects of ischemia on left ventricular apex rotation. An experimental study in anesthetized dogs. *Circulation* **92**, 3539–3548 (1995).
35. Sengupta, P. P., Khandheria, B. K. & Narula, J. Twist and Untwist Mechanics of the Left Ventricle. *Heart Failure Clinics* **4**, 315–324 (2008).
36. Omar Alaa Mabrouk Salem, Vallabhajosyula Sharath & Sengupta Partho P. Left Ventricular Twist and Torsion. *Circulation: Cardiovascular Imaging* **8**, e003029 (2015).
37. Chilton, R. J. Pathophysiology of Coronary Heart Disease: A Brief Review. *J Am Osteopath Assoc* **104**, 5S-8S (2004).
38. Moran, A. E. *et al.* Assessing the Global Burden of Ischemic Heart Disease. *Glob Heart* **7**, 315–329 (2012).
39. Chiong, M. *et al.* Cardiomyocyte death: mechanisms and translational implications. *Cell Death & Disease* **2**, e244 (2011).
40. Buja L. Maximilian & Entman Mark L. Modes of Myocardial Cell Injury and Cell Death in Ischemic Heart Disease. *Circulation* **98**, 1355–1357 (1998).
41. Hashmi, S. & Al-Salam, S. Acute myocardial infarction and myocardial ischemia-reperfusion injury: a comparison. *Int J Clin Exp Pathol* **8**, 8786–8796 (2015).
42. Richardson, W., Clarke, S., Quinn, T. & Holmes, J. Physiological Implications of Myocardial Scar Structure. *Compr Physiol* **5**, 1877–1909 (2015).
43. Gottlieb, R. A., Burleson, K. O., Kloner, R. A., Babior, B. M. & Engler, R. L. Reperfusion injury induces apoptosis in rabbit cardiomyocytes. *J Clin Invest* **94**, 1621–1628 (1994).
44. Buja, L. M. Myocardial ischemia and reperfusion injury. *Cardiovascular Pathology* **14**, 170–175 (2005).
45. Boyle, E. M., Pohlman, T. H., Cornejo, C. J. & Verrier, E. D. Endothelial Cell Injury in Cardiovascular Surgery: Ischemia-Reperfusion. *The Annals of Thoracic Surgery* **62**, 1868–1875 (1996).
46. Kalogeris, T., Baines, C. P., Krenz, M. & Korthuis, R. J. Cell Biology of Ischemia/Reperfusion Injury. *Int Rev Cell Mol Biol* **298**, 229–317 (2012).
47. Chatterjee, K. Right Ventricular Infarction: Pathogenesis of Low Output. in *Update 1988* (ed. Vincent, J. L.) 317–326 (Springer Berlin Heidelberg, 1988). doi:10.1007/978-3-642-83392-2_40
48. Ondrus, T. *et al.* Right ventricular myocardial infarction: From pathophysiology to prognosis. *Exp Clin Cardiol* **18**, 27–30 (2013).
49. Boublik, J. *et al.* Mechanical Properties and Remodeling of Hybrid Cardiac Constructs Made from Heart Cells, Fibrin, and Biodegradable, Elastomeric Knitted Fabric. *Tissue Engineering* **11**, 1122–1132 (2005).
50. Stoppel, W. L., Hu, D., Domian, I. J., Kaplan, D. L. & Iii, L. D. B. Anisotropic silk biomaterials containing cardiac extracellular matrix for cardiac tissue engineering. *Biomed. Mater.* **10**, 034105 (2015).
51. Zimmermann, W. & Eschenhagen, T. Multiloop Engineered Heart Muscle Tissue. (2016).
52. Ogle, B. M. *et al.* Distilling complexity to advance cardiac tissue engineering. *Science Translational Medicine* **8**, 342ps13-342ps13 (2016).
53. Lian, X. *et al.* Directed cardiomyocyte differentiation from human pluripotent stem cells by modulating Wnt/β-catenin signaling under fully defined conditions. *Nat Protoc* **8**, 162–175 (2013).
54. Duan, Y. *et al.* Hybrid Gel Composed of Native Heart Matrix and Collagen Induces Cardiac Differentiation of Human Embryonic Stem Cells without Supplemental Growth Factors. *J. of Cardiovasc. Trans. Res.* **4**, 605–615 (2011).

55. Jung, J. P., Hu, D., Domian, I. J. & Ogle, B. M. An integrated statistical model for enhanced murine cardiomyocyte differentiation via optimized engagement of 3D extracellular matrices. *Scientific Reports* **5**, 18705 (2015).
56. Becher, U. M., Tiyerili, V., Skowasch, D., Nickenig, G. & Werner, N. Personalized cardiac regeneration by stem cells–Hype or hope? *EPMA Journal* **2**, 119–130 (2011).
57. Ellis, B. W., Acun, A., Can, U. I. & Zorlutuna, P. Human iPSC-derived myocardium-on-chip with capillary-like flow for personalized medicine. *Biomicrofluidics* **11**, 024105 (2017).
58. Mahjour, S. B., Sefat, F., Polunin, Y., Wang, L. & Wang, H. Improved cell infiltration of electrospun nanofiber mats for layered tissue constructs. *J. Biomed. Mater. Res.* n/a-n/a (2016). doi:10.1002/jbm.a.35676
59. Chiu, L., Radisic, M. & Vunjak-Novakovic, G. Bioactive scaffolds for engineering vascularized cardiac tissues. *Macromol Biosci* **10**, 1286–1301 (2010).
60. Bracaglia, L. G. *et al.* 3D Printed Pericardium Hydrogels to Promote Wound Healing in Vascular Applications. *Biomacromolecules* (2017). doi:10.1021/acs.biomac.7b01165
61. Lee, S., Tong, X., Han, L.-H., Behn, A. & Yang, F. Aligned Microribbon-like Hydrogels for Guiding Three-dimensional Smooth Muscle Tissue Regeneration. *J. Biomed. Mater. Res.* n/a-n/a (2016). doi:10.1002/jbm.a.35662
62. Jang, J. *et al.* 3D printed complex tissue construct using stem cell-laden decellularized extracellular matrix bioinks for cardiac repair. *Biomaterials* doi:10.1016/j.biomaterials.2016.10.026
63. Rupert, C. E. & Coulombe, K. L. K. IGF1 and NRG1 Enhance Proliferation, Metabolic Maturity, and the Force-Frequency Response in hESC-Derived Engineered Cardiac Tissues. *Stem Cells International* (2017). doi:10.1155/2017/7648409
64. Feric, N. T. & Radisic, M. Towards adult-like human engineered cardiac tissue: Maturing human pluripotent stem cell-derived cardiomyocytes in human engineered cardiac tissues. *Advanced Drug Delivery Reviews* doi:10.1016/j.addr.2015.04.019
65. Bujak, M. & Frangogiannis, N. G. The role of TGF-β signaling in myocardial infarction and cardiac remodeling. *Cardiovasc Res* **74**, 184–195 (2007).
66. McCain, M., Hyngsuk, L., Aratyn-Schaus, Y., Kleber, A. & Parker, K. K. Cooperative coupling of cell-matrix and cell-cell adhesions in cardiac muscle. (2012).
67. Laflamme, M. A. & Murry, C. E. Heart regeneration. *Nature* **473**, 326–335 (2011).
68. Bergmann, O. *et al.* Evidence for cardiomyocyte renewal in humans. *Science* **324**, 98–102 (2009).
69. Ali, S. R. *et al.* Existing cardiomyocytes generate cardiomyocytes at a low rate after birth in mice. *PNAS* **111**, 8850–8855 (2014).
70. Miller, J. D. & Schlaeger, T. M. Generation of induced pluripotent stem cell lines from human fibroblasts via retroviral gene transfer. *Methods Mol. Biol.* **767**, 55–65 (2011).
71. Rodríguez-Pizà, I. *et al.* Reprogramming of human fibroblasts to induced pluripotent stem cells under xeno-free conditions. *Stem Cells* **28**, 36–44 (2010).
72. Afzal, M. Z. *et al.* Generation of human iPSCs from urine derived cells of a non-affected control subject. *Stem Cell Res* **18**, 33–36 (2017).
73. Zhou, T. *et al.* Generation of human induced pluripotent stem cells from urine samples. *Nat Protoc* **7**, 2080–2089 (2012).
74. Zhou, T. *et al.* Generation of Induced Pluripotent Stem Cells from Urine. *J Am Soc Nephrol* **22**, 1221–1228 (2011).
75. Batalov, I. & Feinberg, A. W. Differentiation of Cardiomyocytes from Human Pluripotent Stem Cells Using Monolayer Culture. *Biomark Insights* **10**, 71–76 (2015).
76. Später, D., Hansson, E. M., Zangi, L. & Chien, K. R. How to make a cardiomyocyte. *Development* **141**, 4418–4431 (2014).
77. Van Vliet, P., Wu, S. M., Zaffran, S. & Pucéat, M. Early cardiac development: a view from stem cells to embryos. *Cardiovasc Res* **96**, 352–362 (2012).
78. Teo, A. K. K. *et al.* Activin and BMP4 synergistically promote formation of definitive endoderm in human embryonic stem cells. *Stem Cells* **30**, 631–642 (2012).
79. Yang, L. *et al.* Human cardiovascular progenitor cells develop from a KDR+ embryonic-stem-cell-derived population. *Nature* **453**, 524–528 (2008).
80. Lian, X. *et al.* Robust cardiomyocyte differentiation from human pluripotent stem cells via temporal modulation of canonical Wnt signaling. *PNAS* **109**, E1848–E1857 (2012).
81. Kim, M.-S. *et al.* Activin-A and Bmp4 Levels Modulate Cell Type Specification during CHIR-Induced Cardiomyogenesis. *PLoS One* **10**, (2015).

82. Schweizer, P. A. *et al.* Subtype-specific differentiation of cardiac pacemaker cell clusters from human induced pluripotent stem cells. *Stem Cell Res Ther* **8**, (2017).
83. Cyganek, L. *et al.* Deep phenotyping of human induced pluripotent stem cell–derived atrial and ventricular cardiomyocytes. *JCI Insight* **3**, (2018).
84. Santoro, M., Shah, S. R., Walker, J. L. & Mikos, A. G. Poly(lactic acid) nanofibrous scaffolds for tissue engineering. *Advanced Drug Delivery Reviews* doi:10.1016/j.addr.2016.04.019
85. Dhandayuthapani, B., Yoshida, Y., Maekawa, T. & Kumar, D. S. Polymeric Scaffolds in Tissue Engineering Application: A Review. *International Journal of Polymer Science* **2011**, e290602 (2011).
86. Freed, L. E. *et al.* Biodegradable Polymer Scaffolds for Tissue Engineering. *Nat Biotech* **12**, 689–693 (1994).
87. Masoumi, N. *et al.* Electrospun PGS:PCL Microfibers Align Human Valvular Interstitial Cells and Provide Tunable Scaffold Anisotropy. *Adv. Healthcare Mater.* **3**, 929–939 (2014).
88. Bajaj, P., Schweller, R. M., Khademhosseini, A., West, J. L. & Bashir, R. 3D Biofabrication Strategies for Tissue Engineering and Regenerative Medicine. *Annu Rev Biomed Eng* **16**, 247–276 (2014).
89. Rampichová, M. *et al.* Non-woven PGA/PVA fibrous mesh as an appropriate scaffold for chondrocyte proliferation. *Physiol Res* **59**, 773–781 (2010).
90. Badylak, S. F. & Gilbert, T. W. Immune Response to Biologic Scaffold Materials. *Semin Immunol* **20**, 109–116 (2008).
91. Kaiser, N. J. & Coulombe, K. L. K. Physiologically inspired cardiac scaffolds for tailored in vivo function and heart regeneration. *Biomed. Mater.* **10**, 034003 (2015).
92. Chrobak, M. O. *et al.* Design of a Fibrin Microthread-Based Composite Layer for Use in a Cardiac Patch. *ACS Biomater. Sci. Eng.* **3**, 1394–1403 (2017).
93. Williams, C. *et al.* Cardiac extracellular matrix–fibrin hybrid scaffolds with tunable properties for cardiovascular tissue engineering. *Acta Biomaterialia* **14**, 84–95 (2015).
94. Dong, C. & Lv, Y. Application of Collagen Scaffold in Tissue Engineering: Recent Advances and New Perspectives. *Polymers* **8**, 42 (2016).
95. Lu, L. *et al.* In vitro and in vivo degradation of porous poly(dl-lactic-co-glycolic acid) foams. *Biomaterials* **21**, 1837–1845 (2000).
96. Li, N. *et al.* Three-dimensional graphene foam as a biocompatible and conductive scaffold for neural stem cells. *Sci. Rep.* **3**, (2013).
97. Wu, X. *et al.* Preparation of aligned porous gelatin scaffolds by unidirectional freeze-drying method. *Acta Biomaterialia* **6**, 1167–1177 (2010).
98. O'Brien, F. J., Harley, B. A., Yannas, I. V. & Gibson, L. Influence of freezing rate on pore structure in freeze-dried collagen-GAG scaffolds. *Biomaterials* **25**, 1077–1086 (2004).
99. Baker, B. M. & Mauck, R. L. The Effect of Nanofiber Alignment on the Maturation of Engineered Meniscus Constructs. *Biomaterials* **28**, 1967–1977 (2007).
100. Jiang, J. *et al.* Expanded 3D Nanofiber Scaffolds: Cell Penetration, Neovascularization, and Host Response. *Advanced Healthcare Materials* **5**, 2993–3003 (2016).
101. Kim, P.-H. & Cho, J.-Y. Myocardial tissue engineering using electrospun nanofiber composites. *BMB Rep* (2015).
102. Ye, K. Y., Sullivan, K. E. & Black, L. D. Encapsulation of Cardiomyocytes in a Fibrin Hydrogel for Cardiac Tissue Engineering. *J Vis Exp* (2011). doi:10.3791/3251
103. Tulloch, N. L. *et al.* Growth of Engineered Human Myocardium with Mechanical Loading and Vascular Co-culture. *Circ Res* **109**, 47–59 (2011).
104. Tiburcy, M., Meyer, T., Soong, P. L. & Zimmermann, W.-H. Collagen-based engineered heart muscle. *Methods Mol. Biol.* **1181**, 167–176 (2014).
105. Eschenhagen, T. *et al.* 3D engineered heart tissue for replacement therapy. *Basic Res Cardiol* **97**, I146–I152 (2002).
106. Zimmermann, W.-H. *et al.* Tissue Engineering of a Differentiated Cardiac Muscle Construct. *Circulation Research* **90**, 223–230 (2002).
107. Lullo, G. A. D., Sweeney, S. M., Körkkö, J., Ala-Kokko, L. & Antonio, J. D. S. Mapping the Ligand-binding Sites and Disease-associated Mutations on the Most Abundant Protein in the Human, Type I Collagen. *J. Biol. Chem.* **277**, 4223–4231 (2002).
108. Smejkal, G. B. & Fitzgerald, C. Revised Estimate of Total Collagen in the Human Body. 2
109. Mouw, J. K., Ou, G. & Weaver, V. M. Extracellular matrix assembly: a multiscale deconstruction. *Nat Rev Mol Cell Biol* **15**, 771–785 (2014).

110. Prockop, D. J. & Fertala, A. Inhibition of the Self-assembly of Collagen I into Fibrils with Synthetic Peptides DEMONSTRATION THAT ASSEMBLY IS DRIVEN BY SPECIFIC BINDING SITES ON THE MONOMERS. *J. Biol. Chem.* **273**, 15598–15604 (1998).
111. Helseth, D. L. & Veis, A. Collagen self-assembly in vitro. Differentiating specific telopeptide-dependent interactions using selective enzyme modification and the addition of free amino telopeptide. *J. Biol. Chem.* **256**, 7118–7128 (1981).
112. Erickson, B. *et al.* Nanoscale Structure of Type I Collagen Fibrils: Quantitative Measurement of D-spacing. *Biotechnol J* **8**, 117–126 (2013).
113. Ushiki, T. Collagen Fibers, Reticular Fibers and Elastic Fibers. A Comprehensive Understanding from a Morphological Viewpoint. *Arch. Histol. Cytol.* **65**, 109–126 (2002).
114. Abraham, G. A., Murray, J., Billiar, K. & Sullivan, S. J. Evaluation of the porcine intestinal collagen layer as a biomaterial. *Journal of Biomedical Materials Research* **51**, 442–452 (2000).
115. MacNeil, S. Biomaterials for tissue engineering of skin. *Materials Today* **11**, 26–35 (2008).
116. Zeltz, C. & Gullberg, D. The integrin–collagen connection – a glue for tissue repair? *J Cell Sci* **129**, 653–664 (2016).
117. Jokinen, J. *et al.* Integrin-mediated Cell Adhesion to Type I Collagen Fibrils. *J. Biol. Chem.* **279**, 31956–31963 (2004).
118. Brown, B. N., Valentin, J. E., Stewart-Akers, A. M., McCabe, G. P. & Badylak, S. F. Macrophage phenotype and remodeling outcomes in response to biologic scaffolds with and without a cellular component. *Biomaterials* **30**, 1482–1491 (2009).
119. Zeugolis, D. I. *et al.* Electro-spinning of pure collagen nano-fibres – Just an expensive way to make gelatin? *Biomaterials* **29**, 2293–2305 (2008).
120. Plant, A. L., Bhadriraju, K., Spurlin, T. A. & Elliott, J. T. Cell response to matrix mechanics: Focus on collagen. *Biochimica et Biophysica Acta (BBA) - Molecular Cell Research* **1793**, 893–902 (2009).
121. Yamamoto, M., Yamato, M., Aoyagi, M. & Yamamoto, K. Identification of integrins involved in cell adhesion to native and denatured type I collagens and the phenotypic transition of rabbit arterial smooth muscle cells. *Exp. Cell Res.* **219**, 249–256 (1995).
122. Fleischer, S., Miller, J., Hurowitz, H., Shapira, A. & Dvir, T. Effect of fiber diameter on the assembly of functional 3D cardiac patches. *Nanotechnology* **26**, 291002 (2015).
123. Lasprilla-Botero, J., Álvarez-Láinez, M. & Lagaron, J. M. The influence of electrospinning parameters and solvent selection on the morphology and diameter of polyimide nanofibers. *Materials Today Communications* **14**, 1–9 (2018).
124. Luo, C. J., Nangrejo, M. & Edirisinghe, M. A novel method of selecting solvents for polymer electrospinning. *Polymer* **51**, 1654–1662 (2010).
125. Castilla-Casadiego, D. A. *et al.* Engineering of a Stable Collagen Nanofibrous Scaffold with Tunable Fiber Diameter, Alignment, and Mechanical Properties. *Macromol. Mater. Eng.* n/a-n/a (2016). doi:10.1002/mame.201600156
126. Meechaisue, C., Dubin, R., Supaphol, P., Hoven, V. P. & Kohn, J. Electrospun mat of tyrosine-derived polycarbonate fibers for potential use as tissue scaffolding material. *J Biomater Sci Polym Ed* **17**, 1039–1056 (2006).
127. Evrova, O. *et al.* Hybrid Randomly Electrospun Poly(lactic-co-glycolic acid):Poly(ethylene oxide) (PLGA:PEO) Fibrous Scaffolds Enhancing Myoblast Differentiation and Alignment. *ACS Appl. Mater. Interfaces* **8**, 31574–31586 (2016).
128. Shahabipour, F., Banach, M., Johnston, T. P., Pirro, M. & Sahebkar, A. Novel approaches towards the generation of bioscaffolds as a potential therapy in cardiovascular tissue engineering. *International Journal of Cardiology* doi:10.1016/j.ijcard.2016.11.210
129. Khan, M. *et al.* Evaluation of Changes in Morphology and Function of Human Induced Pluripotent Stem Cell Derived Cardiomyocytes (HiPSC-CMs) Cultured on an Aligned-Nanofiber Cardiac Patch. *PLoS ONE* **10**, e0126338 (2015).
130. Kuppan, P., Sethuraman, S. & Krishnan, U. M. Interaction of human smooth muscle cells with nanofibrous scaffolds: Effect of fiber orientation on cell adhesion, proliferation and functional gene expression. *J. Biomed. Mater. Res.* n/a-n/a (2014). doi:10.1002/jbm.a.35360
131. Masoumi, N. *et al.* Tri-layered elastomeric scaffolds for engineering heart valve leaflets. *Biomaterials* **35**, 7774–7785 (2014).
132. Hobson, C. M. *et al.* Fabrication of elastomeric scaffolds with curvilinear fibrous structures for heart valve leaflet engineering. *J. Biomed. Mater. Res.* n/a-n/a (2015). doi:10.1002/jbm.a.35450

133. Şenel Ayaz, H. G. *et al.* Textile-templated electrospun anisotropic scaffolds for regenerative cardiac tissue engineering. *Biomaterials* **35**, 8540–8552 (2014).
134. Zhao, G., Zhang, X., Lu, T. J. & Xu, F. Recent Advances in Electrospun Nanofibrous Scaffolds for Cardiac Tissue Engineering. *Adv. Funct. Mater.* n/a-n/a (2015). doi:10.1002/adfm.201502142
135. Bridge, J. C. *et al.* Electrospun gelatin-based scaffolds as a novel 3D platform to study the function of contractile smooth muscle cells in vitro. *Biomed. Phys. Eng. Express* **4**, 045039 (2018).
136. Cipitria, A., Skelton, A., Dargaville, T. R., Dalton, P. D. & Hutmacher, D. W. Design, fabrication and characterization of PCL electrospun scaffolds—a review. *J. Mater. Chem.* **21**, 9419–9453 (2011).
137. Qin, K. *et al.* Implantation of Electrospun Vascular Grafts with Optimized Structure in a Rat Model. *JoVE (Journal of Visualized Experiments)* e57340 (2018). doi:10.3791/57340
138. Rai, R., Tallawi, M., Grigore, A. & Boccaccini, A. R. Synthesis, properties and biomedical applications of poly(glycerol sebacate) (PGS): A review. *Progress in Polymer Science* **37**, 1051–1078 (2012).
139. Gaharwar, A. K., Nikkhah, M., Sant, S. & Khademhosseini, A. Anisotropic poly (glycerol sebacate)-poly (ϵ-caprolactone) electrospun fibers promote endothelial cell guidance. *Biofabrication* **7**, 015001 (2014).
140. Rai, R. *et al.* Bioactive Electrospun Fibers of Poly(glycerol sebacate) and Poly(ε-caprolactone) for Cardiac Patch Application. *Adv. Healthcare Mater.* n/a-n/a (2015). doi:10.1002/adhm.201500154
141. Khorshidi, S. *et al.* A review of key challenges of electrospun scaffolds for tissue-engineering applications. *Journal of Tissue Engineering and Regenerative Medicine* **10**, 715–738 (2016).
142. Chakrapani, V. Y., Gnanamani, A., Giridev, V. R., Madhusoothanan, M. & Sekaran, G. Electrospinning of type I collagen and PCL nanofibers using acetic acid. *Journal of Applied Polymer Science* **125**, 3221–3227 (2012).
143. Dippold, D. *et al.* Novel approach towards aligned PCL-Collagen nanofibrous constructs from a benign solvent system. *Materials Science and Engineering: C* **72**, 278–283 (2017).
144. He, W., Yong, T., Teo, W. E., Ma, Z. & Ramakrishna, S. Fabrication and endothelialization of collagen-blended biodegradable polymer nanofibers: potential vascular graft for blood vessel tissue engineering. *Tissue Eng.* **11**, 1574–1588 (2005).
145. Kiselev, P. & Rosell-Llompart, J. Highly aligned electrospun nanofibers by elimination of the whipping motion. *Journal of Applied Polymer Science* **125**, 2433–2441 (2012).
146. Teo, W.-E., Inai, R. & Ramakrishna, S. Technological advances in electrospinning of nanofibers. *Sci Technol Adv Mater* **12**, (2011).
147. Kenry & Lim, C. T. Nanofiber technology: current status and emerging developments. *Progress in Polymer Science* **70**, 1–17 (2017).
148. Pins, G. D., Christiansen, D. L., Patel, R. & Silver, F. H. Self-assembly of collagen fibers. Influence of fibrillar alignment and decorin on mechanical properties. *Biophys J* **73**, 2164–2172 (1997).
149. Caves, J. M. *et al.* Fibrillogenesis in Continuously Spun Synthetic Collagen Fiber. *J Biomed Mater Res B Appl Biomater* **93**, (2010).
150. Caves, J. M. *et al.* The use of microfiber composites of elastin-like protein matrix reinforced with synthetic collagen in the design of vascular grafts. *Biomaterials* **31**, (2010).
151. Caves, J. M. *et al.* Elastin-like protein matrix reinforced with collagen microfibers for soft tissue repair. *Biomaterials* **32**, 5371–5379 (2011).

CHAPTER 2: CUSTOM ENGINEERED TISSUE CULTURE MOLDS FROM LASER-ETCHED MASTERS

Reproduced with permission from Kaiser, N. J., Munarin, F. & Coulombe, K. L. K. Custom Engineered Tissue Culture Molds from Laser-etched Masters. *JoVE (Journal of Visualized Experiments)* e57239–e57239 (2018). doi:10.3791/57239

4.1 Introduction

As the field of tissue engineering has continued to mature, there has been increased interest in a wide range of tissue parameters, including tissue shape. Manipulating tissue shape on the micrometer to centimeter scale can direct cell alignment, alter effective mechanical properties, and address limitations related to nutrient diffusion.[1–3] In addition, the vessel in which a tissue is prepared can impart mechanical constraints on the tissue, resulting in stress fields that can further influence both cell and matrix structure. Shaped tissues with highly reproducible dimensions also have utility for in vitro assays in which sample dimensions are critical, such as whole tissue mechanical analysis.[4,5]

Replica molding, in which an object with a desired shape is created from a negative master mold, offers a convenient and low cost method of producing positive PDMS replicates. However, the required negative master molds are typically produced using microfabrication techniques that are expensive, time-consuming, limited in size, and require clean room space and sophisticated equipment. While 3D printing offers a potential alternative, its utility is somewhat limited due to the resolution limits of lower-cost printers and the chemical interactions between common 3D printer polymers and PDMS that can inhibit curing.

Conversely, negative master molds prepared from laser etched acrylic perform well with PDMS, permit designs with dimensions on the centimeter scale and feature sizes smaller than 25 µm, and can be rapidly designed and fabricated at low cost and with minimal expertise. These minimal time and cost requirements allow for laser etched molds to be rapidly iterated upon until an optimal design is determined, and to be easily adapted to suit any assay of interest.

4.2 Protocol

4.2.1 Create the Vector Format Master Mold Designs

1. Assemble the desired mold geometry in vector format using a vector graphics program (see Materials, Equipment, and Software Table). Select File| New and create a canvas of appropriate dimensions with RGB color format. Create the desired geometry using the shape tools in the left-hand panel: enter the desired dimensions at the top of the window (click the transform button at the top if not initially visible) to precisely define shape sizes.

   NOTE: Mold geometries should allow for at least a 6-mm border between the edge of the outermost features and the cutting line to permit trimming of the PDMS meniscus following mold casting. This will allow the finished mold to lay flush with the bottom of a culture dish. Further, mold geometries should take into consideration limitations associated with the laser cutter model that will be used, including kerf width and minimum feature size. The laser used for the work described herein (see Materials, Equipment, and Software Table) featured a 0.2 mm kerf width and a minimum etched feature size of 25 µm (maximum DPI of 1,000). Mold dimensions can be chosen to accommodate a desired culture vessel, such as a 10-cm dish, or 6- or 24-well plates.

2. Open the color picker in the top left-hand corner of the window and define new color swatches compatible with the laser cutter software.

   NOTE: We use red (RGB 255, 0, 0) for cutting and blue (RGB 0, 0, 255) for etching. Additional swatches can be defined depending on requirements for the design (for example, if more than one etching depth is desired). Assign these swatch colors to cutting paths by selecting the path and then selecting the cut swatch for the path color and [None] for the fill color from the color picker.

3. Similarly, assign swatch colors to etching paths by selecting the object and then selecting the etching path for the fill color and [None] for the path color from the color picker.

4. Save designs as either.ai or.pdf file formats, depending on the vector graphics program and laser cutter compatibility (Fig 2.1).

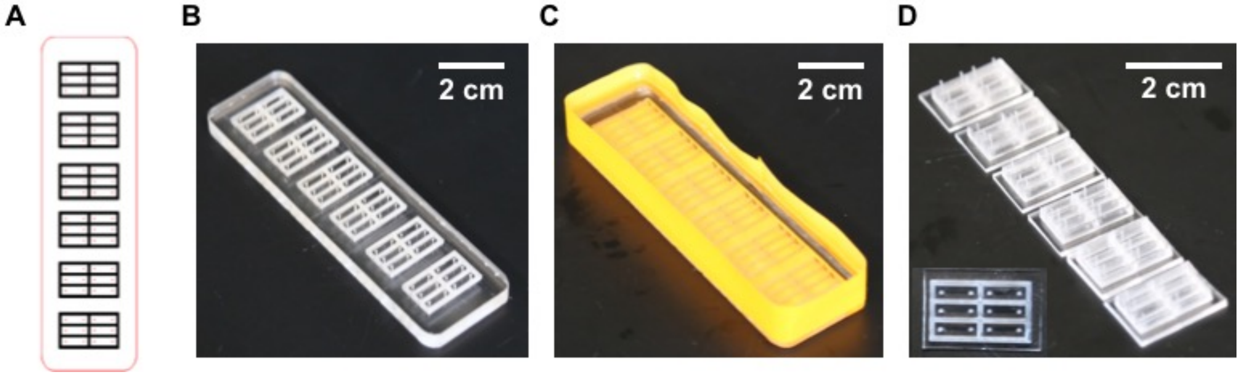

Figure 2. 1: Outline of the process for designing and preparing PDMS molds from laser cut acrylic masters. (A) Mold design prepared in vector graphics format. (B) Cleaned laser etched acrylic negative master. (C) PDMS cast on the surface of the taped acrylic master mold. (D) Resulting PDMS mold ready for sterilization prior to tissue culture. Inset: top view, same scale.

4.2.2 Laser Cut the Acrylic Master Molds

1. Select a negative master mold material.

   NOTE: Quarter-inch thick acrylic is well suited to this application due to its compatibility with laser cutting, relatively low cost, and thickness which allows for features up to ~ 5.5 mm in height. However, other materials that satisfy the following requirements may be used as well: (i) Non-reactive with PDMS curing; (ii) Non-porous/strongly adhesive to cured PDMS; (iii) Cuts and etches cleanly with a laser cutter; (iv) Maintains a glassy state up to 60 °C; (v) Of a thickness compatible with the desired maximum feature height.

2. Prepare the laser cutter for cutting according to the manufacturer's specifications. Ensure that sufficient ventilation is used and that the bed height is properly calibrated to the chosen negative master mold material's thickness.
3. Open the design file in a vectors graphics program on the computer connected to the laser cutter and click File| Print. Ensure that the laser cutter is set as the printer and that "Do Not Scale" is selected in the Scaling drop down menu to prevent distortion of the design before clicking the Print button at the bottom of the printing dialog.
4. In the laser cutter printing utility, click the Settings button in the bottom right-hand corner. Assign power, speed, and pulses per inch (PPI) settings to each of the previously chosen colors to set cut/etch parameters for all design features.

   NOTE: Here, the laser cutter equipped with a 75 W laser (see Materials, Equipment, and Software Table), used settings of the following: 100% power, 1% speed, and 1,000 PPI cuts cleanly through ¼" acrylic; 100% power, 8% speed, and 500 PPI etches to a depth of 2.75 mm in acrylic; and 100% power, 5% speed, 500 PPI etches to a depth of 3.50 mm in acrylic. If unknown for a laser cutter configuration or material, these parameters can be determined empirically through trial and error with a test piece.
5. Click the large green button in the laser cutter software to laser etch and cut the negative master molds.

6. Prepare the negative master molds for PDMS casting by removing any residual cutting debris with small brushes and/or compressed air (Fig 2.1 B).

4.2.3 Prepare the PDMS Molds for Cell or Tissue Culture

1. Prepare a PDMS casting mix according to its manufacturer's specifications. Prepare 0.35 mL/cm^2 of master mold; this will vary based on the mold features and height.
2. Degas the prepared PDMS in a vacuum chamber connected to a standard lab vacuum line (<500 mmHg) for 1 h, or until all bubbles have been eliminated.
3. Tape the outer edge of the mold with vinyl or masking tape (colored label tape works well) such that the tape extends >3 mm above the etched face of the negative master mold. Press the tape firmly against the side of the mold to prevent leaks later on.
   NOTE: If the acrylic master mold features through-holes, it may be necessary to apply tape to the bottom of the mold as well (Fig 2.1 C).
4. Pour the degassed PDMS over the etched face of the negative master mold.
   NOTE: The target PDMS thickness will depend on the application, though thick PDMS mold bottoms can make imaging challenging. A minimum thickness of ~ 1.5 mm strikes a good balance between imaging considerations and ease of mold removal.
5. Place the PDMS-coated negative master mold into a vacuum chamber and degas again for 1 h, or until all bubbles have been eliminated.
6. Place the degassed PDMS-coated negative master mold into a 60 °C oven to cure for at least 6 h. Ensure that the oven shelf is level. Alternatively, allow the PDMS to cure at 37 °C overnight, or at ambient temperature for ~ 72 h.
7. If multiple molds were cast on the same negative master mold, use a razorblade to cut these molds apart while they are still on the negative master mold. Then, peel each

PDMS mold off of the negative master mold. Ensure that PDMS molds are collected slowly and carefully to prevent mold feature tearing during collection.

8. Using a razor blade, trim off regions with the meniscus from casting, which would prevent the mold from lying flat, as well as any excess material or debris (Fig 2.1 D).
9. If necessary, prepare molds for cell/tissue casting by autoclaving.

4.2.4 Cast the Collagen and Fibrin Hydrogel Tissues

NOTE: Use a proper aseptic procedure to maintain sterility.

1. Adhere the molds to the bottom of the desired vessel. Adhere new molds to the bottom of a non-tissue culture treated plate by firmly pressing the mold against the untreated plastic (due to the hydrophobicity of PDMS).

   NOTE: However, if tissue-culture treated polycarbonate is to be used, or in the case of re-used molds, which tend to adhere less firmly, a natural or synthetic glue (such as fibrin or silicone sealant cured overnight) can be used to ensure attachment.
2. Prepare fibrinogen, thrombin, and neutralized collagen casting solutions such that the desired concentration of each will be achieved in the cast tissue. Keep collagen on ice until casting.

   NOTE: Fibrinogen and thrombin should not be allowed to mix until immediately prior to casting. If necessary, the fibrinogen and thrombin solutions can also be chilled to increase the polymerization time. We have used a final fibrinogen concentration between 0-8 mg/mL, a final thrombin concentration between 10 - 100 U/mL, and a final collagen concentration between 0.8 - 2.0 mg/mL (Fig 2.2). For engineered cardiac tissues, we often use cardiomyocytes at 12 x 10_6 cells/mL with 1.6 mg/mL, 4 mg/mL fibrinogen, and 20 U/mL thrombin (thrombin is added immediately prior to casting). Optimal concentrations (even outside of these suggested ranges) should be determined empirically.

3. Harvest cells following standard protocols and resuspend at a concentration appropriate to achieve the desired initial cell density in the cast tissue.

   NOTE: Human induced pluripotent stem cell-derived cardiomyocytes were harvested as described in Lian et al.[9] Keep the harvested cells on ice. Cell volume should be accounted for when preparing the cell suspension. We have used cell concentrations ranging from 9 - 18 x 10^6 cells/mL, though optimal ranges are expected to vary with cell population (Fig 2.2).

4. Combine the fibrinogen, neutralized collagen, and cell suspension (see step 4.2 for an example) to create a casting mix. Keep the casting mix on ice.

   NOTE: Fibrinogen and thrombin temperatures and concentrations will determine polymerization kinetics; in order to prevent polymerization during casting, it may be necessary to prepare separate batches of the casting mix depending on the number and volume of the constructs that will be cast.

5. Treat the surfaces of the mold that will be exposed to the casting mix to mitigate PDMS hydrophobicity (PDMS hydrophobicity will increase protein adsorption and make casting difficult).

   1. Achieve hydrophilic surface modification by treating with oxygen plasma, such as with a handheld high frequency generator (e.g., BD-20A from Litton Engineering). Expose all surfaces of the mold that contact the cell/gel mixture to the plasma treatment for 3 - 5 s, about 5 min before casting.

    2. Alternatively treat with a surfactant, like Pluronic F-127 (1% w/v)[10]. Perform the surface treatment as close to the casting time as possible, as the change in polarity will deteriorate over time.

6. Immediately prior to casting, add the thrombin to the casting mix and mix thoroughly by pipetting up and down without introducing bubbles.
7. Working quickly, pipette the casting mix into the molds, using care to deposit the mix into all corners and crevices of the mold. Avoid pipette ejection beyond the first stop to prevent bubble formation inside the constructs.
8. Repeat steps 4.6 and 4.7 as necessary for any additional batches of casting mix.
9. Place the tissue culture vessel in a 37 °C incubator for 45 min. If the incubator is not well humidified, deposit cell media around the molds prior to incubation to prevent construct dehydration.

   NOTE: The type of cell media will depend on cell type, but for engineered cardiac tissue constructs we use RPMI 1640 + B27 supplement.
10. After 45 min, return the constructs to the hood and cover with cell media before returning to the incubator.
11. Change the cell media every 48 - 72 h as needed for the cell and construct type.

    NOTE: Media change should be planned according to the recommended instructions provided by the supplier to ensure maximum cell health. Use care when changing the media to avoid disturbing the constructs. We have not experienced problems with constructs floating, but if this occurs, it may be prevented by adding tall posts to the mold design that extend beyond the media level.

12. After use, wash the molds sequentially with 10% bleach, 70% ethanol, and distilled water. Then air dry, and autoclave for re-use up to ~10 times.

4.3 Analysis Techniques: Tissue Compaction

NOTE: Compaction resulting from matrix remodeling is an indicator of tissue viability and development that can be easily measured through optical microscopy and image analysis.

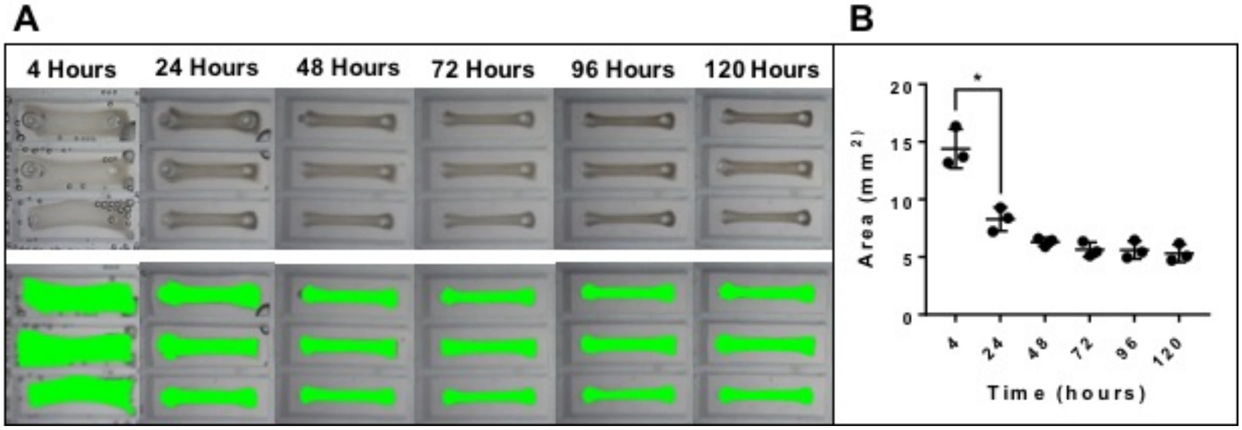

Figure 2. 2: Construct compaction over time in culture. (A) Images of rectangular constructs prepared in triplicate compacting over time in culture. Green overlays represent masks used to calculate visible construct area for image analysis. (B) Plot of construct area (a two-dimensional metric of construct compaction) over time. Horizontal lines represent the mean values and error bars indicate the standard deviation. For all groups, n = 3 and * indicates $p < 0.05$ as evaluated by ANOVA.

1. Collect optical microscopy images of the constructs in the molds at time increments ranging from 2 h to 96 h after casting.

   NOTE: Due to the low degree of magnification required, a dissection microscope with a camera mount is well suited to this application.

2. Trace the visible construct area in an image analysis suite such as ImageJ (open source, imagej.nih.gov/ij/).

3. Analyze the rate and final degree of compaction (Fig 2.2).

4.4 Analysis Techniques: Tensile Testing

Note: Both active mechanics (forces or strains generated by an engineered tissue because of cell activity) and passive mechanics (forces or strains generated in response to applied strains or forces) are critical functional characteristics of many engineered tissues, and this is particularly true for engineered cardiac tissues. The micromechanical analyzer used for the analyses is described in the Table of Materials. Other mechanical testing apparatuses could be similarly applied assuming they allow for hydrated testing and are capable of length control and force measurements over ranges and resolutions relevant for the tissue. For tissues with cross-sectional areas on the order of single square millimeters and stiffnesses on the order of tens of kPa, a 5 mN load cell is a good fit. Larger and stiffer materials would require a larger load cell. Prior to testing, ensure that both the force transducer and length controller are properly calibrated.

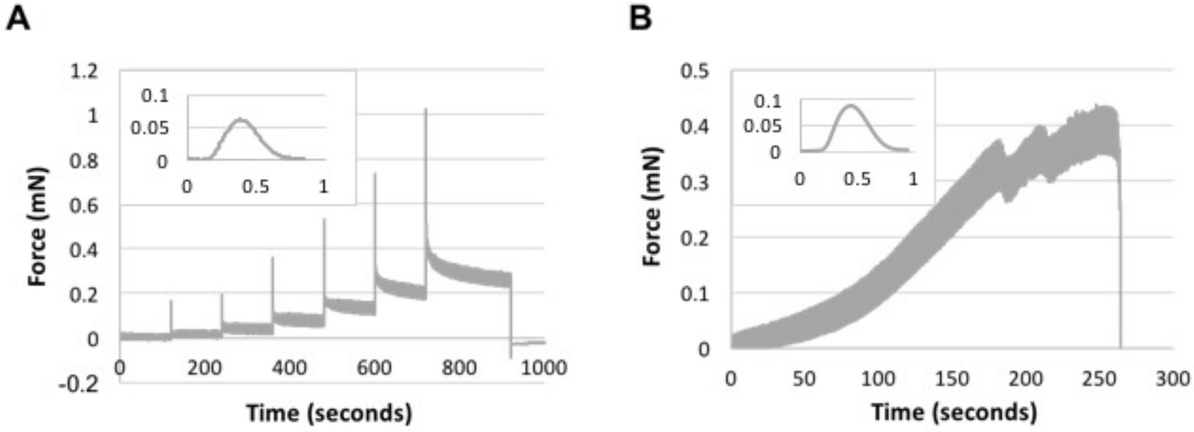

Figure 2. 3: Raw traces for mechanical characterization of engineered cardiac tissues. Insets display a single representative twitch contraction trace (same axes as main plot). (A) Active mechanical response resulting from rapid steps followed by holds at 5% strain increments. (B) Passive mechanical response resulting from a pull-to-break test at a rate of 10% strain/min. All samples were analyzed in a 37 °C bath of Tyrode's solution.

1. Turn on the length controller, force transducer, pulse generator, and temperature controller.

2. Fill the mechanical testing trough with Tyrode's solution (1.8 mM calcium chloride, 1.0 mM magnesium chloride, 5.4 mM potassium chloride, 140 mM sodium chloride, 0.33 mM sodium phosphate, 10 mM HEPES, and 5 mM glucose in ddH_2O, pH adjusted to 7.4) for engineered cardiac tissues. Adjust the thermocouple such that a bath temperature of 37 °C is achieved.

3. Load a mechanical testing protocol for collecting active contraction data.

   NOTE: We have evaluated active contractile mechanics using a length step protocol in which length steps in 5% strain increments up to 30% are held for 120 s to evaluate the impact of strain on contraction force (Fig 2.3 A). Additionally, we have evaluated passive mechanical properties through a pull-to-break protocol at a constant strain rate of 10% strain/min (Fig 2.3 B). Both of these protocols may serve as good starting points for active and passive mechanical analysis.

4. Under a dissection scope, carefully detach the engineered tissue construct from the PDMS mold, such that it is floating freely.

   NOTE: Cellularized constructs that have undergone tissue compaction will likely already be detached from the interior mold surfaces, and in those cases minimal manipulation is required.

   1. If compaction has not caused the construct to release, use forceps to gently separate the construct from the sides and bottom of the mold to avoid damaging the tissue.

5. Using forceps, gently pick up the construct and transfer it to the mechanical testing bath.

6. Viewing the construct through a dissection microscope, mount either end of the construct to the hooks attached to the force transducer and lever arm.

7. Adjust the lever arm position using the micromanipulator until the construct is positioned without applied strain. Zero the length controller and force controller.
8. Image the construct through the dissection scope so that the dimensions of the construct can be measured via image analysis.
9. Initiate the active force protocol and save the collected data once the protocol has been completed (Fig 2.3).
10. If passive mechanical data are required as well, adjust the lever arm again until there is zero applied strain. Zero the length and force controllers and image the construct a second time before loading and initiating the passive mechanics protocol (Fig 2.3). Save the collected data.

4.5 Analysis Technique: Paraffin Histology and Immunohistochemistry

Note: We have had the greatest success in imaging engineered tissue sections using paraffin blocks so that tissue morphology is best preserved. All steps of the process must be carefully considered and tailored to the engineered tissue, including processing samples without vacuum or pressure, empirically determining the appropriate antigen retrieval methods, and titrating the primary antibody concentration. Other techniques, such as using frozen blocks for preparing slides, may require less time and expense while yielding sufficient results depending on the intended application.

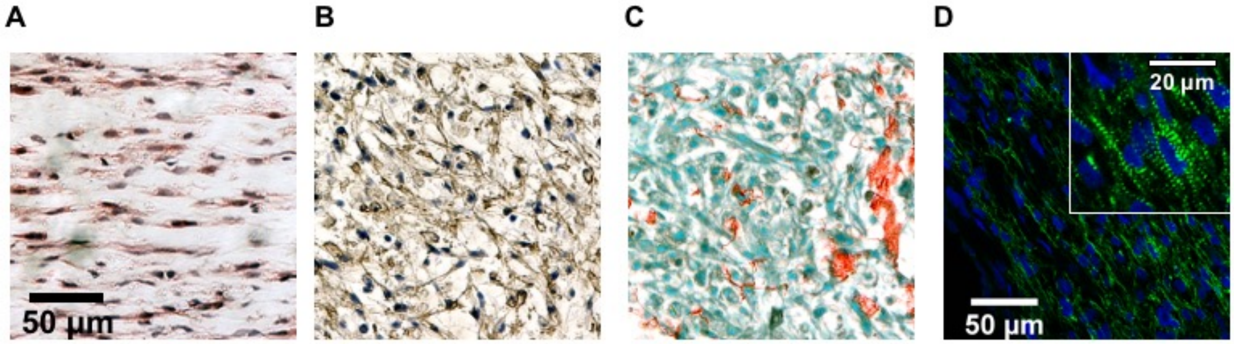

Figure 2. 4: Paraffin block histology images for engineered cardiac tissue constructs of various designs. Paraffin block histology images for engineered cardiac tissue constructs of various designs stained with (A) hematoxylin and eosin, (B) diaminobenzidine (anti-cardiac troponin T, brown), and hematoxylin nuclear counterstain, (C) picrosirius red stain for collagen with fast green cytoplasmic counterstain, and (D) mouse anti- α-actinin antibody (green) and 4',6-diamidino-2-phenylindole (DAPI) nuclear counterstain (blue). Cell alignment differs as a result of the construct design and tissue compaction. Scale bar in A applies to B and C as well. Inset in D shows striated cardiomyocytes.

1. Under a dissection scope, carefully detach the engineered tissue construct from the PDMS mold using forceps slid between the construct and PDMS to gently separate it from the PDMS, such that it is floating freely. Transfer these constructs to a microcentrifuge tube for fixation.

   NOTE: Fragile constructs or those to be fixed under the static stress condition provided by the mold itself may be fixed in the mold by changing solutions in the culture well and removing the construct from the mold after fixation.
2. Immediately fix the engineered tissues by submerging in 4% paraformaldehyde (PF) for 10 min at room temperature. Estimate no more than 1 h per 1 mm of tissue thickness; do not over-fix.
3. Rinse the tissues with phosphate buffered saline (PBS).
4. Keeping the tissue wet, place a drop of eosin on it to stain it pink for 10 - 30 s, and then rinse with 70% ethanol.

NOTE: The pink color helps to identify it in the paraffin block for sectioning later and will be washed away during deparaffinization.

5. Wrap the tissue in lens paper and place in a histology cassette. Use foam pads in the cassette as needed to keep the tissue flat.
6. Submerge the cassette in 70% EtOH and store at 4 °C until ready for paraffin processing.
7. Process the tissue by dehydrating it in increasing concentrations of ethanol (2 x 30 min each of 70, 95, and 100%). Then bathe samples in three sequential xylene baths for 30 min each.
8. Submerge the samples in three sequential paraffin baths for 30 min each.
9. Warm up the cassettes, carefully unfold and remove the eosin-stained tissue from the lens paper, and embed the paraffin-infiltrated tissue in a paraffin block. Be careful to lay the sample flat on the bottom of the mold to enable easier sectioning.
10. Section the tissues using a microtome as desired (5 - 8 μm thick) and stain using standard procedures optimized for the engineered tissue (Figure 2.4).

NOTE: An alternative to paraffin sections is to use frozen blocks, although morphology of the sample may be compromised. Place the fixed constructs in 30% sucrose in PBS for 3 h or until the specimen is equilibrated (e.g., overnight). Exchange the solution with 50/50 v/v 30% sucrose and optimal cutting temperature (OCT) freezing medium for 1 h. Place the constructs into frozen blocks with OCT freezing medium using a 70% EtOH with dry ice slurry for rapid block freezing in plastic trays. Section the blocks with a cryostat to 10 - 50 μm thick sections.

4.6 Analysis Technique: Cell Alignment

Note: Manipulating the tissue shape and internal stress fields can modulate cell alignment, a defining feature of many native tissues.

1. Prepare the engineered tissue constructs in PDMS molds with geometries of interest.
2. At the end of the culture period, wash the constructs in PBS, fix in 4% PF (see step 7.2) and harvest constructs to prepare for imaging by sectioning and histology (see Section 7) or whole mount staining.

   NOTE: Whole mount staining follows similar steps to histology/immunohistochemistry but requires longer incubation periods, and the penetration depth of dyes, the antibodies, and any imaging techniques (such as light penetration depth into the constructs) will need to be empirically determined for the construct composition.
3. Orient the tissue sections in the horizontal plane (parallel to the plane of the mold bottom) and stain for a marker for the cell of interest. Use an f-actin label, such as phalloidin, to mark the actin stress fibers of most cell types. Alternatively, use a cell specific marker.

   NOTE: In the case of engineered cardiac tissues, orientation was determined by sarcomeres stained with α-actinin.
4. Assess the major axis of all cells or nuclei in the region of interest manually or using an analysis tool (e.g., ImageJ, MATLAB).

NOTE: It may be useful to categorize different regions of the same construct, depending on the geometry (such as "node" and "bundle" regions in a mesh-like geometry, or "core" and "edge" in a circular geometry).

4.7 Representative Results

The optics of the laser cutter will cause etched areas to have very slightly decreased dimensions as etching depth increases, and results in mold walls with a very subtle bevel, due to tapering of the laser beam. This will help facilitate the removal of the cast PDMS molds, but should be carefully considered if very deeply etched negative master molds (>6 mm) are required (Fig 2.1).

Over time in culture, cellularized constructs will compact due to matrix remodeling, though the rate and extent to which this occurs will depend on the scaffold composition, cell load, and culturing conditions.

Matrix remodeling can occur through both reorganization and degradation of the surrounding matrix (as well as deposition of new matrix), but is typically associated with an increase in mechanical stiffness due to the decrease in cross-sectional area. With collagen-only constructs composed of 1.6 mg/mL collagen and 12 x 10_6 cardiomyocytes/mL, we see constructs compact to 19.7 ± 2.8% of their initial width over the four days following casting (Fig 2.2) via the compaction assay. While this assay yields a representative 2D approximation of a 3D process, the ease of data collection and non-destructive nature make it a powerful tool for studying the construct development process. Note that under cell culture conditions, even in the absence of cells, collagen mechanics can change over time due to both self-assembly and cross-linking[11]. Fibrin can be rapidly degraded by fibrinolysis both in vivo and in vitro if not in the presence of an antifibrinolytic, such as aprotinin or aminocaproic acid[12]. Therefore, the impact of scaffold components on long term tissue development, and not just tissue formation, should be considered when selecting a construct formulation. If final tissue size is important for a specific application, compaction must also be considered in mold design and empirically determined based on the cell type(s) and matrix composition. Note that tissue compaction can also induce stress fields within the tissue, which can be manipulated in cellularized constructs to encourage cell alignment (Fig 2.4).

A wide range of scaffold polymer concentrations and initial cell seeding densities have been used to create engineered tissues in the literature, and this can be attributed primarily to differing requirements for various cell types, cell lines, and applications. Based on our own work with hiPSC-derived cardiomyocytes, we believe that a collagen concentration of 1.25 mg/mL and a seeding density of ~ 15 million cells/mL is a good starting point[13]. Alternatively, fibrin is widely used as a cardiac tissue scaffold material as well, typically in the range of 3 - 4 mg/mL[14]. Cell seeding density may be selected based on a number of factors depending on the application, but the cell densities of native tissues provide a good reference point. Also consider that highly concentrated cell solutions can become challenging to work with, especially for small volumes. For a given cell population, the scaffold formulation can be tuned; generally by increasing the polymer concentration when tissues are too fragile or break upon compaction, and increasing the polymer concentration when tissues are too stiff or fail to compact[15].

Prior to performing passive mechanical analysis at any time point during culture, it may be appropriate to mechanically precondition the construct sample. Preconditioning of natural polymer hydrogels and engineered tissues will increase the reproducibility of the testing result due to material viscoelasticity and provide a better indication of the properties that the construct will exhibit in a clinical application. We use 8 cycles of 10% strain in a triangular waveform at a rate of 10% strain/min prior to starting mechanical assessment (Fig 2.3). Tissue and cell-type specific morphology can be assessed through histology and immunohistochemistry with traditional methods. However, we have found that optimization of nearly all steps of the paraffin processing, embedding, sectioning, antigen retrieval, and staining have been necessary for the engineered cardiac tissue compared to plated cells or sectioned native tissue (Fig 2.4).

4.8 Discussion

Customized PDMS mold geometries that are compatible with tissue culture have great utility in tuning important engineered tissue properties, such as cell alignment, diffusion rate, and effective stiffness. Additionally, these molds are very useful for preparing tissues for analysis applications in which geometry is important, such as mechanical testing[16,17]. Preparing these devices from laser cut negative master molds offers a rapid, facile, and low-cost method of utilizing these tools, especially when compared to the time and cost associated with traditional microfabrication. Laser cutting also permits a larger maximum mold size, limited only by the bed size of the cutter. We have successfully used these versatile molds to execute a wide variety of studies with engineered cardiac tissues, including optical mapping of action potential propagation, assessment of force production and passive mechanical properties, and implantation in a rat model of myocardial infarction[13,18]. We recognize that beyond the research niche of cardiovascular regenerative engineering, the applications for the fields tissue engineering, drug delivery, and materials research are vast.

While there are few technically challenging steps in the fabrication of the molds themselves, there are a number of critical steps involved in creating functional tissues. If constructs fail to compact the surrounding matrix after 24 h, first confirm the cell viability through viability staining of the engineered tissues. If cell viability is high, consider altering the construct composition for the next set of tissues. While outcomes will vary greatly depending on the cell population, we have observed increased compaction associated with higher seeding densities and lower collagen concentrations. Finally, it may also be useful to supplement the seeded cell population with a cell type well suited for matrix remodeling, such as fibroblasts, to encourage compaction.

One limitation of these molds is the potential for PDMS to adsorb small hydrophobic molecules. While for our applications this has not been problematic, it may be of concern in assays very sensitive to the loss of these molecules. In these cases, PDMS protein adsorption can be mitigated through treatment with an antifouling agent such as polyhydrophilic or polyzwitterionic materials[19]. Alternatively, a sterilized PDMS mold could be prepared as a negative master (from a laser-etched positive mold) for a culture mold to be cast in another, non-adsorbent material, such as agarose.

4.9 Acknowledgements

The authors acknowledge funding from NIH R00 HL115123 and Brown University School of Engineering. They are also grateful to the Brown Design Workshop and Chris Bull for training and support with the laser cutter.

4.10 References

1. Qin, D., Xia, Y., & Whitesides, G. M. Soft lithography for micro- and nanoscale patterning. Nat. Protoc. 5, 491 (2010).
2. Rogers, J. A., & Nuzzo, R. G. Recent progress in soft lithography. Mater. Today. 8, 50-56 (2005).
3. Whitesides, G. M., Ostuni, E., Takayama, S., Jiang, X., & Ingber, D. E. Soft Lithography in Biology and Biochemistry. Annu. Rev. Biomed. Eng. 3, 335-373 (2001).
4. Isiksacan, Z., Guler, M. T., Aydogdu, B., Bilican, I., & Elbuken, C. Rapid fabrication of microfluidic PDMS devices from reusable PDMS molds using laser ablation. J. Micromechanics Microengineering. 26, 035008 (2016).
5. Lee, K. Y., & Mooney, D. J. Hydrogels for Tissue Engineering. Chem. Rev. 101, 1869-1880 (2001).
6. Kloxin, A., Kloxin, C., Bowman, C., & Anseth, K. Mechanical properties of cellularly responsive hydrogels and their experimental determination. Adv. Mater. Deerfield Beach Fla. 22, 3484-3494 (2010).
7. Aubin, H. et al. Directed 3D cell alignment and elongation in microengineered hydrogels. Biomaterials. 31, 6941-6951 (2010).
8. Jaiswal, M. K. et al. Vacancy-Driven Gelation Using Defect-Rich Nanoassemblies of 2D Transition Metal Dichalcogenides and Polymeric Binder for Biomedical Applications. Adv. Mater. 29 (2017).
9. Lian, X. et al. Directed cardiomyocyte differentiation from human pluripotent stem cells by modulating Wnt/β-catenin signaling under fully defined conditions. Nat. Protoc. 8, 162-175 (2013).
10. Boxshall, K. et al. Simple surface treatments to modify protein adsorption and cell attachment properties within a poly(dimethylsiloxane) micro-bioreactor. Surf. Interface Anal. 38, 198-201 (2006).
11. Pins, G. D., Christiansen, D. L., Patel, R., & Silver, F. H. Self-assembly of collagen fibers. Influence of fibrillar alignment and decorin on mechanical properties. Biophys. J. 73, 2164-2172 (1997).

12. Pipan, C. M. et al. Effects of antifibrinolytic agents on the life span of fibrin sealant. J. Surg. Res. 53, 402-407 (1992).
13. Roberts, M. A. et al. Stromal Cells in Dense Collagen Promote Cardiomyocyte and Microvascular Patterning in Engineered Human Heart
Tissue. Tissue Eng. Part A. 22, 633-644 (2016).
14. Ye, K. Y., Sullivan, K. E., & Black, L. D. Encapsulation of Cardiomyocytes in a Fibrin Hydrogel for Cardiac Tissue Engineering. JoVE. (2011).
15. Zimmermann, W.-H. et al. Tissue Engineering of a Differentiated Cardiac Muscle Construct. Circ. Res. 90, 223-230 (2002).
16. McCain, M. L., Agarwal, A., Nesmith, H. W., Nesmith, A. P., & Parker, K. K. Micromolded Gelatin Hydrogels for Extended Culture of Engineered Cardiac Tissues. Biomaterials. 35, 5462-5471 (2014).
17. Hu, J.-J., Chen, G.-W., Liu, Y.-C., & Hsu, S.-S. Influence of Specimen Geometry on the Estimation of the Planar Biaxial Mechanical Properties of Cruciform Specimens. Exp. Mech. 54, 615-631 (2014).
18. Munarin, F., Kaiser, N. J., Kim, T. Y., Choi, B.-R., & Coulombe, K. L. K. Laser-Etched Designs for Molding Hydrogel-Based Engineered Tissues. Tissue Eng. Part C Methods. 23, 311-321 (2017).
19. Zhang, H., & Chiao, M. Anti-fouling Coatings of Poly(dimethylsiloxane) Devices for Biological and Biomedical Applications. J. Med. Biol. Eng. 35, 143-155 (2015).

CHAPTER 3: OPTIMIZING BLENDED COLLAGEN-FIBRIN HYDROGELS FOR CARDIAC TISSUE ENGINEERING WITH IPSC-DERIVED CARDIOMYOCYTES

Reproduced with permission from Kaiser, N. J., Kant, R. J., Minor, A. J. & Coulombe, K. L. K. Optimizing Blended Collagen-Fibrin Hydrogels for Cardiac Tissue Engineering with Human iPSC-derived Cardiomyocytes. *ACS Biomater. Sci. Eng.* **5**, 887–899 (2019).

5.1 Introduction

Over the past decade, the field of tissue engineering has witnessed increased focus on scaffold materials used to create engineered tissues, due to both improved understanding of the substantial role that substrates can play in cell development and function, as well as advances in material technologies in terms of customization, cost, and accessibility. Recent studies have shown that substrate material properties alone can significantly alter cell phenotype, growth rate, and differentiation pathway [1–3]. As a result, substrate and scaffold properties such as stiffness, remodeling rate, and ligand density have expanded material selection considerations well beyond simple biologic inertness. Concurrently, fabrication techniques such as electrospinning, wet spinning, salt leeching, and 3D printing with biocompatible polymers have necessitated the development of scaffold materials with both complex and extremely diverse properties and geometries, allowing for increased control over these very same variables[4–7].

However, these great strides in identifying, categorizing, and manipulating cell-materials interactions have not been matched with a comparable understanding of the mechanisms of cell-dense engineered tissue formation. Attempts to define the role of substrate parameters in cell or tissue function have typically been singular in their approach, evaluating the influence of a single variable on tissue function, which over-simplifies the interconnected parameter space of engineered tissues[8–10]. As a result, predictive tissue scaffold models have been limited in their scope[11–13]. Many of these characterization studies focus on responses exclusively at the cellular level and employ analytical formats and materials unsuitable for direct translation to tissue scale application. While more sophisticated statistical approaches are increasingly used to address other challenges related to tissue engineering, such as the optimization of stem cell differentiation[14,15], biomaterial fabrication[16], and imaging protocols[17], these same methods have not been applied to hydrogel-based cardiac tissues. This has led to the identification of tissue scaffold compositions for specific cell populations primarily through trial-and-error, and limited data has been published to justify the selected components.

Within the cardiac tissue engineering niche there are diverse and evolving approaches to producing engineered myocardium. Once common to the field, poorly defined additives and supplements derived from basement membrane, such as Matrigel® and Geltrex™, have largely been eliminated due to an emphasis on repeatability and translation. While both natural and synthetic polymer scaffolds are often used, simple hydrogels are often favored because of their ease-of-use and the ability to seed a high number of cells in a small volume, relative to other scaffold modalities such as pre-made scaffolds seeded later with cells. Natural polymers have a high density of cell binding sites, relatively high rate of remodeling by resident cells with non-toxic byproducts, and off-the-shelf availability. However, they are typically lacking in mechanical stiffness and strength that can be achieved with synthetic materials. Both collagen hydrogels with concentrations ranging from 0.5 to 1.5 mg/mL[18–23] and fibrin hydrogels with concentrations ranging from 2.0 to 4.0 mg/mL[24–26] have been used frequently as cardiac tissue scaffolds, but there is no evidence in the literature of these two hydrogels used in blends.

Research Group	Hydrogel Composition	Protein Concentration	Cell Type(s)	Seeding Density (cells/mL)
Black[25]	Fibrin	3.3 mg/mL	Neonatal rat CM	4.9e6
Coulombe[23]	Collagen I	1.25 to 1.5 mg/mL	hiPSC-CM	17e6
Eschenhagen[18,19]	Collagen I and Matrigel	0.56 to 0.89 mg/mL	Neonatal rat CM	1.1e6 to 11e6
Murry[20]	Collagen I and Geltrex	1.25 mg/mL	hiPSC-CM	20e6
Radisic[27,28]	Davol Ultrafoam + Matrigel	7.5 mg/mL	Neonatal Rat CM + C2C12	67e6 to 123e6
Tranquillo[24]	Fibrin	2 to 4 mg/mL	hiPSC-CM	3e6 to 5e6
Vunjak-Novakovic[29]	Porous PGS coated with laminin	N/A, Solid	Neonatal rat CM	146e6
Zimmerman[21]	Collagen I	0.8 to 1.2 mg/mL	iPSC-CM or Neonatal rat/mouse	2.5e6 to 3e6

Table 3. 1: **Composition of engineered cardiac tissue constructs reported in the literature.**

Collagen I is the predominant structural protein in the human body, as well as in native myocardium. Characterized by the triple helical molecular structure typical of all collagens, collagen I self-assembles into fibrils composed of interleaved individual molecules, which are further organized into collagen fibers of varying diameters in native tissue. In tissues exposed to high mechanical stresses, such as tendons, ligaments, and muscle, these fibrils and fibers are oriented parallel to the stresses, maximizing their tensile mechanical contributions. In the myocardium, collagen fibers are the primary component of the endomysium, forming the long channels that surround the cardiac muscle fibers and contributing to the anisotropy of native myocardium. While most collagen hydrogel scaffolds are initially unorganized, it has been demonstrated that organization can be imparted over time via stresses applied by resident cells[30].

Fibrin is a critical component of the wound healing cascade, wherein it provides vital, temporary structural reinforcement and stability to blood clots for hemostasis before degrading via fibrinolysis as the vessel wall is repaired and new extracellular matrix (ECM) deposited. In vivo, fibrin can be completely degraded just hours after polymerization[31,32]. Fibrin can also rapidly degrade in vitro due to plasmin and non-plasmin proteases present in cell media and produced by resident cells. When fibrin is used as a scaffold component it is typically used with a fibrinolysis inhibitor, such as aprotinin or aminocaproic acid, to increase fibrin persistence. Fibrin has great utility as a tissue scaffold due to its potential for rapid polymerization when exposed to thrombin (on the order of seconds to minutes) and due to its ability to be prepared at much greater concentrations than collagen (up to ~100 mg/mL compared to ~10 mg/mL), which facilities its use in forming tissue constructs and allows it to contribute substantially to construct mechanical properties.

Beyond scaffold composition, engineered cardiac tissues also differ significantly from each other in their initial cell population and seeding density. It is well accepted that there are functional differences between native cardiomyocytes and those derived from stem cells, but there can also be significant variability based on factors such as source animal species and age, passage number, purity, differentiation protocol, and even differentiation batch[33–35]. Due to the low growth rate of mature cardiomyocytes (from 1% in adult native cardiomyocytes[36] to 2.7% in 6 week old human embryonic stem cell derived cardiomyocytes[37,38]) the initial seeding density of cardiomyocytes in the fabrication of engineered myocardium is also a major factor in driving cell-scaffold interactions and tissue formation. Seeding density values from the literature range widely from 2.5 to 17 million cells/mL[21–23,25]. For all of these reasons, there is unlikely to be a single engineered myocardium scaffold that yields desired results with all cell types and seeding densities, but rather a spectrum of scaffold parameter sets that can be tuned to compliment a given cell population.

Herein, we present an innovative approach to characterizing the impact of both cell population and scaffold composition on engineered myocardium formation and function. We believe that employing a multifactor design of experiments approach, entirely in a 3D format, will yield a more complete understanding of the ways in which cells and scaffolds interact to form functional engineered tissues. It is our aim that this study will serve as a foundation for the development of more sophisticated and highly functional engineered cardiac tissues in the future.

5.2 Materials and Methods

5.2.1 Fabrication of PDMS Tissue Molds

Custom polydimethylsiloxane (PDMS) molds with rectangular troughs 3 mm wide and either 9 mm or 17 mm long were used to prepare cellularized and acellular hydrogels, respectively, for tensile mechanics and compaction characterization. Circular molds 5 mm in diameter were fabricated for acellular compression mechanics. All molds were fabricated using a previously described technique utilizing laser cut acrylic master molds[39,40]. Briefly, negative acrylic master molds were designed in Adobe Illustrator (Adobe System Inc., San Jose, CA) and then fabricated on a ULS 6.75 model laser cutter equipped with a 75 watt laser. Sylgard® 184 (Dow Corning, Midland, MI) PDMS was prepared according to the manufacturer's specifications (10:1 base:curing agent) and cast over the etched surface of the master mold. Molds were cured overnight in a 60°C oven, autoclaved, and then positioned at the bottom of the wells of an untreated polystyrene six well plate. No adhesive was necessary to hold the molds in place in the wells for the new PDMS molds, likely due to the hydrophobicity of both the PDMS and polystyrene surfaces.

5.2.2 Cardiac Differentiation and Lactate Purification

Cardiomyocytes were differentiated from human induced pluripotent stem cells (hiPSCs; Gibco human episomal iPSCs or GCaMP6 WTC hiPSCs from The Gladstone Institutes) using chemically defined conditions and small molecule modulation of the Wnt signaling pathway as previously described[23,39]. Briefly, hiPSCs cultured on vitronectin (Gibco™)-coated 10 cm polystyrene tissue culture plates were treated with 6 µM Chiron 99021 (Tocris), a glycogen synthase kinase 3 (GSK3) inhibitor at day 0, followed by 5 µM IWP2 (Tocris), a Wnt inhibitor at day 3. Cardiac phenotype, demonstrated by beating behavior, is typically first observed between day 10 and day 14. Cardiomyocytes differentiated from hiPSCs were used for the fabrication of cellularized constructs between differentiation day 14 and 18, unless designated for lactate purification. Cardiomyocytes designated for lactate purification were harvested on day 15 and replated to new culture vessels coated with Matrigel on day 15 in RPMI+B27. These cells were deprived of media change from day 16 to 19 and were fed with lactate media (DMEM without glucose, L-glutamine, phenol red, sodium pyruvate and sodium bicarbonate (D-5030, Sigma) + 4 mM L-glutamine, 1X Non-Essential Amino Acids, and 4 mM lactate, pH 7.4) on day 20 and day 22. Lactate purified cells were fed with RPMI+B27 on day 24 and then harvested to seed tissues on day 26. Cardiac purity was measured via flow cytometry analysis on every batch of cells used for the preparation of cellularized constructs. Purity was defined by the percentage of cardiac troponin T (cTnT) positive cells.

5.2.3 Preparation of Collagen and Fibrin Hydrogels Seeded with hiPSC-derived Cardiomyocytes

Detailed methods for preparing collagen and fibrin hydrogel constructs seeded with cardiomyocytes have been described previously[39,40]. Briefly, prior to cellularized construct preparation, custom molds were prepared for tissue culture by placing autoclaved PDMS molds at the bottom of the wells of an untreated six well plate and treating with oxygen plasma to reduce the hydrophobicity of the PDMS surface.

Blended collagen I and fibrin hydrogels seeded with cardiomyocytes were prepared by combining neutralized collagen, fibrinogen, thrombin, and cell precursor mixtures immediately prior to casting. The collagen precursor mix was prepared by neutralizing a 4.0 mg/mL rat collagen I commercial stock solution (Advanced Biomatrix, San Diego, CA) with 1M sodium hydroxide to a pH of 7.4, supplementing with 10X RPMI 1640 medium, and further diluting with DI water to achieve 1X RPMI, as well as the targeted collagen concentration (ranging from 0.8 to 1.6 mg/mL) in the casting mix. The fibrinogen precursor mix was prepared by diluting a 100 mg/mL bovine fibrinogen stock solution in construct media (RPMI with B27 supplement, Gibco™; RPMI+B27, supplemented with bovine aprotinin to achieve 50 U/mL aprotinin) as well as the targeted fibrinogen concentration (ranging from 0 to 20 mg/mL) in the casting mix. Finally, the cell precursor mix was prepared by resuspending harvested cardiomyocytes in RPMI+B27 to achieve the desired seeding density (9, 12, or 15 million cells/mL) in the casting mix. The collagen precursor mix, cell precursor mix, and cast mix were all kept on ice prior to casting. In the case of the fractional factorial methodology studies, the precursor mixes were combined in the wells of a chilled, untreated, 96 well plate to accommodate the large number of unique formulations. Thrombin was added immediately prior to casting. Specific formulations for the fractional factorial and response surface methodology studies were preferentially chosen based on which would lend the greatest amount of statistical information to the respective models[41,42]. Constructs were stimulated at 1 Hz (section 2.4) during culture at 37°C and 5% CO_2, fed with construct media every 48 hours, and supplemented with 50 U/mL aprotinin every day between feeds to mitigate fibrinolysis.

5.2.4 Electrical Stimulation of Hydrogels Seeded with hiPSC-derived Cardiomyocytes

All cellularized constructs were stimulated for the duration of the culture period using a C-Pace EP system with six-well C-dish electrode assembly lids (IonOptix). This system is composed of stimulator lids with pairs of carbon electrodes for each well of a six well plate. Carbon electrodes extend into the culture medium and are positioned on opposite sides of the engineered tissues. A ribbon cable connects the stimulator lid to the stimulator bank outside of the incubator. Constructs were field stimulated with a 1 Hz, 10.0 V, 4.0 ms duration bi-polar pulse train for the full culture period.

5.2.5 Preparation of Acellular Collagen and Fibrin Hydrogels

Acellular hydrogels were prepared using the same methodology as the cellularized constructs with the cell precursor mix and construct media replaced by PBS. Additionally, rather than treating the PDMS surface with oxygen plasma prior to casting, the troughs of the PDMS molds were lightly coated with canola oil to facilitate hydrogel release.

5.2.6 Mechanical Characterization of Hydrogels and Constructs

a. Acellular Hydrogels

Acellular blended collagen and fibrin hydrogels were evaluated in both compression and tension. Compression testing was performed on 5 mm diameter hydrogel discs cast 1.88±0.06 mm thick, prepared using custom PDMS molds. Hydrogels were allowed to polymerize for one hour at either 4°C or 37°C, and were then incubated for either 1 or 72 hours at 37°C in PBS in the dark. Sample thickness was measured with a micrometer immediately prior to testing. All compression testing was performed unconfined, between two flat platens, with a 1 kN load cell, at a constant strain rate of 1 mm/minute (Instron E1000) until the limit of the load cell was reached. Compressive Young's modulus was determined from a near-linear portion of the stress-strain curve in the physiological range, usually between 0 and 5 percent strain, and is referred to as compressive stiffness throughout.

A subset of the acellular hydrogel formulations tested in compression, chosen to span the range of compressive stiffness values observed, were selected for further evaluation under tension. Acellular tensile samples were cast in custom 3 mm x 17 mm PDMS troughs, 1.29±0.05

mm thick, with 0.5 mm diameter posts at either end. Samples were allowed to polymerize for one hour at 37°C and then incubated further for either 1 or 72 hours of incubation at 37°C. Prior to testing, samples were cut in half crosswise and thicknesses were measured with a micrometer while widths and lengths were measured with calipers. Each half of the construct was tested under tension on a micromechanical system (Aurora Scientific) equipped with a 5 mN load cell in a bath of PBS at 37°C. All samples were tested at a constant strain rate of 1 mm/min until failure. Tensile Young's modulus was determined from the linear region of the stress-strain curve, usually between 15 and 25 percent strain, and is referred to tensile stiffness throughout.

b. Cellularized Constructs

Both active and passive tensile mechanical properties were analyzed for beating cellularized cardiac tissue constructs. Cellularized constructs were prepared in custom PDMS molds with troughs 3 mm (W) x 9 mm (L), with 0.5 mm diameter posts at either end of the troughs. Constructs were mechanically evaluated after six days of culture at 37°C with 1 Hz stimulation. Uniformity of beating was visually assessed and assigned a score of 0 for no beating, 1 for localized regional beating, or 2 for uniform beating throughout tissue. After mounting the tissue on the mechanical setup and immediately prior to testing, bright field optical microscopy images were collected (Olympus SZ40) for later image analysis to determine initial sample dimensions. Both active and passive mechanical testing was performed in a 37°C bath of Tyrode's solution (1.8 mM $CaCl_2$, 1.0 mM $MgCl_2$, 5.4 mM KCl, 140 mM NaCl, 0.33 mM NaH_2PO_4, 10 mM HEPES, 5 mM Glucose). Resting tension was set to 10% above slack length. Active mechanical testing was performed by measuring construct contraction force at strains of 5, 10, 15, 20, 25, and 30 percent, held for 120 seconds at each length to allow for stress relaxation and electrically stimulated at 1 Hz during the final 20 seconds of each step to capture twitch contractions. Peak active stress is calculated at 0.3 strain, normalized for cross-sectional area. The rate of force or calcium rise is reported as upstroke velocity, V_{up} (in units of stress/time or normalized calcium amplitude/time, respectively). Passive testing uses eight precondition cycles at a rate of 1 mm/min to 10% strain followed by pull-to-break at the same rate until sample failure. Young's modulus was determined from the linear region of the stress-strain curve, usually between 15 and 25 percent strain.

5.2.7 Mechanical Analysis of Native Rat Myocardium

Passive mechanical properties were analyzed for samples of native rat myocardium. All animal procedures were conducted in accordance with the U.S. NIH Policy on Humane Care and Use of Laboratory Animals and the Brown University and Rhode Island Hospital Institutional Animal Care and Use Committee (IACUC protocol No. 1310000025). Immediately after harvest, whole rat hearts were washed, ventricles open to expose the endocardium, and stored in Tyrodes solution with a protease inhibitor cocktail at 4°C. Tissue samples were dissected and analyzed within 6 hours. Compression samples were collected as discs with sharp dissection via a 5 mm biopsy punch through the full thickness of the left ventricular myocardial layer. Compression testing was performed unconfined, between two flat platens, with a 1 kN load cell, at a constant strain rate of 1 mm/minute until the limit of the load cell was reached. Young's modulus was determined from the linear portion of the stress-strain curve, usually between 0 and 5 percent strain. Tensile samples were collected as strips approximately 2 mm x 10 mm via sharp dissection with microsurgical spring scissors from the myocardial layer. Special care was taken to collect tensile samples with a long axis either parallel to the circumferential epicardial muscle fibers (referred to as longitudinal samples) or perpendicular to these muscle fibers (referred to as transverse samples). Tensile testing was performed in a 37°C bath of Tyrode's solution with eight preconditioning cycles at a rate of 1 mm/min to 10% strain followed by pull-to-break at the same rate until sample failure. Young's modulus was determined from the linear region of the stress-strain curve, usually between 15 and 25 percent strain.

5.2.8 Construct Compaction Assay

Construct compaction was evaluated through a non-destructive, longitudinal imaging assay. Cellularized tissues cast in custom PDMS troughs 3 mm x 9 mm were prepared in six-well plates as described above. Constructs were imaged via bright field optical microscopy at 4, 24, 48, 72, 96, and 120 hour timepoints. Images were then analyzed in ImageJ (Schneider, 2012) to determine visible two-dimensional construct areas.

5.2.9 Immunofluoresence Staining and Sarcomere Length Analysis

Immunostaining was performed as previously described[23]. Briefly, cellular constructs were fixed immediately after mechanical testing in 4% paraformaldehyde (MilliporeSigma) for 10 minutes then processed into frozen blocks with OCT and sectioned into 5 µm slices. Sections underwent antigen retrieval with a proteinase K digest (10 µg/mL; Roche) for 5 minutes at 37°C prior to staining for sarcomeric alpha-actinin (α-actinin), connexin 43 (Cx43), and cell nuclei (DAPI). Images were taken with an Olympus FV3000 Confocal Microscope and processed using ImageJ. Sarcomere length was analyzed by taking the average distance between the midpoint of continuous sarcomeres for regions with a minimum of 3 visible bands aligned with the major axis of the construct.

5.2.10 Statistical Analysis

All statistical analyses were performed in Prism 7 (GraphPad Inc., San Diego, CA). For comparison between two groups, Student's t-tests were used. For comparisons of more than two groups, one way analysis of variance (ANOVA) with multiple comparisons and Tukey's post-hoc test was used. Error bars represent standard error of the mean unless otherwise noted. Group differences were considered statistically significant for p-values < 0.05.

5.3 Results

5.3.1 Collagen and Fibrin Modulate Acellular Construct Stiffness

Investigation of acellular blended hydrogel compressive mechanical properties was performed via a two-level fractional factorial approach to assess how these natural matrix proteins interact in the absence of cellular remodeling. A total of five hydrogel formulations and processing parameters were considered, namely collagen concentration, fibrin concentration, aprotinin concentration, polymerization temperature, and time in culture. Two levels were evaluated for each factor, referred to as "low" and "high" for convenience. Low and high factor levels were chosen based on the lower and upper bounds of tolerances necessary for cell viability, historical data from our lab[23,39], and values previously reported in the literature[21,22,25–27,43] (Table 1). Higher levels of collagen and fibrin were chosen to emulate the density of ECM in compacted engineered tissues for analysis of acellular samples. The fractional factorial approach leverages linear regression statistics to reduce the number of trials that must be conducted to quantify the impact of each factor on a response, at the cost of the ability to isolate high order interactions from the system. According to the sparsity-of-effects principle, such interactions are rare and are unlikely to have a significant effect on a response of interest[41]. Sixteen individual hydrogel formulations were defined as combinations of these high and low levels for each factor and tested in compression (Fig 3.1 B).

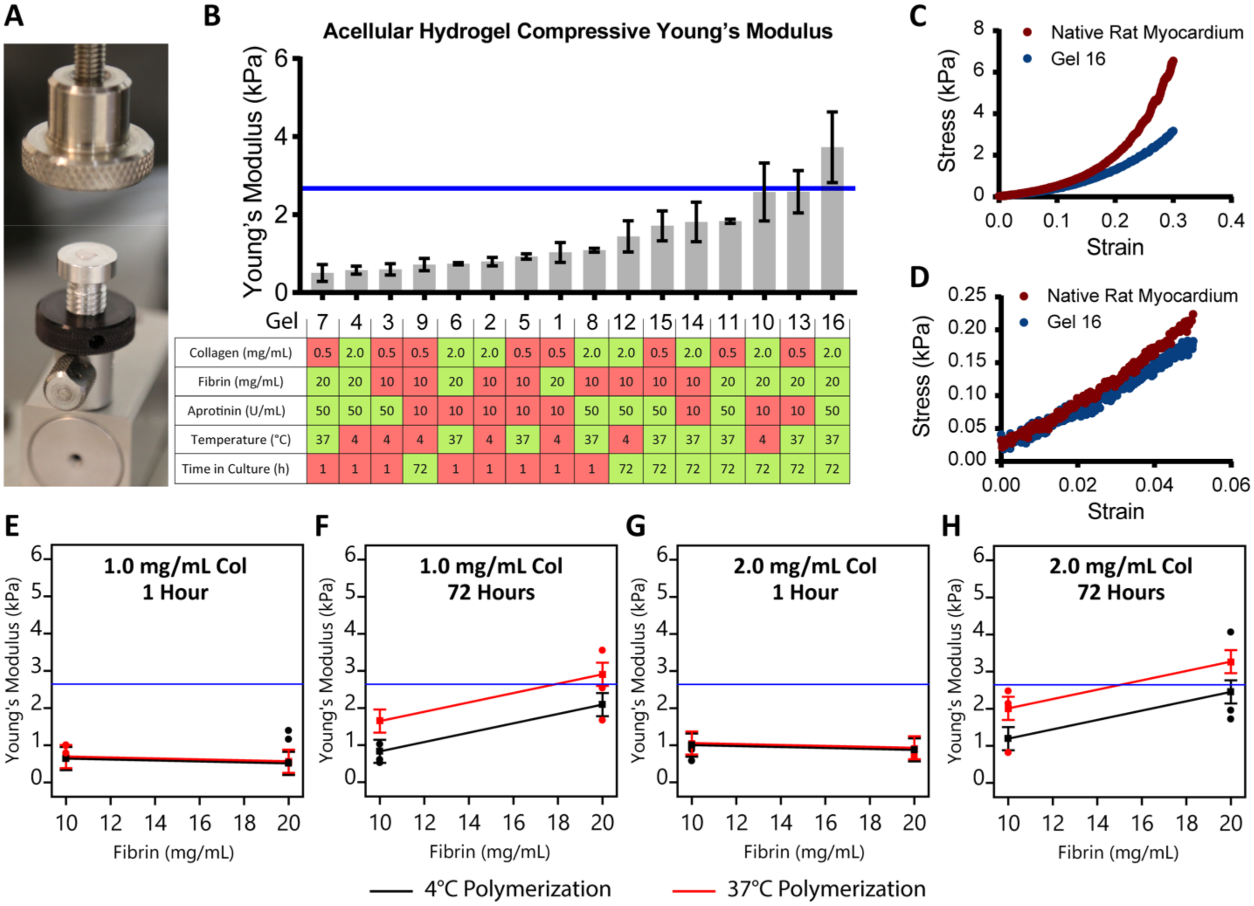

Gel	7	4	3	9	6	2	5	1	8	12	15	14	11	10	13	16
Collagen (mg/mL)	0.5	2.0	0.5	0.5	2.0	2.0	0.5	0.5	2.0	2.0	0.5	2.0	0.5	2.0	0.5	2.0
Fibrin (mg/mL)	20	20	10	10	20	10	10	20	10	10	10	10	20	20	20	20
Aprotinin (U/mL)	50	50	50	10	10	10	10	10	50	50	50	10	50	10	10	50
Temperature (°C)	37	4	4	4	37	4	37	4	37	4	37	37	37	4	37	37
Time in Culture (h)	1	1	1	72	1	1	1	1	1	72	72	72	72	72	72	72

Figure 3. 1: Unconfined compression of acellular blended hydrogels and native rat myocardium. (A) Unconfined compression testing apparatus with hydrogel disc on platen. (B) Unconfined compressive Young's modulus of hydrogel formulations shown from least to most stiff, with the formulation and processing parameters for each gel defined in the table below. Red boxes indicate low factor levels and green boxes indicate high factor levels. The blue line indicates the mean unconfined compressive Young's modulus of adult rat myocardium tested under the same conditions. (C and D) Representative unconfined compressive stress-strain plots for rat myocardium and Gel 16 from 0 to 30% and 0 to 5% strain, respectively. (E - G) Interaction plots for the influence of polymerization temperature, time in culture, and fibrin concentration on hydrogel stiffness. Black symbols and lines represent the low polymerization temperature (4°C), while red symbols and lines represent high polymerization temperature (37°C). Blue lines represent mean compressive stiffness of adult rat myocardium.

Unconfined compressive Young's modulus values ranged from 0.50±0.22 to 3.73±0.91 kPa across all formulations, spanning the mean value measured for native rat myocardium (2.67±0.61 kPa, Fig 3.1 B). Both hydrogels and native myocardium stress/strain curves demonstrated strain-stiffening phenomena typical of natural polymers and native tissue. High levels of both time in culture and polymerization temperature were associated with increased hydrogel compressive stiffness (green squares in table of Fig 3.1B), and were found to be significant factors ($p<0.05$) in the fractional factorial analysis (see Table S4). Collagen concentration and aprotinin concentration had no significant impact on blended hydrogel compressive stiffness. The stiffest gel, number 16, showed good agreement with the non-linear toe region of native rat myocardium (Fig 3.1 C), particularly in the physiological range of strain (Fig. 3.1 D). Interestingly, high fibrin concentration also significantly increased hydrogel stiffness, but the increase was only apparent after 72 hours of incubation in PBS in the dark (Fig 3.1 E-H). While the fibrin and thrombin concentrations were sufficient to induce polymerization within 5 – 10 minutes, well before the start of testing, it is possible that additional crosslinks or molecular interactions (including fibrin-fibrin or fibrin-collagen interactions) developed during the extended incubation, which altered the compressive mechanical properties associated with initial fibrin concentration.

Native myocardium experiences both compressive and tensile forces in vivo[44], and for this reason, tensile testing was done on a subset of four formulations, spanning the range of measured compressive stiffness values and containing high (2 mg/mL) collagen. For comparison, rat cardiac tissue samples were characterized in both long and transverse fiber directions (see details in methods section 2.7) due to the anisotropic architecture of native myocardium.

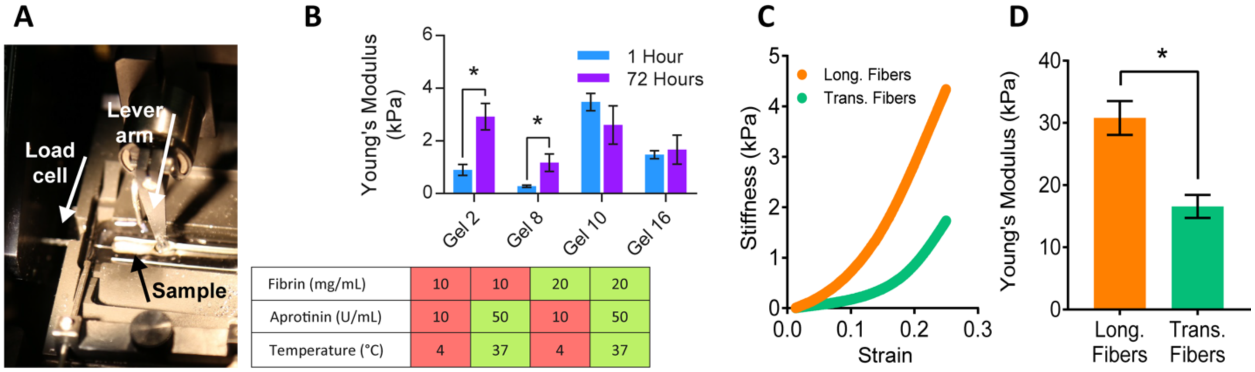

Fibrin (mg/mL)	10	10	20	20
Aprotinin (U/mL)	10	50	10	50
Temperature (°C)	4	37	4	37

Figure 3. 2: Tensile analysis of acellular blended hydrogels and native rat myocardium. (A) Micromechanics setup consisting of a 37°C PBS bath with platinum electrodes, lever arm of rapid stepper motor (right), and 5 mN load cell (left) used for mechanical analysis. (B) Young's modulus for hydrogel formulations (n=3 for all groups) for 1-hour (blue) and 72-hour (purple) samples (n=3, $*P<0.05$). (C) Representative stress/strain curves for longitudinal (Long., orange) and transverse (Trans., teal) fiber native rat myocardium samples. Note distinct toe regions under 20% strain. (D) Mean adult rat myocardial stiffness data collected from samples prepared with long and transverse fiber orientations collected from two adult rats (n=5, $*P<0.05$).

Tensile stiffness ranged from 0.28±0.04 to 3.48±0.33 kPa, which was well below the tensile stiffness values found for native rat myocardium (30.80±2.71 kPa in the long fiber direction and 16.58±1.85 kPa in the transverse fiber direction, Fig 3.2 B-D). These stiffness values and the anisotropic ratio of approximately 2:1 are similar to values reported in the literature[45,46]. Again, both the hydrogels and native myocardium stress/strain curves demonstrated strain-stiffening phemona. Gels with low fibrin concentrations had lower stiffness values versus those with high fibrin concentrations at one hour (blue bars, Fig 3.2 B). However, tensile stiffness of both of the low fibrin concentration gels increased after 72 hours of culture, while there was no significant change in tensile stiffness of the other groups with culture time. This may indicate that collagen assembly enabled increased tensile stiffness at 72 hrs in gels with low fibrin (purple bars in gels 2 and 8, Fig 3.2 B), and that either increased fibrin presence interfered with collagen fibril formation or there was no additive benefit of high fibrin to tensile stiffness at 72 hours in gels with high fibrin (purple bars in gels 10 and 16, Fig 3.2 B), limiting the tensile stiffness of the material.

5.3.2 Tissue Formulation Influences Compaction

Analysis of the acellular blended hydrogels indicated that fibrin concentration was the most direct method of manipulating blended hydrogel tensile and compressive stiffnesses, with time in culture and collagen concentration playing lesser roles. Knowing that cellular adhesions to the matrix proteins would significantly remodel the tissue with time, we hypothesized that an optimum tissue formulation could be defined by testing a wider range of fibrin concentrations without changing other parameters using hiPSC-derived cardiomyocytes. However, when cellularized constructs were prepared with fibrin concentrations ranging from 5 to 20 mg/mL in the presence of 2 mg/mL collagen, constructs failed to compact and resume a beating phenotype two of the three times the experiment was repeated (Fig A1.2 A). Flow cytometry analysis of cardiac purity based on cTnT protein expression revealed differences in construct diameter for cardiac purities ranging from 13% to 77% cTnT$^+$, suggesting purity plays an important role in tissue development by modulating tissue compaction. Considering that tissue compaction, a process through which resident cells adhere to and remodel the surrounding matrix, is a necessary precursor to functional cardiac tissue formation, a pilot study was conducted to evaluate the role of collagen concentration and seeding density on tissue compaction (Fig. A1.2 B). This study had 49.7% cTnT$^+$ cells and used a narrowed range of collagen, from 0.8 to 1.2 mg/mL, based on what is prevalent in the literature (see Table 1) and had worked successfully for our lab in the past[23,39]. This pilot study showed that higher cell density (pink lines) and lower collagen concentration (lighter colors) enabled the greatest compaction (i.e. smallest construct diameter; Fig A1.2). Together, these experiments with cellularized constructs suggest that collagen concentration, fibrin concentration, seeding density, and cell purity all impact construct compaction, and therefore merit inclusion as factors in a broader set of cell-based experiments.

To evaluate tissue formation, a response surface methodology (RSM) approach was chosen to assess the impact of each factor and two-level factor interactions on tissue compaction rather than using an empirical approach that would require a higher number of test groups. Collagen concentration, fibrin concentration, and seeding density were each considered as factors, each with three evenly spaced levels, in each iteration of the compaction assay experiment. Low, medium, and high levels for each factor were selected based on values from the literature (Table 1) and informed by the acellular mechanics and pilot compaction studies (see Table 2). By traditional methods, this selection of factors and levels would have required the evaluation of 27 groups in triplicate, for a total of 81 constructs.

	Low	**Medium**	**High**
Collagen (mg/mL)	0.8	1.2	1.6
Fibrin (mg/mL)	0	4	8
Seeding density (1x10^6/mL)	9	12	15

Table 3. 2: Factors and levels considered in each run of the compaction assay.

Instead, specific formulations to test were selected based on a standard three factor, three level Box-Behnken design[41]. This design format prescribed thirteen construct formulations, each of which was prepared in triplicate in each run of the experiment. Additionally, one center point group was repeated across each of the two six-well plates used for each experiment as a control to assess and minimize variability between plates, for a total of 42 constructs in each run of the experiment with a single batch of hiPSC-derived cardiomyocytes (Fig 3.2).

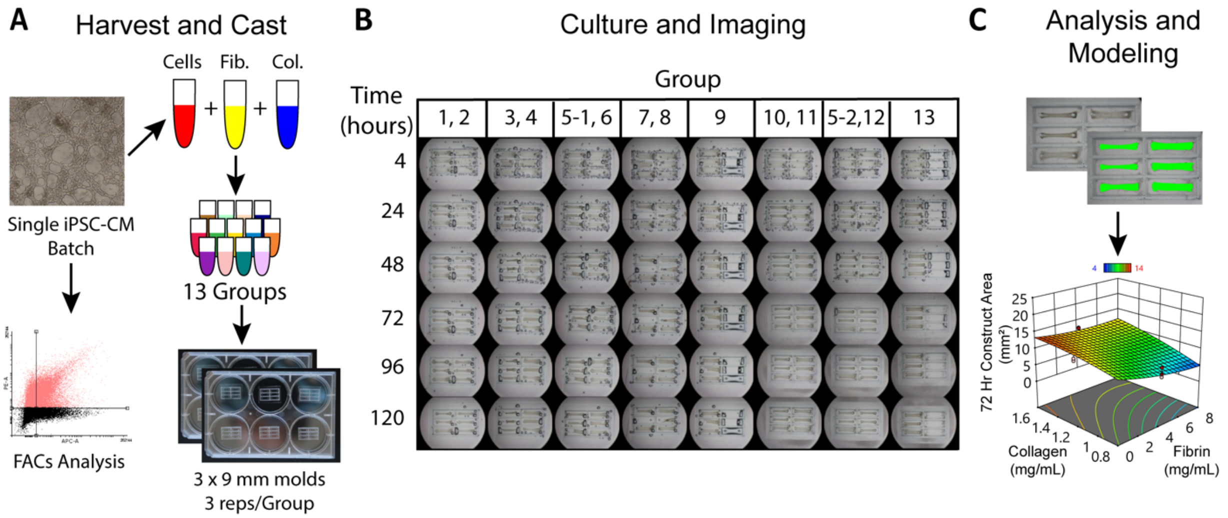

Figure 3. 3: Compaction assay schematic for a single iPSC-CM batch. (A) One batch of iPSC-CMs is harvested, a FACs sample is collected, and the remaining cells are incorporated into one of thirteen sample groups dictated by the Box-Behnken design. Construct suspensions are each used to cast three 35 μL constructs in 3 x 9 mm PDMS wells (the center point Group 5 was repeated as 5-1 and 5-2 to account for variability between plates). (B) Throughout culture, samples were imaged at time points 4 – 120 hours (left row labels) to monitor compaction. (C) Visible construct 2D area was measured via image analysis software as a metric of construct compaction. These results were used to build a response surface model (RSM) for compaction at each time point. Results from multiple experiments and iPSC-CM batches were used to build a predictive model incorporating iPSC-CM purity as a factor.

To incorporate cardiomyocyte purity as a fourth factor, the full experiment was repeated three times with discrete batches of hiPSC-derived cardiomyocytes. Flow cytometry samples collected during harvest were used to assign a cardiomyocyte purity to each run. Data collected across three of these runs with purities of 24.4%, 30.2%, and 60.2% was successfully incorporated into a single significant predictive model, with a non-significant lack-of-fit to the collected data (Fig 3.4).

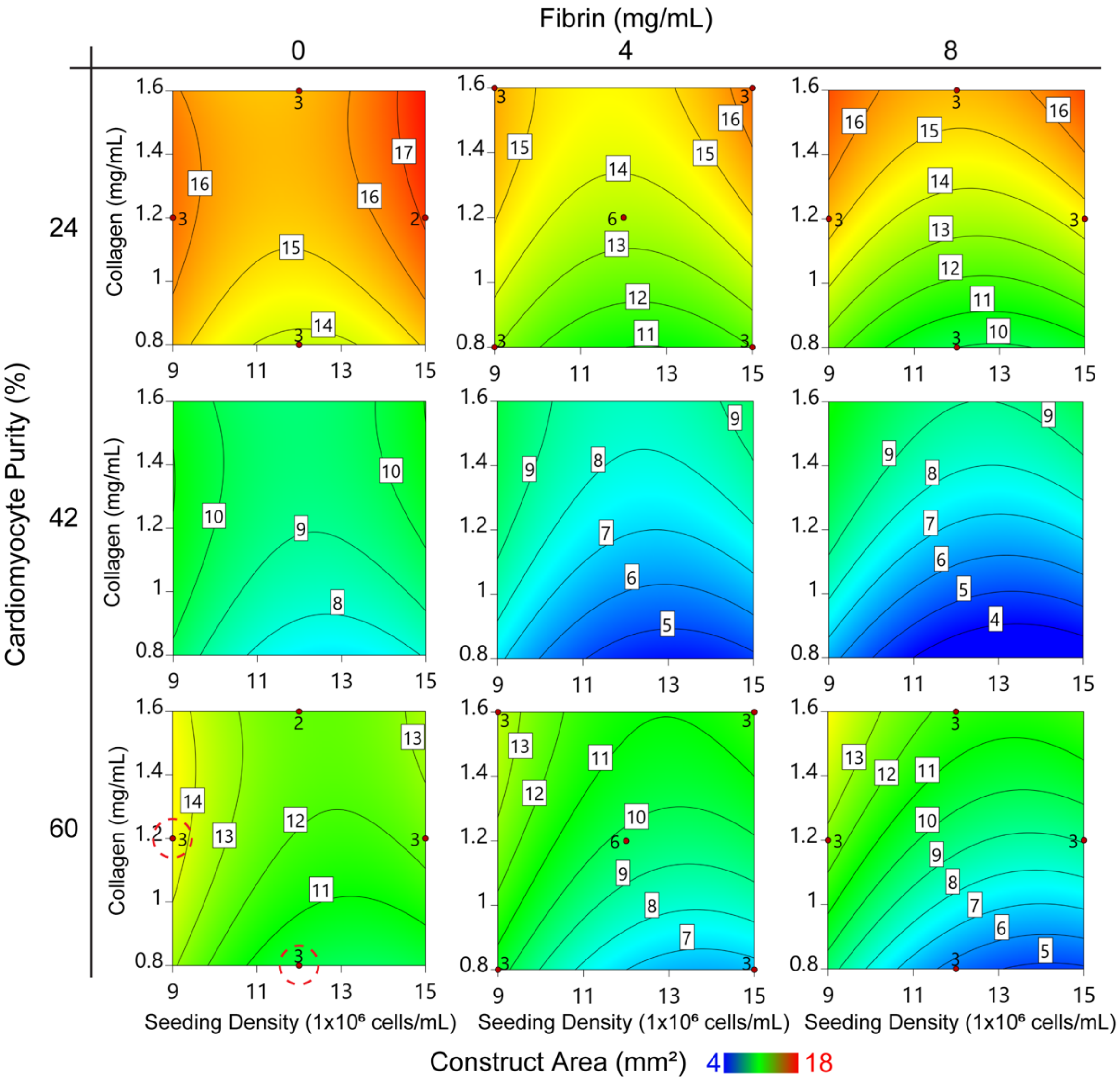

Figure 3. 4: **Contour plots describing predicted construct compaction after 72 hours of culture.** Data is organized by cardiac purity (major y-axis), fibrin concentration (major x-axis), collagen concentration (minor y-axes), and seeding density (minor x-axes) for unpurified cardiomyocytes. Contour labels and colors indicate the predicted construct two-dimensional area in mm^2 (white boxed labels) after 72 hours of culture. Red dots and adjacent numbers indicate the number of empirical data replicates for a corresponding factor set, in positions prescribed by the Box-Behnken design. Red dashed circles indicate contractile groups.

Figure 3.4 is a discrete representation of the continuous model generated from the data collected in this experiment. Each of the nine contour plots represents the model's prediction of visible construct area in mm^2 (a metric of compaction) for a given cardiac purity value (major y-axis) and fibrin concentration (major x-axis) after 72 hours in culture, at which point compaction had stabilized. Within each contour plot, construct area values specific to a given collagen concentration (minor y-axis) and seeding density (minor x-axis) can be found. Blue areas represent small visible construct areas, associated with high degrees of compaction, while red areas represent high visible construct areas, associated with low degrees of compaction. A complete numeric representation of this and all other presented models can be found in the Appendix 1.

Increased fibrin concentration and initial seeding density were both associated with increased construct compaction, while increased collagen concentration was associated with decreased compaction. Cardiac purity was the predominant factor influencing construct compaction and our data shows nuances not yet reported in cardiac tissue engineering. The least compaction was observed with the lowest cardiomyocyte purity (24.4%), suggesting that cardiomyocyte-ECM adhesions are crucial for hydrogel remodeling and tissue compaction. Interestingly, the highest cardiomyocyte purity (60.2%) was associated with moderate compaction that increased with increasing fibrin concentration to a minimum area of about 5 mm^2. The greatest compaction was predicted to occur with cardiomyocyte purities ranging from 40-50%, also demonstrating reduced area to a minimum of about 4 mm^2 with increasing fibrin concentration (Fig A1.4).

While these experiments identified construct formulations that consistently yielded high degrees of compaction, only two formulations produced uniformly beating constructs across all three of the trials (Fig 3.4) and therefore predictive models for functional mechanics such as contractility were not generated from these experiments. We hypothesized that disruption of the cardiac electrical syncytium was occurring due to the non-cardiomyocyte cell population in spite of high levels of compaction. Thus, we repeated this experiment a fourth time with lactate purified cardiomyocytes having 75.5% cTnT$^+$ cells (Fig 3.5 A).

5.3.3 Robust Compaction and Beating is Associated with Increased Stiffness and Force Production

Passive and active mechanical characteristics were quantified in constructs containing lactate purified cardiomyocytes where functional cardiac tissues emerged in 9 of 13 groups (Fig A1.3). In addition to compaction, predictive models were generated for Young's modulus and peak twitch force (Fig 3.5 B,C).

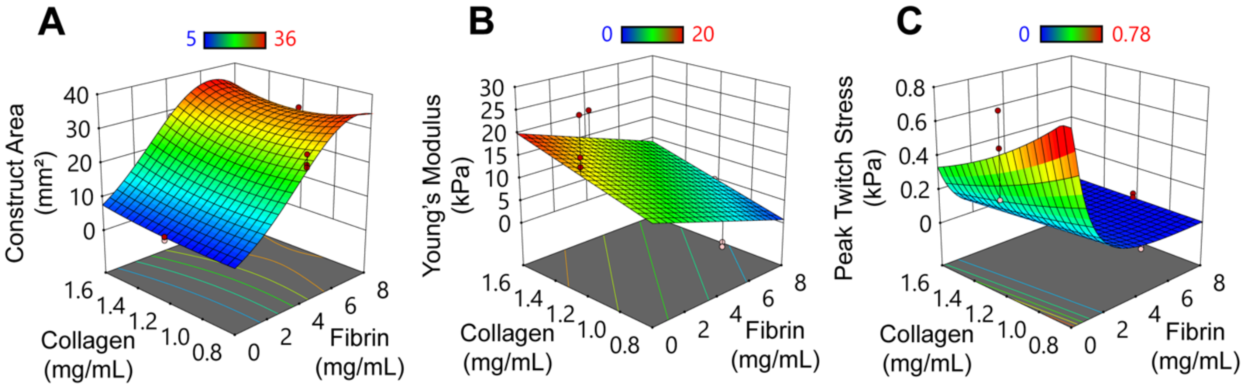

Figure 3. 5: Response surface plots for cardiac tissue constructs prepared from purified hiPSC-derived cardiomyocytes (15 x10^6 cells/mL) at day 6. (A) Visible construct area as measured via the medium-throughput compaction assay. See Fig A1.3 for an alternative representation of this data. (B) Tensile stiffness under a constant strain rate of 10% strain/min. (C) Force generation normalized by cross-sectional area at 1 Hz electrical stimulation. Red and pink dots represent data points above and below (respectively) those predicted by the model.

Surprisingly, although compaction was dominated by fibrin concentration, high concentrations of fibrin reduced compaction with lactate purified cardiomyocytes, which is the opposite effect of fibrin to that observed in unpurified cardiomyocyte constructs. While again increased seeding density was associated with increased compaction and increased collagen concentration was associated with decreased compaction, their effects were small (Fig A1.3, Table A1.9). Further, data using the lactate purified cardiomyocytes could not be incorporated into a single predictive model with data from the unpurified cardiomyocyte experiments due to a statistically significant lack of fit ($p<0.0001$). This result indicates that a quadratic or lower order model could not be found to describe the compaction response of both purified and unpurified cardiomyocytes, which we discuss below.

Predictive modeling for tensile Young's modulus of cardiac tissue constructs associates increased stiffness with increasing collagen concentration and cell number but decreased fibrin concentration. Tensile stiffness of this hydrogel engineered tissue system evaluated empirically approached values of native rat myocardium (15-30 kPa; Figs 3.2 D and A1.4) in the 0 mg/mL fibrin, 1.2 mg/mL collagen, and 15e6 cells/mL group, where Young's modulus was 21.79±3.23 kPa (Group 11; Table A1.1, Fig A1.5 D), approximated by the model as 16 kPa. Further, three other groups approached the lower limit of the physiological range of stiffness (Fig A1.5), suggesting an open landscape for mimicking the native myocardium stiffness.

Group	**Peak Active Stress (kPa)**	**Young's Modulus (kPa)**	**V_{up} (mN/mm^2/s)**	**T_{50} (ms)**	**T_{90} (ms)**
1	0.49±0.13	8.29±0.025	2.29±0.71	180±11.1	318±15.0
4	0.11±0.05	13.03±1.19	0.59±0.30	124±16.0	238±11.4
7	0.18±0.08	18.92±1.02	1.18±0.55	129±24.7	237±40.0
11	0.54±0.14*	21.79±3.26	2.94±0.68*	156±6.35	279±3.48*

Table 3. 3: Lactate purified twitch mechanics at 1 Hz for select groups. V_{up}, upstroke velocity; T_{50} and T_{90}, time to 50% and 90% relaxation, respectively. See Fig A1.6 for more information. n=3 for all groups. * indicates $p<0.05$ versus group 4.

Active twitch contractions at 1 Hz (equivalent to 60 beats per minute, a resting human heart rate) has a physiological positive force-length response 6 days after tissue formation (Fig A1.6). Predictive modeling for peak twitch stress (i.e. force normalized to cross-sectional area) associates high peak twitch forces with increased seeding densities and decreased fibrin concentrations (as with Young's modulus) but also with decreased collagen concentration (which is the opposite of the Young's modulus data and predictions; Fig. 3.5 B, C). The greatest peak twitch stress observed experimentally at 30% stretch beyond resting length is 0.54±0.14 kPa in constructs produced with 0 mg/mL fibrin, 1.2 mg/mL collagen, and 15e6 cells/mL (Group 11), which is the same group as peak stiffness. However, peak twitch stress as high as 0.84 kPa is predicted for constructs with lower (0.8 mg/mL) collagen concentration. Peak twitch stress varies between groups as much as 5-fold (Table 3) demonstrating that matrix composition alone greatly influences not just tissue remodeling (compaction) but also cellular functional phenotype. The contraction upstroke velocity, V_{up}, is faster with higher peak stress but similar between groups when V_{up} is normalized by peak stress, suggesting that crossbridge binding and force generation kinetics are not altered in the different tissue groups. The twitch duration , measured by the time (in ms) from peak stress to 50% and 90% relaxation (T_{50} and T_{90}, respectively) and controlled by calcium handling dynamics and thin filament de-activation, shows little change between groups, suggesting little to no dependence of twitch relaxation on force amplitude. This force data suggests that the ECM composition at tissue casting impacts the early (day 6) amplitude of force generation in engineered cardiac tissue with little impact on cardiomyocyte functional maturation.

5.3.4 Force Production follows Calcium Kinetics

In order to directly evaluate calcium transient kinetics in engineered cardiac tissues prepared using the conditions described, tissues were prepared with cardiomyocytes differentiated from an hiPSC line genetically engineered to express a calcium indicator, GCaMP6 (GCaMP-CMs). The conditions associated with groups 11 and 4 were chosen for further evaluation based on the significant differences observed in force production (Tables 3, S3). Additionally, a new group was added (referred to as Group "Predicted") based on the model’s prediction of conditions that would maximize force production (15e6 cells/mL in 0.8 mg/mL collagen only). All groups were cultured under the conditions previously described for 6 days and evaluated for cellular morphology (Fig 3.6 A-C) and function (Fig 3.6 D-F, Table A1.3). All groups formed syncytia and were visibly beating uniformly when evaluated on day 6. No differences are observed in alpha-actinin-positive cardiomyocyte content (cell number or size), alignment, and sarcomere length (data not shown). Connexin 43 shows no change in expression level or distribution of gap junctions (Fig 3.6 A-C, insets), suggesting that force amplitude was not primarily altered by cardiomyocyte or myofilament content, alignment, or electrical connectivity at this relatively early time point after tissue formation.

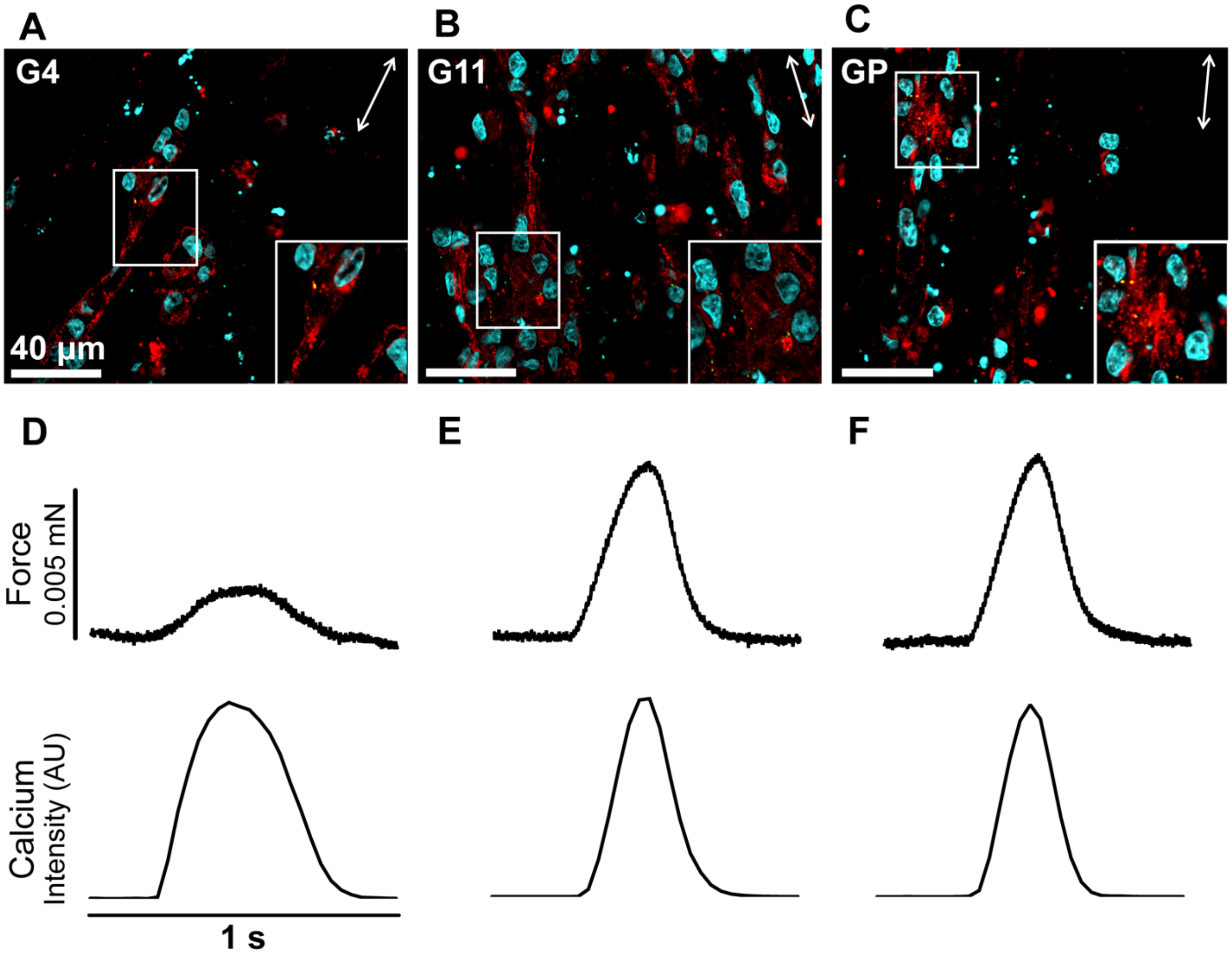

Figure 3. 6: Histological analysis and simultaneous force/calcium transient analysis of cardiac tissue constructs prepared from GCaMP-CMs at day 6. (A-C) Frozen sections of tissue constructs prepared under group 4 conditions (G4: 9e6 cells/mL in 1.2 mg/mL collagen only), group 11 conditions (G11: 15e6 cells/mL in 1.2 mg/mL collagen only) and the conditions predicted to lead to the highest force production by the model (GP: 15e6 cells/mL in 0.8 mg/mL collagen only). Immunofluorescence of tissue sections show α-actinin (red) labeled cardiomyocytes aligned with the tissue main axis (double-headed arrows), connexin 43 (green), and DAPI (cyan). Insets highlight striated cardiomyocytes and punctate connexin 43-positive gap junctions. (D-F) Force (top) and calcium transient (bottom) traces from representative contractions are generated from fluorescent video capture of GCaMP signal for each of the three groups (corresponding to A-C) at 15% strain and 1 Hz.

Active mechanical measurements are made with simultaneous fluorescent video collection to capture calcium transients from the GCaMP signal (Fig 3.6 D-F). As expected, faster upstroke velocity, V_{up}, is required to reach higher peak stress in group 11 (Tables 3.3, A1.3). However, significant differences in upstroke velocity of force disappear when V_{up} is normalized for stress amplitude (i.e. normalized by the number of crossbridges, since force is proportional to crossbridge number). These normalized force upstroke kinetics are similar to calcium kinetics (namely, calcium V_{up} is not significantly different between groups 4 and 11; Table A1.3). These data suggest no change in calcium release kinetics due to ECM conditions of engineered tissues; however, calcium amplitude was not measured and could explain force amplitude differences and no differences in twitch duration (T_{50}, T_{90}) suggest that calcium sequestration are not significantly impacted by ECM composition.

Within 72 hours of casting, all but one of the six replicates prepared for the Predicted group (GP) failed due to necking and breaking, suggesting that the mechanical properties of the compacted hydrogel are insufficient to withstand the cell-generated tissue tension[47]. The single surviving sample from the Predicted group produced the greatest peak contraction force, validating the model and supporting a critical role for collagen density in maintaining tissue integrity during early tissue formation. However, the model cannot account for an imbalance of cell tension and ECM strength during remodeling that causes breaking, so empirical evaluation must be completed.

5.4 Discussion

The study presented herein sought to understand the relationship between blended collagen and fibrin hydrogels and resident human iPSC-derived cardiomyocyte populations for the purpose of creating engineered cardiac tissues. Utilizing a response surface methodology to evaluate the impact and interactions of these factors, the results clearly demonstrate that scaffold protein composition and cell population both play critical roles in engineered cardiac tissue development, as measured by compaction, tissue stiffness, and active force production.

In the field of cardiac tissue engineering, the debate concerning what the optimal scaffold is ensues. How to define “optimum” will depend upon the desired outcome of the study, be it in vitro disease modeling or in vivo heart repair. Our study evaluated acellular and cellular constructs to assess how scaffold composition impacts stiffness (Young's modulus), hydrogel compaction, and contractile force generation using the two most common natural polymer matrices, namely type 1 collagen and fibrin. Knowing that the stiffness of the environment impacts cellular phenotype[9], acellular compressive and tensile mechanics (Figs 3.1-3.2) demonstrated that the concentrations of collagen and fibrin dominated the time-dependent stiffness response. In cellular constructs, we found that (1) purity of the input hiPSC-derived cardiomyocyte population drives the success of tissue formation into a uniformly beating cardiac tissue and (2) trade-offs must be made between maximizing tensile stiffness (to match values from native adult myocardium) and maximizing contraction force. The range of acellular blended collagen and fibrin hydrogel formulations considered in this study approximated the compressive stiffness of native rat myocardium, but deviated significantly ($P<0.0001$) from the tensile stiffness of native rat myocardial tissue in both long (30.80±2.71 kPa) and transverse (16.58±1.85 kPa) fiber orientations. However, tensile stiffness values of two groups of cellularized cardiac constructs (18.92±1.02 kPa and 21.79±3.26 kPa) approached the tensile stiffness values of native adult myocardium. Remodeling by resident cells and associated stresses resulting from isometric compaction (due to the custom-designed tissue molds[39,40]) increase scaffold protein density and provide alignment cues, which are both likely responsible for the increased tensile stiffness values in cellular constructs. It is important to note that the predictive model generated in this study associated increased initial collagen concentration with both increased tensile stiffness and decreased peak active twitch stress (Fig 3.5). Therefore, while high collagen concentrations yield constructs with passive mechanics that approximate those of native myocardium, lower collagen concentrations yield constructs with improved active contractile mechanics (Fig 3.2, 3.5). A potential explanation for this trade-off of stiffness versus contractile force amplitude is that the hiPSC-derived cardiomyocytes are relatively immature at the 6-day evaluation time point used in this study, having structure and contractility akin to fetal tissue[38,48,49], and thus function best in a stiffness environment that more closely matches that of the fetal heart (12±4 kPa)[50].

The experiment design employed in this study aimed to identify a role for fibrin in a blended hydrogel system that was driven by the hypothesis that the stiffness provided by fibrin would improve cellular remodeling, tissue stiffness, and contractility upon tissue formation and prior to cellular maturation. An important consideration for scaffold composition is that prior experiments in our lab and others[47] have demonstrated that sufficiently low scaffold protein concentrations and high seeding densities can lead to construct compaction to the point of extreme necking, breaking, and construct failure. Studies by other groups that use only fibrin as a scaffold material utilize an inhibitor of fibrinolysis (like aprotinin or aminocaproic acid) to inhibit fibrin degradation, presumably to enable tissue formation, prevent breaking, and allow sufficient time for cellular deposition of matrix[25,26]. Thus, while this study did not assess fibrin-only constructs, we show that compaction of blended hydrogel constructs is aided by fibrin in these experimental conditions (Fig 3.4), potentially due to its ease of degradation and remodeling by the resident cell population, which is useful in many tissue engineering applications. Aprotinin was chosen as a fibrinolytic inhibitor for this study due to its widespread use in the field of cardiac tissue engineering[32,51,52]. Aprotinin is known to inhibit several serine proteases including plasmin, trypsin, and chymotrypsin[53]. Conversely, other fibrinolytic inhibitors such as aminocaproic acid[54] and tranexamic acid[55] are believed to influence a narrower set of proteases, which may be suited for mechanistic study of fibrin remodeling in engineered tissues.

The iterative DOE approach is a powerful tool for assessing the influence of scaffold composition on tissue formation and function, and our results clearly show modulation of the engineered tissue by both scaffold properties and cell population, specifically cell purity and seeding density, though likely also cell type, cell line, and species. Therefore, for the purpose of optimizing construct formulation for generating compact contractile human cardiac tissue with iPSC-derived cardiomyocytes, our study demonstrates that a low collagen concentration (0.8 mg/mL) and high cardiomyocyte purity are required.

Using unpurified cardiomyocytes (25-60% cTnT-positive), increasing fibrin concentration and cell seeding density were found to increase tissue compaction, while increased collagen concentration was found to decrease compaction (Fig 3.4). This model predicts the greatest compaction occurs with a moderate cardiomyocyte purity (40 - 50%), however, this group did not correlate with uniform beating, which is visual evidence of a syncytium throughout the tissue. Only 60% pure cardiomyocytes with no fibrin demonstrated uniform beating in all 3 tissue samples (Fig 3.4, circled data points), suggesting a strong role for cardiac purity in predicting a functional cardiac tissue. This result may guide quality control parameters for cardiac tissue engineering. Importantly, the impact and influence of collagen and fibrin scaffold parameters on tissue formation, as measured by tissue compaction, changed as a result of higher cardiac purities, which was achieved through either efficient directed differentiation or with post-differentiation lactate-based metabolic purification. The inversion of fibrin's effect on tissue compaction, and the fact that constructs prepared with low versus high purity cardiomyocytes could not be described by a single response surface model, suggest that hiPSC-derived cardiomyocytes alone are effective in binding collagen and compacting the hydrogel to form functional cardiac tissue. The lactate purification protocol used in this study requires 11 days of treatment beyond the 14 – 15 day protocol required for cardiomyocyte differentiation. As a result, the population of lactate purified cells was substantially older than the unpurified cell groups (26 days vs. 14 – 18 days). However, these older cells performed well in collagen-only engineered tissues when purity was high, resulting in peak twitch forces of 0.54 ± 0.14 mN/mm^2 (Fig 3.5). Constructs prepared with high-purity, unpurified cardiomyocytes (84.6% cTnT$^+$) responded similarly to collagen hydrogel scaffolds with and without fibrin (Fig A1.7). How the age of cardiomyocytes entering tissues impacts tissue formation remains an open issue; a recent study by Vunjak-Novakovic and colleagues strongly supports using younger cardiomyocytes (10-12 days differentiation in 12 mg/mL fibrin hydrogel scaffold) to take advantage of their cellular plasticity as they adapt to the 3D environment and mature in the engineered tissue[51], but this approach compromises control over the input cell population and primarily it's purity. As we observed with high purity cardiomyocytes, contractility was greatly modulated by scaffold composition, emphasizing the importance of well-defined scaffold compositions in forming functional tissues with reproducibility.

Fully defined culture conditions (without serum or Matrigel) are used in this study to minimize unknown and variable protein constituents and are being adopted in a number of tissue engineering studies utilizing hiPSC-derived cells for future clinical applications. Indeed, the engineered cardiac tissues prepared in this study are cultured under defined conditions similar to those optimized by Zimmermann and colleagues.[56] In agreement with their study, which used fibroblast doping to modulate cardiomyocyte content of engineered tissues to be 40 – 75% cardiomyocytes, we show that peak construct compaction occurs with constructs composed of 40 – 50% cTnT$^+$ cardiomyocytes. We also show a consistently increased force amplitude with low collagen and no fibrin across batches of high purity cardiomyocytes (with and without lactate purification and from Gibco or GCaMP hiPSC lines), suggesting that low collagen is a critically important design parameter in the context of defined culture conditions that enables functional tissue formation despite variation in hiPSC-cardiomyocyte populations. Force generation kinetics followed the kinetics of the calcium transient, but were not different between groups when normalized by force amplitude, suggesting that differences in peak force were not due to alterations in calcium or force kinetics. Possible explanations for the differences in contractile force amplitude are the amplitude of the calcium release (not measured) or force transduction pathways through the cytoskeleton and ECM. Future work may elucidate these mechanisms and their relationship to "maturation" through longer culture periods, in addition to fibroblast supplementation and different biophysical culture conditions (e.g., Tiburcy et al. uses additional stretching of the tissue after compaction and stiff posts for maintenance or "maturation" culture). Here, we demonstrate that uniformly contracting tissues with good force generation are formed with an optimum, defined matrix composition by day 6, prior to maturation culture, while accounting for varying input cardiomyocyte populations.

The non-cardiomyocyte hiPSC-derived cell population is largely dismissed as a "fibroblast-like" cell type, but heterogeneous cell and matrix interactions do impact engineered tissue formation. Construct compaction peaked at approximately 45% purity for all fibrin concentrations, suggesting that neither hiPSC-derived cardiomyocytes nor the non-cardiac cells dominate the compaction response, but that cardiac tissue remodeling relies on a balance of heterogenous cell interactions. Cardiac fibroblasts are primarily responsible for matrix remodeling in native myocardial tissue[57,58] and show plasticity in their number and phenotype during aging and disease, such as post-myocardial infarction when they become "activated" to a more contractile and synthetic phenotype[59,60]. Although the non-cardiac population in these studies was 3.0 - 43.6% positive for alpha-smooth muscle actin (αSMA; a classic marker of activated, contractile fibroblasts[61,62]) they were not efficient at compacting matrix (as may be expected for fibroblasts) when they made up ~75% of the cell population, suggesting that they may also have an immature or poorly defined phenotype. It is clear that under these in vitro conditions, cardiomyocytes play a prominent role in tissue remodeling and that heterogeneous interactions with fibroblasts and scaffold composition modulate cardiomyocyte-driven compaction and contractility. While prior studies have suggested that human cardiomyocytes contribute to the process of matrix deposition and remodeling[63], this is the first study to our knowledge to demonstrate and quantify the network of interactions between cells and matrix components influencing the ability of hiPSC-derived cardiomyocytes to form and remodel engineered tissue.

5.5 Conclusions

Engineered cardiac tissue development is dictated by a complex relationship between scaffold composition, cell density, and cell purity. In collagen and fibrin hydrogel scaffolds seeded with unpurified hiPSC-derived cardiomyocytes, the greatest tissue compaction was predicted to occur with a relatively high concentration of fibrin (8 mg/mL), low concentration of collagen (0.8 mg/mL), high seeding density (15e6 cells/mL), and moderate cardiomyocyte purity (40-50%). However, beating tissues appeared only in pure collagen groups with higher cardiac purity (≥60%), and at 6 days after tissue formation peak contractile force was 0.54 ± 0.14 mN/mm^2 with 15 x 10^6 cardiomyocytes/mL in 1.2 mg/mL collagen. These results provide robust methods for creating highly functional human iPSC-derived cardiac tissues for many translational applications, and emphasize the importance of matching scaffold composition to cell population to form tissues with optimal efficiency and function.

5.6 Acknowledgements

We gratefully acknowledge funding from NIH R01 HL135091 and the GCaMP6 hiPSC line from Bruce Conklin (The Gladstone Institutes).

5.7 References

1. Discher, D. E., Janmey, P. & Wang, Y. Tissue Cells Feel and Respond to the Stiffness of Their Substrate. *Science* **310**, 1139–1143 (2005).
2. Gershlak, J. R. *et al.* Mesenchymal stem cells ability to generate traction stress in response to substrate stiffness is modulated by the changing extracellular matrix composition of the heart during development. *Biochem. Biophys. Res. Commun.* **439**, 161–166 (2013).
3. Curran, J. M., Chen, R. & Hunt, J. A. The guidance of human mesenchymal stem cell differentiation in vitro by controlled modifications to the cell substrate. *Biomaterials* **27**, 4783–4793 (2006).
4. Cheng, J., Jun, Y., Qin, J. & Lee, S.-H. Electrospinning versus microfluidic spinning of functional fibers for biomedical applications. *Biomaterials* **114**, 121–143 (2017).
5. Caves, J. M. *et al.* The use of microfiber composites of elastin-like protein matrix reinforced with synthetic collagen in the design of vascular grafts. *Biomaterials* **31**, (2010).
6. Sears, N. A., Dhavalikar, P. S., Seshadri, D. & Cosgriff-Hernandez, E. A Review of 3D Printing of Tissue Engineering Constructs. *Tissue Eng. Part B Rev.* (2016). doi:10.1089/ten.TEB.2015.0464
7. Hwang, P. T. *et al.* Poly(ε-caprolactone)/gelatin composite electrospun scaffolds with porous crater-like structures for tissue engineering. *J. Biomed. Mater. Res. A* n/a-n/a (2015). doi:10.1002/jbm.a.35614
8. Chhabra, P., Tyagi, P., Bhatnagar, A., Mittal, G. & Kumar, A. Optimization, characterization, and efficacy evaluation of 2% chitosan scaffold for tissue engineering and wound healing. *J. Pharm. Bioallied Sci.* **8**, 300–308 (2016).
9. Jacot, J. G., McCulloch, A. D. & Omens, J. H. Substrate Stiffness Affects the Functional Maturation of Neonatal Rat Ventricular Myocytes. *Biophys. J.* **95**, 3479–3487 (2008).
10. Lien, S.-M., Ko, L.-Y. & Huang, T.-J. Effect of pore size on ECM secretion and cell growth in gelatin scaffold for articular cartilage tissue engineering. *Acta Biomater.* **5**, 670–679 (2009).
11. Drury, J. L. & Mooney, D. J. Hydrogels for tissue engineering: scaffold design variables and applications. *Biomaterials* **24**, 4337–4351 (2003).
12. Guyot, Y. *et al.* A computational model for cell/ECM growth on 3D surfaces using the level set method: a bone tissue engineering case study. *Biomech. Model. Mechanobiol.* **13**, 1361–1371 (2014).
13. Tartarini, D. & Mele, E. Adult Stem Cell Therapies for Wound Healing: Biomaterials and Computational Models. *Front. Bioeng. Biotechnol.* **3**, (2016).
14. Jung, J. P., Hu, D., Domian, I. J. & Ogle, B. M. An integrated statistical model for enhanced murine cardiomyocyte differentiation via optimized engagement of 3D extracellular matrices. *Sci. Rep.* **5**, 18705 (2015).
15. Jung, J. P., Bache-Wiig, M. K., Provenzano, P. P. & Ogle, B. M. Heterogeneous Differentiation of Human Mesenchymal Stem Cells in 3D Extracellular Matrix Composites. *BioResearch Open Access* **5**, 37–48 (2016).
16. Lin, S. *et al.* Predictive modelling-based design and experiments for synthesis and spinning of bioinspired silk fibres. *Nat. Commun.* **6**, 6892 (2015).
17. Sonnaert, M. *et al.* Multifactorial Optimization of Contrast-Enhanced Nanofocus Computed Tomography for Quantitative Analysis of Neo-Tissue Formation in Tissue Engineering Constructs. *PLOS ONE* **10**, e0130227 (2015).
18. Eschenhagen, T. *et al.* 3D engineered heart tissue for replacement therapy. *Basic Res. Cardiol.* **97**, I146–I152 (2002).
19. Zimmermann, W.-H. *et al.* Engineered heart tissue grafts improve systolic and diastolic function in infarcted rat hearts. *Nat. Med.* **12**, 452–458 (2006).
20. Tulloch, N. L. *et al.* Growth of Engineered Human Myocardium with Mechanical Loading and Vascular Co-culture. *Circ. Res.* **109**, 47–59 (2011).
21. Tiburcy, M., Meyer, T., Soong, P. L. & Zimmermann, W.-H. Collagen-based engineered heart muscle. *Methods Mol. Biol. Clifton NJ* **1181**, 167–176 (2014).

22. Naito, H. *et al.* Optimizing Engineered Heart Tissue for Therapeutic Applications as Surrogate Heart Muscle. *Circulation* **114**, I-72-I–78 (2006).

23. Rupert, C. E. & Coulombe, K. L. K. IGF1 and NRG1 Enhance Proliferation, Metabolic Maturity, and the Force-Frequency Response in hESC-Derived Engineered Cardiac Tissues. *Stem Cells International* (2017). doi:10.1155/2017/7648409

24. Schaefer, J. & Tranquillo, R. T. Tissue Contraction Force Microscopy for Optimization of Engineered Cardiac Tissue. *Tissue Eng. Part C Methods* (2015). doi:10.1089/ten.TEC.2015.0220

25. Ye, K. Y., Sullivan, K. E. & Black, L. D. Encapsulation of Cardiomyocytes in a Fibrin Hydrogel for Cardiac Tissue Engineering. *J. Vis. Exp. JoVE* (2011). doi:10.3791/3251

26. Wendel, J. S., Ye, L., Zhang, P., Tranquillo, R. T. & Zhang, J. J. Functional Consequences of a Tissue-Engineered Myocardial Patch for Cardiac Repair in a Rat Infarct Model. *Tissue Eng. Part A* **20**, 1325–1335 (2014).

27. Radisic, M. *et al.* Functional assembly of engineered myocardium by electrical stimulation of cardiac myocytes cultured on scaffolds. *Proc. Natl. Acad. Sci. U. S. A.* **101**, 18129–18134 (2004).

28. Radisic, M. *et al.* High-density seeding of myocyte cells for cardiac tissue engineering. *Biotechnol. Bioeng.* **82**, 403–414 (2003).

29. Marsano, A. *et al.* The effect of controlled expression of VEGF by transduced myoblasts in a cardiac patch on vascularization in a mouse model of myocardial infarction. *Biomaterials* **34**, 393–401 (2013).

30. Dynamic quantitative visualization of single cell alignment and migration and matrix remodeling in 3-D collagen hydrogels under mechanical force. *Biomaterials* **32**, 3776–3783 (2011).

31. Jockenhoevel, S. *et al.* Fibrin gel – advantages of a new scaffold in cardiovascular tissue engineering. *Eur. J. Cardiothorac. Surg.* **19**, 424–430 (2001).

32. Coffin, S. T. & Gaudette, G. R. Aprotinin extends mechanical integrity time of cell seeded fibrin sutures1. *J. Biomed. Mater. Res. A* n/a-n/a (2016). doi:10.1002/jbm.a.35754

33. Ma, D. *et al.* Generation of patient-specific induced pluripotent stem cell-derived cardiomyocytes as a cellular model of arrhythmogenic right ventricular cardiomyopathy. *Eur. Heart J.* **34**, 1122–1133 (2013).

34. Zuppinger, C. 3D culture for cardiac cells. *Biochim. Biophys. Acta BBA - Mol. Cell Res.* **1863**, 1873–1881 (2016).

35. Feinberg, A. W. *et al.* Functional Differences in Engineered Myocardium from Embryonic Stem Cell-Derived versus Neonatal Cardiomyocytes. *Stem Cell Rep.* **1**, 387–396 (2013).

36. Bergmann, O. *et al.* Evidence for cardiomyocyte renewal in humans. *Science* **324**, 98–102 (2009).

37. Laflamme, M. A. *et al.* Formation of Human Myocardium in the Rat Heart from Human Embryonic Stem Cells. *Am. J. Pathol.* **167**, 663–671 (2005).

38. Robertson, C., Tran, D. D. & George, S. C. Concise Review: Maturation Phases of Human Pluripotent Stem Cell-Derived Cardiomyocytes. *Stem Cells Dayt. Ohio* **31**, (2013).

39. Munarin, F., Kaiser, N. J., Kim, T. Y., Choi, B.-R. & Coulombe, K. L. K. Laser-Etched Designs for Molding Hydrogel-Based Engineered Tissues. *Tissue Eng. Part C Methods* **23**, 311–321 (2017).

40. Kaiser, N. J., Munarin, F. & Coulombe, K. L. K. Custom Engineered Tissue Culture Molds from Laser-etched Masters. *JoVE J. Vis. Exp.* e57239–e57239 (2018). doi:10.3791/57239

41. Box, G. E. P., Hunter, J. S. & Hunter, W. G. *Statistics for experimenters: design, innovation, and discovery*. (Wiley-Interscience, 2005).

42. NIST/SEMATECH e-Handbook of Statistical Methods. (2013). Available at: http://www.itl.nist.gov/div898/handbook/index.htm. (Accessed: 22nd January 2018)

43. Bursac, N., Loo, Y., Leong, K. & Tung, L. Novel anisotropic engineered cardiac tissues: studies of electrical propagation. *Biochem. Biophys. Res. Commun.* **361**, 847–853 (2007).

44. Pierce, W. H. Body forces and pressures in elastic models of the myocardium. *Biophys. J.* **34**, 35–59 (1981).

45. Engelmayr, G. C. *et al.* Accordion-like honeycombs for tissue engineering of cardiac anisotropy. *Nat. Mater.* **7**, 1003–1010 (2008).

46. Bhana, B. *et al.* Influence of substrate stiffness on the phenotype of heart cells. *Biotechnol. Bioeng.* **105**, 1148–1160

47. Wang, H. *et al.* Necking and failure of constrained 3D microtissues induced by cellular tension. *Proc. Natl. Acad. Sci. U. S. A.* **110**, 20923–20928 (2013).

48. Batalov, I. & Feinberg, A. W. Differentiation of Cardiomyocytes from Human Pluripotent Stem Cells Using Monolayer Culture. *Biomark. Insights* **10**, 71–76 (2015).

49. Khan, J. M., Lyon, A. R. & Harding, S. E. The case for induced pluripotent stem cell-derived cardiomyocytes in pharmacological screening. *Br. J. Pharmacol.* **169**, 304–317 (2013).

50. Jacot, J. G., Martin, J. C. & Hunt, D. L. Mechanobiology of Cardiomyocyte Development. *J. Biomech.* **43**, 93 (2010).

51. Ronaldson-Bouchard, K. *et al.* Advanced maturation of human cardiac tissue grown from pluripotent stem cells. *Nature* **556**, 239–243 (2018).

52. Wang, Z., Lee, S. J., Cheng, H.-J., Yoo, J. J. & Atala, A. 3D bioprinted functional and contractile cardiac tissue constructs. *Acta Biomater.* **70**, 48–56 (2018).

53. Mahdy, A. M. & Webster, N. R. Perioperative systemic haemostatic agents. *Br. J. Anaesth.* **93**, 842–858 (2004).

54. Kupcsik, L., Alini, M. & Stoddart, M. J. Epsilon-Aminocaproic Acid Is a Useful Fibrin Degradation Inhibitor for Cartilage Tissue Engineering. *Tissue Eng. Part A* **15**, 2309–2313 (2008).

55. Cholewinski, E., Dietrich, M., Flanagan, T. C., Schmitz-Rode, T. & Jockenhoevel, S. Tranexamic Acid—An Alternative to Aprotinin in Fibrin-Based Cardiovascular Tissue Engineering. *Tissue Eng. Part A* **15**, 3645–3653 (2009).

56. Tiburcy, M. *et al.* Defined Engineered Human Myocardium With Advanced Maturation for Applications in Heart Failure Modeling and Repair. *Circulation* **135**, 1832–1847 (2017).

57. Camelliti, P., Borg, T. K. & Kohl, P. Structural and functional characterisation of cardiac fibroblasts. *Cardiovasc. Res.* **65**, 40–51 (2005).

58. Fan, D., Takawale, A., Lee, J. & Kassiri, Z. Cardiac fibroblasts, fibrosis and extracellular matrix remodeling in heart disease. *Fibrogenesis Tissue Repair* **5**, 15 (2012).

59. Fibroblasts in myocardial infarction: A role in inflammation and repair. *J. Mol. Cell. Cardiol.* **70**, 74–82 (2014).

60. Bujak, M. & Frangogiannis, N. G. The role of TGF-β signaling in myocardial infarction and cardiac remodeling. *Cardiovasc. Res.* **74**, 184–195 (2007).

61. Santiago, J.-J. *et al.* Cardiac fibroblast to myofibroblast differentiation in vivo and in vitro: Expression of focal adhesion components in neonatal and adult rat ventricular myofibroblasts. *Dev. Dyn.* **239**, 1573–1584 (2010).

62. Willems, I. E., Havenith, M. G., De Mey, J. G. & Daemen, M. J. The alpha-smooth muscle actin-positive cells in healing human myocardial scars. *Am. J. Pathol.* **145**, 868–875 (1994).

63. Kreutziger, K. L. *et al.* Developing Vasculature and Stroma in Engineered Human Myocardium. *Tissue Eng. Part A* **17**, 1219–1228 (2011).

CHAPTER 4: DIGITAL DESIGN AND AUTOMATED FABRICATION OF BESPOKE COLLAGEN MICROFIBER SCAFFOLDS

Reproduced with permission from Kaiser, N. J., Bellows, J. A., Kant, R. J. & Coulombe, K. L. K. Digital Design and Automated Fabrication of Bespoke Collagen Microfiber Scaffolds. *Tissue Eng Part C Methods* (In press).

6.1 Introduction

An expansive variety of natural and synthetic polymer hydrogel materials has been used in soft tissue engineering because of their versatility, permitting a high degree of customization for individual applications (reviewed in Jafari et. al., 2017[1]). Tissue engineers are able to select from a vast library of hydrogel scaffolds (defined by molecular composition and organization) and choose a composition best suited to the cell and tissue type of interest in terms of cell adhesion site availability and density, mechanical stiffness and strength, remodeling/degradation rate and cleavage sites, and many other parameters important for tissue development. However, these ubiquitous, homogenous hydrogel systems are limited in their ability to provide internal structural and organizational cues to resident cells. Stress fields resulting from tissue compaction in isometrically confined tissues are often used as a surrogate in order to induce cell alignment, which is also known to be a functional characteristic of many types of tissue (e.g. skeletal muscle, cardiac muscle, cartilage, and the vascular wall). While often effective at inducing alignment, these methods necessitate either tissue fenestrations (reducing the efficacy and efficiency of tissues with function related to mechanics and structure), or prescribe high-aspect-ratio tissues with limited utility as replacement tissue patches[2–5]. Further, this approach does not enable the design of the mechanical material anisotropy that is found in these native tissues and extracellular matrices (ECM, often a defining feature of these tissues and materials), which plays an important role in cell and tissue development[6,7].

In recent years a number of approaches to emulating ECM structural and mechanical cues in 3D engineered tissues have been used, including both aligned and random (unorganized) nanofiber mats[8–11], aligned pores through directional freezing[12–15], sphere- and rod-templated scaffolds[16,17], and 3D printed scaffolds[18–21] in a wide array of shapes. While all of these strategies successfully impact cell phenotype and function and thereby demonstrate their value to the field and the importance of mechanical and structural signaling cues, these methods all require compromise in terms of thickness limitations, ease of cell infiltration, and precise control over the scaffold pattern or morphology. Aligned and unorganized nanofiber mats feature high surface areas and fiber densities which are helpful for cell adhesion and interaction, but the high fiber density can make cell infiltration challenging, especially in thicker mats[22–24]. Recent innovations have allowed for the collection of aligned electrospun fiber arrays[25–27], but the fabrication of more complex, well-defined patterns remains a challenge. Directional freezing is used to create uniform, anisotropic pore arrays in a variety of natural and synthetic scaffold materials. The aligned pores improve cell infiltration and impart mechanical and structural anisotropy[15,28,29]. However, directional controlled rate freezing has constraints, such as singular freezing direction, that limit the types of morphologies that can be created. Finally, 3D printed scaffolds offer a high degree of reproducibility and a broad design space, but compromises must be made in terms of either resolution or scaffold polymer, often resulting in the exclusion of fully natural polymer scaffolds.

A bio-inspired alternative solution is to use polymer microfibers embedded in a bulk hydrogel, which presents a means of providing precise structural and mechanical cues to cells seeded in engineered tissues and provides tissue engineers another dimension of control in designing tissues for specific applications. Natural polymer fibers (such as collagen and fibrin) offer certain advantages due to their high number of cell adhesion sites, minimal immune response, and ability to be remodeled by resident and host cells. Aligned arrays of microfibers composed of collagen, fibrin, and other natural polymers have been used as scaffolds in a variety of tissue systems[9,30–32] as well as biomaterials with broader applications such as wound dressings and sutures[33,34]. Overlapping sets of natural polymer microfibers have also been used to create more sophisticated fibrous tissue scaffolds and therapeutic biomaterials with unique and tunable properties[35,36]. However, fabrication of natural polymer fibrous networks more complex than overlapping aligned fibers, as well as broader adoption of these scaffolds and biomaterials by other research labs, has been hindered by technical challenges related to the characteristic fragility of these natural polymers, leading to processes that require significant manual labor at bench scale. Without automation, fabrication has been restrained to simple patterns, low throughput, and low fiber density.

Herein, we present and characterize an automated method for the fabrication of high-fidelity, high density, 40 – 120 μm diameter collagen microfiber meshes. Through the use of software tools, mesh patterns are designed in a graphical user interface and translated into automated fabrication protocols (similar to those used by 3D printers), enabling the facile fabrication of complex designs. Further, we describe an aseptic method of capturing these meshes and embedding them in natural polymer hydrogels as acellular biomaterials or with cells as engineered tissues. The mechanical properties of single collagen microfibers and composite hydrogel-fiber scaffolds demonstrate ample strength and stiffness of the microfibers to impart material anisotropy in the composite scaffold. To ensure accessibility of our method, low-cost materials and off-the-shelf components were used as frequently as possible in the development of all associated tools and pieces of equipment, and all software tools and device plans are provided for download and use.

6.2 Materials and Methods

6.2.1 Isolation of rat tail tendon type I collagen

Rat tail tendons are a relatively high purity source of type I collagen, though other tissues could be used, such as bovine dermis. This method uses acid to extract full length telopeptide collagen.

a. Rat tails are collected from Sprague-Dawley rats within 30 minutes of sacrifice and are immediately frozen at -20°C for up to 6 months. Tails are thawed for 2 hours at room temperature and thoroughly washed with ethanol prior to tendon harvest.

b. Tendons are harvested using a "twist-and-pull" method described by Rajan et al, 2007[37]. Briefly, tails are grasped at both the cut end of the tail and at a second point approximately 2.5 cm further down the tail (towards the tip of the tail) using a pair of clean, sturdy hemostats or needle-nose pliers in each hand. While the pliers closer to the tip of the tail are held firmly in place, the second pair of pliers is rotated around the axis of the tail while grasping the 2.5 cm section, causing the tissue and cartilage to break away. After 2-3 rotations, the ~2.5 cm section can be pulled away and discarded, revealing the tail tendons. Exposed sections of tail tendons are cut with scissors into a beaker filled with ~250 mL of sterile phosphate buffered saline (PBS) to wash off tissue debris and keep tendons hydrated.

c. Washed tail tendons from approximately 12 tails are transferred to a 2 L beaker filled with 1.8 L of 0.1M acetic acid in DI water for collagen extraction. The beaker is stirred at 120 rpm at 4°C for 72 hours to solubilize the collagen.

d. Tissue debris is separated from the acid extracted collagen solution via centrifugation at 8,000 x g at 4°C for 2 hours. The supernatant containing the collagen is decanted into a beaker and the tissue debris pellets are discarded.

e. Collagen is precipitated from the acetic acid solution by the gradual addition of 5M NaCl in DI water while on a stir plate set to 200 rpm, until the collagen solution reaches a NaCl concentration of 4%. Stirring continues for 1 hour at 4°C, after which precipitated collagen is visible.

f. Precipitated collagen is isolated via centrifugation at 8,000 xg at 4°C for 2 hours. The supernatant is discarded and the pellets of collagen are re-dissolved in 0.1M acetic acid on a stir plate set to 120 rpm at 4°C over a period of 72 hours. Using a small volume of acetic acid (~75 mL for 12 rat tails) allows for the preparation of a high concentration stock solution. Additional 0.1M acetic acid can be added if necessary to fully dissolve the collagen.

g. Once dissolution of the collagen pellets is complete, a 5 mL aliquot of the collagen solution is lyophilized and weighed to determine the collagen concentration of the prepared solution (mass/volume). Additional 0.1M acetic acid is added to the remaining solubilized collagen to achieve a stock concentration of 13 mg/mL. Store collagen at 4°C for up to six months.

h. If desired, the collagen solution can be sterilized via chloroform vapor. Aliquot a volume of chloroform equal to 10% of the volume of collagen to be sterilized into the bottom of a conical tube or beaker. Carefully float the volume of collagen on top of the chloroform and store overnight at 4°C. The next day, collect the collagen solution, being careful not to take up any chloroform, and store at 4°C for up to 6 months.

6.2.2 Fabrication and assembly of collection device and bath

All acrylic to acrylic connections between parts are made by sanding with 150 grit sandpaper and then gluing with cyanoacrylate adhesive. See Figs A2.2, A2.4, and A2.6 for reference during assembly. Bolts and screws are referred to here by their thread size. Refer to Table A2.1 for further parts details.

a. Laser etch and cut all parts in the included laser design files (see Fig A2.1, A2.3, and A2.5 and supplemental files) out of ¼" thick acrylic. Target etching depths are described in each of these documents. Specific power, speed, and DPI settings will be laser dependent. A Universal Laser System PLS 6.75 equipped with a 75 watt laser cuts through ¼" acrylic cleanly with power, speed, and dots per inch (DPI) settings of 100% 1, 1000, etches to a depth of 2.00 mm with settings of 100%, 10, 1000, and etches to a depth of 3.00 mm with settings of 100%, 7, 1000.

b. Prepare required machined components (see Figs A2.7 and A2.8 for details). Using a local machine shop to match required specifications is recommended. Steel capture frames are best cut via industrial laser cutter followed by tapping the 1-72 threaded holes.

c. Assemble the fiber collector translator base by sanding the bottom edge of the translator stepper motor mount (Part D) and gluing into place on the translator base (Part A). Similarly sand and glue two stacked rail shaft risers (Part B) into the matching etched slots in the translator base, with M5 bolts in place to ensure screw holes are aligned. Press fit and glue the two ball bearings into the openings in the pulley mounts (Part C), sand the bottom of the mounts, and glue into place with the pulley rod inserted to ensure alignment. Install the NEMA-17 stepper motor with four M3 bolts through the motor mount. Install the four linear rail shaft guides with M5 bolts. Attach the 5 mm GT2 timing pulley to the shaft of the translation stepper and the 8 mm GT2 timing pulley to the pulley shaft. Insert each 8 mm rail through each of the linear bearing platforms as well as one pair of rail guides. Tighten the rail guide screws to fix the rods in place. Attach the linear bearing mounts (Part F) and the translator platform (Part E) to the linear bearing platforms with sixteen M4 screws. Prepare the timing belt grip (Part G) by cutting a 5 cm length of the GT2 timing belt and gluing into the etched trough, such that the teeth of the belt are exposed. Finally, install the translator timing belt by wrapping the remainder of the GT2 timing belt around the two translator timing pulleys, fixing the loose ends in place between the bottom of the translator platform (Part E) and the timing belt grip with four M4 bolts, cutting away excess.

d. Assemble the fiber collector rotator by stacking the inner mandrel support (Part J) between the two outer mandrel supports (Part I) such that the etched regions face each other. Fix in place with two M5 bolts before sanding the bottom and gluing into the matching slot on the rotator base (Part H). Press fit and glue the two ball bearings into the matching openings on the rotator stepper mount (Part K) and rotator shaft support (Part L). Install one Mcl and XL series timing pulley on the rotator stepper motor and attach to the rotator stepper mount with four M3 screws. Once the glue is dry, similarly sand the bottom and press fit these components into their matching slots on the rotator with the rotation drive shaft in place to ensure alignment. Install the other Mcl and XL series timing pulley on the rotation drive shaft and connect the two pulleys with the urethane timing belt.

e. Prepare one or more collection mandrels by press fitting the 37.5 cm long, 3/8” diameter polytetrafluoroethylene (PTFE) rods into the four large openings of each of the mandrel caps (Part N). Teflon rods can be cut to size with a razor blade. Slide the mandrel caps, number 008 o-rings, shaft collars, and the end ball bearing onto the mandrel rod. Tighten the set screws of the shaft collars to fix the mandrel caps and ball bearing in place, as shown in Fig A2.2, using the o-rings and shaft collars to hold the components in place.

f. Sand all four edges of the ethanol bath bottom (Part Q) as well connection regions of the sides (Part P) and front and back (Part O). After sanding, clamp the bath together and glue by distributing cyanoacrylate adhesive along all connections. Once dry, seal all internal connections with silicone sealant to make the bath liquid tight.

g. Prepare the fiber guide support (Part M) by drilling two small holes 1 mm apart into the bottom of the top opening, sized to fit metal rods bent to form a narrow channel (see Fig A2.2). Catheter IV needles (14 gauge, 2.1 mm OD) work well.

h. Finally, complete the fiber collector by attaching the fiber collector rotator to the translator with four M4 bolts through the precut holes. Attach the fiber guide by sanding the bottom and gluing into the matching etched slots. Mount a collection mandrel with the mandrel coupler and cotter pins. Position the bath at the end of the fiber collector. Decreasing the distance between the bath and the collection mandrel may reduce fiber breaks during mesh collection (see Fig 4.1). Adhesive feet can optionally be attached to the bottom of the fiber collector and ethanol bath.

6.2.3 Designing microfiber mesh protocols

a. Mesh patterns are designed using an open source flowchart software program called "Dia" (https://sourceforge.net/projects/dia-installer/), which allows for simple "click and drag" placement of lines in a graphical user interface. A provided Dia data file with mesh windows matching the dimensions of those on the collection mandrels facilitates mesh design in each of the four mesh windows (3.5 x 19 cm, Fig A2.2).

b. Mesh protocols designed in Dia are saved and exported as .dxf files (document exchange format). This format identifies the lines that compose the mesh design based on the x,y coordinates of their start and end points.

c. Mesh protocol .dxf files are translated into .ino Arduino format protocols using a custom Python script included with this publication. Multiple mesh designs can be translated into a single .ino file which can be individually chosen during mesh collection.

d. Translated .ino format protocols are uploaded to the Arduino microcontroller with Motor Shield and RGB LCD Shield (Adafruit Industries, New York, New York) via USB for mesh fabrication. The Arduino microcontroller and Motor Shield provide a simple means of manipulating the two stepper motors, while the RGB LCD Shield provides a user interface during mesh collection.

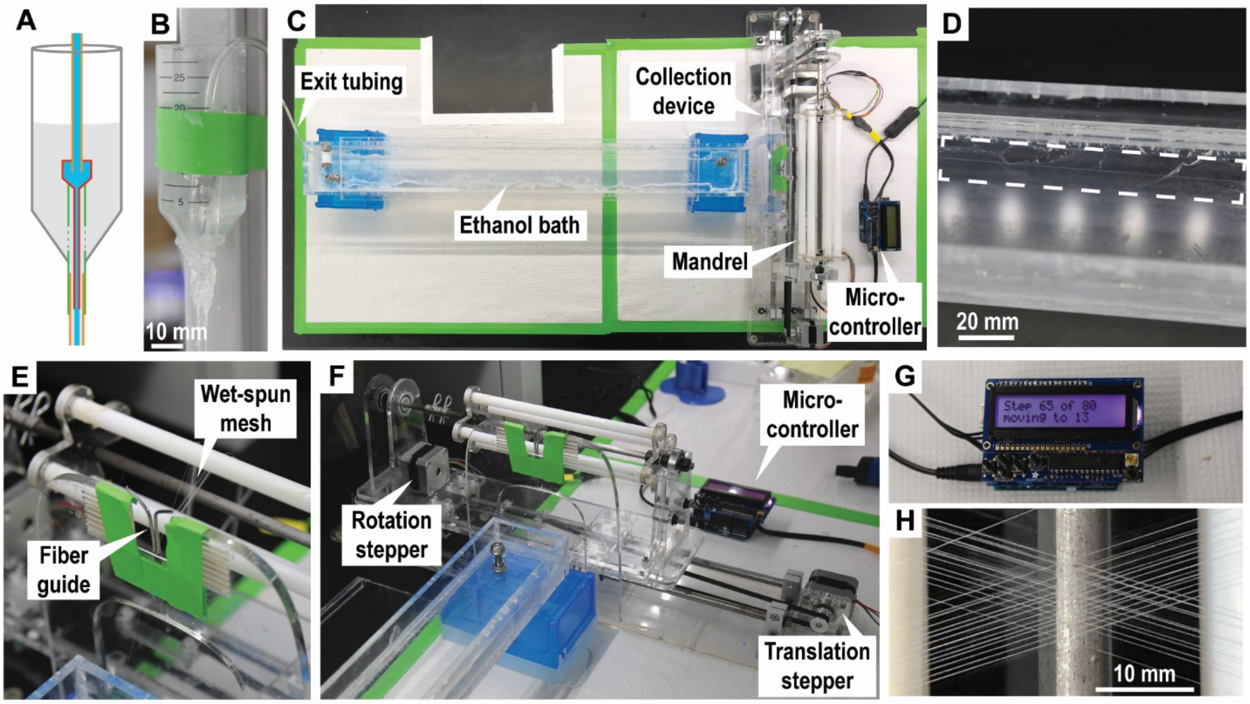

Figure 4. 1: Collagen fiber wet spinning and mesh organization. (A) A cross-sectional schematic of the spinneret composed of a 22 gauge syringe needle (red) inserted into the needle cap (green). (B) Collagen enters the spinneret via syringe pump extrusion and forms a co-axial flow system with wet spin buffer descending from the buffer reservoir. Windows have been cut in the needle cap to allow buffer to flow in from the sides, and the end of the cap has been cut in order to connect with the exit tubing (orange). (C) Overhead view of the bath and collector. The continuous collagen fiber exits into the bath filled with 70% ethanol, which washes away residual PEG and facilitates fiber drying. The fiber is pulled through the length of the bath, threaded through a fiber guide, and laid onto the mandrel of the collection device. (D) A close-up view of a continuous collagen fiber traveling through the 70% ethanol bath. The dotted line box indicates the location of the continuous collagen microfiber. (E) A close-up view of the fiber guide and the collection mandrel. The dotted line box indicates the location of the continuous collagen microfiber. (F) The fiber collector consists of a fiber guide and the mandrel on a translating platform. Two stepper motors, driven by an Arduino microcontroller, direct the rotation and translation of the mandrel. (G) The Arduino microcontroller controls the collection device and executes mesh protocols. (H) A 30° collagen microfiber mesh on the mandrel.

6.2.4 Wet spinning collagen meshes

Collagen is wet spun into continuous microfibers using methods adapted from Caves et. al, 2010[38].

a. Prior to the start of wet spinning, the outer surfaces of the four polytetrafluoroethylene (PTFE) rods on the collection mandrel are coated with Neoweld Contact Cement (Springfield Leather Company, Springfield, MO) and allowed to dry for 20 minutes. This adhesive remains tacky for days after drying, holding fibers in place as they are collected and maintaining mesh design fidelity.

b. Dissolved gases in the collagen solution may form bubbles that interrupt the continuous wet spun fiber. If this problem arises, the collagen solution can be degassed in a vacuum chamber for 30 minutes prior to wet spinning.

c. The 64 x 7 cm bath (Fig 4.1 C) is filled with 650 mL of 70% ethanol, such that the depth in the bath is approximately 1.5 cm, allowing the fiber and tubing to remain submerged during collection.

d. The buffer reservoir of the spinneret (Fig 4.1 A, B) is filled with high viscosity wet spinning buffer (HV-WSB, 34.5 mM potassium phosphate monobasic, 85.2 mM sodium phosphate dibasic, 135 mM sodium chloride, 29.9 mM HEPES buffer, 8.57 mM polyethylene glycol (PEG) MW 35,000). Buffer flow into the 1 m length of 1.6 mm inner diameter (ID) polyvinyl chloride (PVC) tubing is initiated by applying suction to the end of the tubing with a micropipette.

e. Once HV-WSB begins exiting the length of PVC tubing, 13 mg/mL collagen I in 0.1 M acetic acid (see section 2.1) is extruded via syringe pump at a rate of 50 µL/min through a 0.4 mm ID spinneret prepared from a 22 gauge syringe needle into the same length of 1.6 mm ID PVC tubing, forming a coaxial flow system (Fig 4.1 B). Collagen precipitates from the 13 mg/mL solution as it travels the length of the tubing.

f. The continuous collagen fiber exits into the 70% ethanol bath, which washes away residual buffer solution and aids in drying the fiber.

g. The collagen fiber is picked up with forceps, dragged through the length of the bath, and a length of ~20 cm is held in the air for ~30 seconds, or until the fiber is dry. The dry fiber is then threaded through the fiber guide (Fig 4.1 E) and onto the collection mandrel rods.

h. The collection protocol is initiated on the Arduino microcontroller (Fig 4.1 G). As the mandrel rotates, the fiber is pulled through the fiber guide and onto the mandrel in the prescribed pattern. Drying time between mandrel rotations is an important parameter that can be modified in the digital collection protocol.

i. Once the mesh protocol is complete, the mandrel is removed from the collection device for mesh capture.

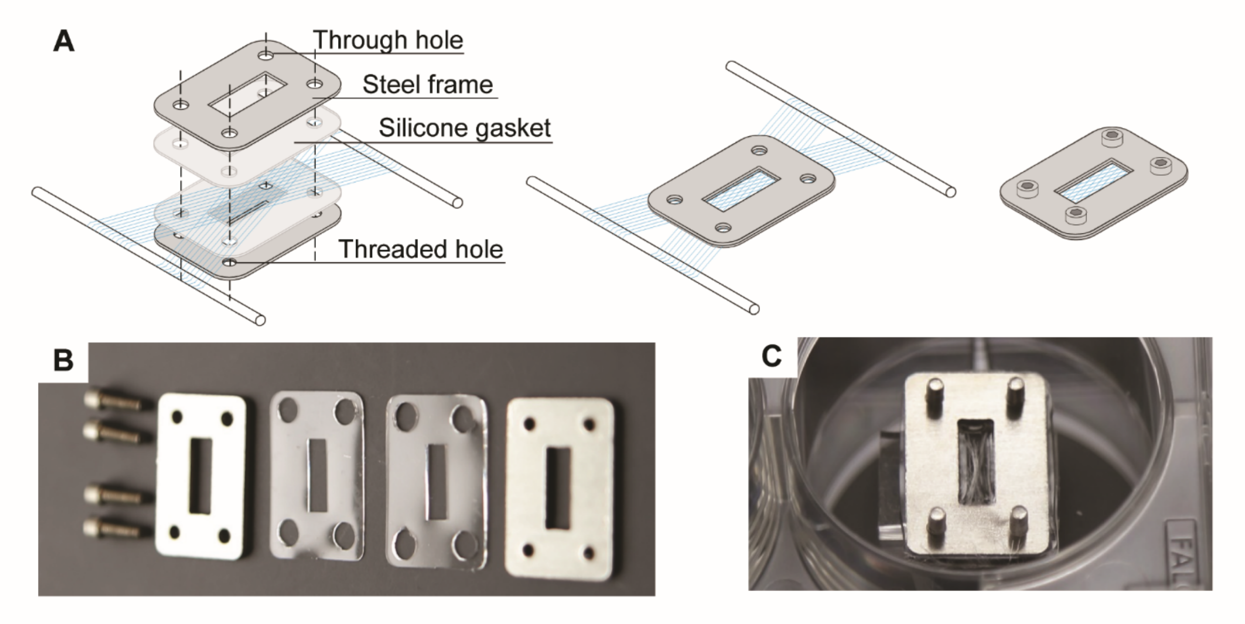

Figure 4. 2: Collagen mesh capture frames and method. (A) Silicone gaskets and steel support frames are placed on opposite sides of a collagen microfiber mesh on the collection mandrel, the frames are collapsed together, and screws are put in place to hold the frame together. (B) Screws, frames, and gaskets used in the capture process. (C) A captured mesh in the well of a 6 well plate and ready for hydrogel/cell casting.

6.2.5 Capturing and embedding wet spun collagen meshes

Mesh capture frames are stainless steel rectangular frames with a window matching the desired size of the composite tissue construct (in this case, 3 x 9 mm). Paired with gaskets of similar dimensions, the frames hold the fibers in place during capture, embedding/casting, and cell culture.

a. Prior to mesh capture, 316 stainless steel frames, matching polydimethylsiloxane (PDMS) gaskets, 316 stainless steel screws (McMaster-Carr), and a matching hex key are autoclaved. Half of the stainless steel frames feature 1-72 threaded holes, while the other half feature larger 1.98 mm diameter through holes, allowing the frames to be screwed together with ¼" long 1-72 threaded screws.

b. The frame alignment jig is thoroughly sprayed with ethanol and is placed inside a biosafety cabinet along with the autoclaved tools. The frame alignment jig is composed of an upper half and a lower half (prepared from laser cut ¼" thick acrylic plastic) connected by a metal hinge (HIGHPOINT Model 161694W). PDMS plugs sized to fit the windows of the capture frames hold the frames in place during capture. The upper half of the jig features four through holes so that screws can be put in place while the frame is closed.

c. Aseptically, the stainless steel capture frames are loaded onto the press-fit PDMS plugs of the alignment jig with a frame with threaded holes on the lower half of the jig, and frame with through holes on the upper half of the jig.

d. The alignment jig is carefully positioned on either side of a mesh on the collection mandrel, with the region of interest aligned with the window of the lower capture frame. Once positioned appropriately, the jig is closed and held in place by the alignment jig magnets.

e. Screws are inserted through the holes in the alignment jig, and are screwed into place in the frame with the help of the hex key. Once all four screws are place, the alignment jig can be opened and the captured mesh can be removed. Store captured meshes in a sterile vessel for up to two weeks prior to use.

f. Immediately prior to casting, while wearing sterile gloves, PDMS plugs are inserted into one capture frame of each frame set. The plugs should be sized to press-fit into the stainless steel windows. The frames are placed in an untreated six-well plate such that the plugs make contact with the bottom of the plate and keep the frames and bolts suspended.

g. A collagen hydrogel casting mix is pipetted through the open window in the stainless steel frame, using the tip of the pipette to guide the solution into the corners and edges of the window. In the case of acellular constructs, 2.0 mg/mL collagen I in PBS (pH 7.4) was used due to the poor handling properties of lower concentrations of collagen when uncompacted by resident cells. For cellularized constructs, 1.2 mg/mL collagen I in cell media is most effective[39].

h. Once casting is complete, the 6-well plate is placed in a 37°C incubator for 30 minutes or until the collagen hydrogel has become opaque. Sufficient PBS (or cell media for cellularized constructs) is then added to each well to ensure that the fibrous constructs are covered.

6.2.6 Calibration of the collection device

Fabricated mesh fidelity relative to the Dia design file is dependent on the distance between rod positions indicated in the Dia design file. Device calibration is necessary to ensure that the fiber angles described in the mesh protocol design step match what is produced during wet spinning and mesh fabrication. The Dia files provided with this manuscript (as supplemental files) have been calibrated to a rod spacing of 1240 units (corresponding to the y-axis tick marks in the Dia software; Fig 4.5 F) which is appropriate for the collection device as described here. Changes to the mandrel dimensions, fiber guide position, or choice of stepper motor will require adjusting or re-calibration of this parameter. The following steps describe the calibration process.

a. Using the provided Dia file (which uses a rod spacing parameter of 1240 units), a mesh is created with known target fiber angle in terms of units. The provided 30° mesh angle protocol is a good starting point.

b. The known mesh protocol is loaded onto the microcontroller and a set of meshes is fabricated, as described previously.

c. Each mesh on the mandrel is imaged on a microscope with a low power objective.

d. Fiber angle is analyzed via ImageJ using the Angle Tool (Fig 4.5 E). The angles of at least five overlapping fibers are measured for each mesh, and an overall empirical fiber angle mean is calculated.

e. A new calibration factor is determined by multiplying the ratio of the target fiber angle over the empirical fiber angle by the rod spacing parameter (initially 1240). The rod spacing parameter should increase if the empirical angle is too acute and decrease if the empirical angle is too obtuse.

f. Repeat steps b through d to ensure that the fiber angle is accurate.

6.2.7 Mechanical Analysis of Individual Collagen Fibers

a. An adhesive is prepared by thoroughly mixing two parts acetone and one part polyurethane adhesive (Gorilla Glue). Thinning the polyurethane in this way decreases the viscosity such that the glue can be precisely placed via syringe. The prepared adhesive is loaded into a 3 mL syringe.

b. The chamfered tip of a 22 gauge syringe is cut, such that the new opening of the needle is fully perpendicular to the length of the needle, and this needle is attached to the syringe. This step facilitates precise adhesive placement.

c. A printed grid of known dimensions (rectangles 14 mm x 8 mm) is glued to a petri dish. Stainless steel washers (ID 1.7 mm, OD 4.0 mm, McMaster-Carr) are carefully placed at each grid intersection to ensure sample regularity. Precise fiber length is measured later, immediately prior to testing via calipers.

d. Single wet spun collagen fibers are cut to approximate size and each is laid across a pair of the steel washers. An anti-static tool (such as the Milty Zerostat, or an ionizing air blower) may assist in dissipating stating electricity that can interfere with collagen fiber manipulation.

e. Under a dissection scope, the prepared syringe is used to deposit droplets of adhesive on the regions of fiber and washer overlap. The adhesive is allowed to dry overnight (Fig 4.3 B).

f. Once the adhesive is dry, fiber samples are placed in separate wells of a six well plate, covered with 4 mL of PBS, and incubated at 37°C for various lengths of time prior to testing.

g. Fiber samples are carefully removed from the six well plate and are placed into the PBS-filled bath of a micromechanical testing apparatus (Aurora Scientific, model 801C; Fig 4.3 A, C), consisting of a temperature controlled basin (maintained at 37°C), a hook connected to a lever arm, and a hook connected to a 5 mN load cell (Aurora Scientific, model 403a). One washer is placed around each of the two hooks, a preload of 0.1 mN is applied to each sample, and the initial sample length is measured with calipers.

h. Each fiber sample is preconditioned prior to testing by a triangular waveform pulling to 10% strain at a rate of 1% strain per second and declining at the same rate for a total of eight cycles.

i. After preconditioning, the 0.1 mN pre-load is re-applied, the new sample length is recorded, and each sample is pulled to break at a rate of 10% strain/min. Strain at break, ultimate tensile stress (UTS), and Young's modulus (defined based on the linear region of the stress-strain curve, typically between 10% and 30% strain) is calculated from the pull-to-break trace for each sample.

6.2.8 Mechanical Analysis of Fibrous Collagen Mesh Composites

a. Acellular collagen mesh composites are prepared using 30° and 60° fiber meshes with 200 µm fiber spacing in stainless steel capture frames as described (see *Capturing and embedding collagen meshes)*. Meshes are captured in two orthogonal orientations (referred to as longitudinal and transverse, see Fig 4.6A).

b. Mesh composites are incubated at 37°C in PBS for 6 days.

c. Mesh composites are isolated by disassembling the stainless steel capture frames. Aluminum T-clips (0.02 mm thick aluminum foil cut into the shape of a T, with a 0.8 mm diameter hole in the center of the longest tab) are attached to either end of the mesh composites by folding the wings inward (see Fig 4.6 B). This method provides a means of griping the hydrogel constructs without causing damage.

d. Samples are mounted on to a micromechanical apparatus (model 801C, Aurora Scientific) with a 37°C bath filled with PBS by positioning the two right angle hooks through the holes of the aluminum t-clips (see Fig 4.3 A). A preload of 0.1 mN is applied to each sample, and the initial samples length is measured with calipers.

e. Each composite sample is preconditioned prior to testing by a triangular waveform pulling to 10% strain at a rate of 1% strain per second and declining at the same rate for a total of eight cycles.

f. After preconditioning, the 0.1 mN pre-load is re-applied, the new sample length is recorded, and each sample is pulled to break at a rate of 10% strain/min. Young's modulus (defined based on the linear region of the stress-strain curve, typically between 10% and 30% strain) is calculated from the pull-to-break trace for each sample.

6.2.9 Statistical Analysis

All statistical analyses were performed in Prism 7 (GraphPad Inc., San Diego, CA). For comparison between two groups, Student's t-tests were used. For comparisons of more than two groups, one way analysis of variance (ANOVA) with multiple comparisons and Tukey's post-hoc test was used. Error bars represent standard error of the mean (SEM) unless otherwise noted. Group differences were considered statistically significant for p-values < 0.05.

6.3 Results

Single fiber tensile mechanical properties increase with physiological incubation or crosslinking

In order to manipulate the mechanical properties of a composite material with embedded collagen microfibers, the mechanical properties of the fibers relative to the bulk hydrogel material are of critical importance. Additionally, we hypothesized that collagen self-assembly would increase the stiffness and strength of the fibers in a physiological, aqueous microenvironment. Individual collagen microfibers were prepared using a mesh protocol with straight fibers spaced 400 μm apart. After spinning, fibers were cut from the mandrel and glued to stainless steel washers, as described previously in methods. Samples were incubated for 0, 24, 48, 72, or 96 hours in PBS at 37°C. All samples were preconditioned and then tested in a constant strain rate pull-to-break test as described previously. It is important to note that the 0 hour incubation group was allowed to hydrate in the testing bath for 10 minutes prior to analysis.

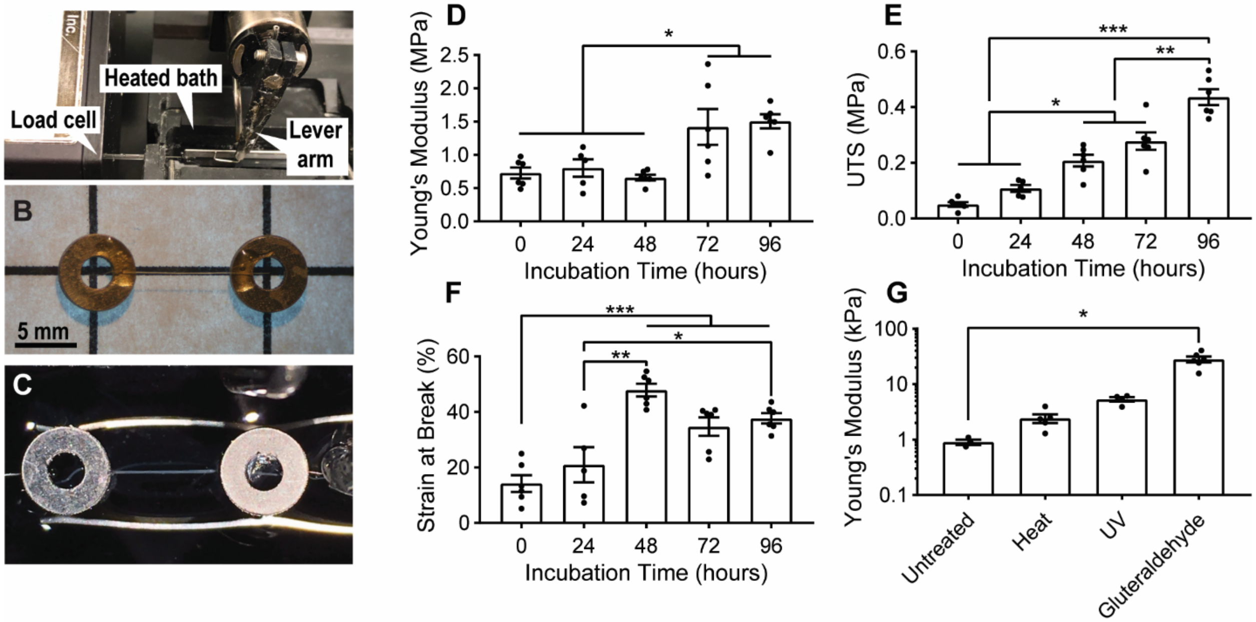

Figure 4. 3: Mechanical analysis of wet spun collagen microfibers. (A) Micromechanics setup consisting of one hook connected to a 5 mN load cell and one hook connected to a lever arm. (B) Individual collagen microfibers are glued to stainless steel washers prior to incubation in PBS at 37°C. (C) Hydrated collagen fiber sample mounted on the mechanics setup prior to analysis. (D, E, F) Young's modulus, ultimate tensile stress (UTS), and strain at break for individual collagen microfibers incubated for 0 to 96 hours. (G) Young's modulus of individual collagen microfibers crosslinked via heat (1 h), UV (1 h), or glutaraldehyde vapor (24 h) prior to incubation. * indicates $p<0.05$, ** indicates $p<0.001$, and *** indicates $p<0.0001$.

Prior to incubation treatment, hydrated collagen microfibers had a Young's modulus of 0.73±0.08 MPa, UTS of 0.05±0.01 MPa, and strain at break of 14.21±3.02% (Fig 4.3 D-F). After incubation for 96 hours, Young's modulus increased to 1.51±0.11 MPa, UTS to 0.44±0.03 MPa, and strain at break to 37.70±1.85%, significant increases for all three metrics ($p<0.05$). Evaluation at time points up to 15 days showed no further significant increases vs. 96 hrs (data not shown). To explore the range of stiffness values that could be achieved by these fibers through established cross-linking methods, individual fiber mechanical samples were crosslinked either via dry heat for 1 hour, 254 nm, 30 Watt UV light bulb (12 Watt output) at a distance of 75 cm for 1 hour, or exposure to 25% w/v glutaraldehyde vapor for 24 hours. Crosslinked fibers produced Young's modulus values as high as 28.1±3.5 MPa (Fig 4.3 G).

6.3.1 SEM and TEM imaging show collagen fibril self-assembly

To test our hypothesis that collagen self-assembly increases mechanical properties with incubation in physiological solution, we prepared bundles of overlapping wet spun collagen microfibers using a collection protocol without any translational movement. Bundles of 20 fibers were collected and embedded in agarose to hold fibers together during incubation and processing. One group of collagen fiber bundles was immediately stained with 3% potassium ferrocyanide, 2% osmium tetroxide and 1% uranyl acetate, embedded in EPON 812 resin, and sectioned for imaging, while a second group was incubated in a 10 cm dish filled with 10 mL of PBS at 37°C for 6 days before undergoing the same staining, blocking, and sectioning process. Both samples were imaged via serial block face (SBF) imaging, a technique that allows for layer-by-layer SEM imaging in order to develop a 3D visualization of the sample volume on a Thermo Apreo VS SEM.

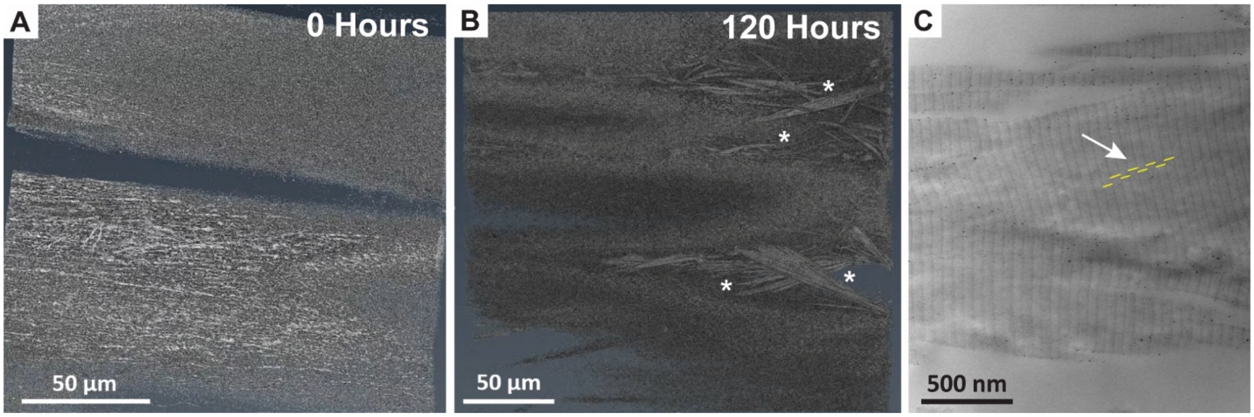

Figure 4. 4: Electron microscopy imaging of un-incubated and incubated collagen microfibers. (A) SBF volume reconstructed from serial SEM images of unincubated collagen microfibers and (B) collagen microfibers incubated for 120 hours under cell culture conditions. Note the emergence of large diameter fibrils (*) following collagen microfiber incubation. (C) TEM imaging of incubated collagen microfibers shows D-banding phenomena characteristic of collagen microfibers. Arrow indicates D-banding measurements.

SBF imaging of unincubated fibers revealed only small-diameter collagen fibrils visible along the exterior of the wet spun microfibers, while SBF renderings of the incubated fibers showed large, hierarchically organized collagen fibers (bundles ranging in diameter from 1 to 15 um) branching out from the surface of the wet spun microfibers, primarily oriented in the direction of the microfibers. Further TEM imaging of the incubated fibers (Fig 4.4 C) found additional evidence of collagen self-assembly in clear D-banding phenomena with periodicity of 61.0±2.8 nm, in line with values found in native collagen by other groups[40,41].

6.3.2 DSC analysis confirms collagen integrity after wet spinning

To confirm that the collagen maintained its native structure following the wet spinning process, we replicated the DSC methods of Zeugolis et. al., 2008[42]. Briefly, collagen microfibers were collected following the protocol described above and then both these microfibers as well as unprocessed, lyophilized stock collagen were incubated in PBS for 24 hours at 4°C to ensure full hydration. Samples were blotted dry on lint-free wipes and hermetically sealed in 40 µL aluminum pans. For each of the two groups, n=3 samples were sequentially heated at a constant rate of 5°C/min from 15°C to 90°C on a TA Instruments DSC Q20. An empty aluminum pan was used as a reference. The denaturation curve of each sample was analyzed based on three metrics: onset of denaturation temperature, peak denaturation temperature, and change in enthalpy (calculated as the area under the denaturation curve).

Sample	**ΔH_D (J/g)**	**Onset (°C)**	**Peak (°C)**
Lyophilized Collagen	-7.05±0.42	39.31±0.68	49.01±0.29
Collagen Microfibers	-5.95±0.14	41.97±0.06	51.88±0.26

Table 4. 1: DSC analysis of unprocessed collagen and collagen microfibers.

Both the collagen microfibers and the collagen stock solution exhibited change in enthalpy and denaturation temperatures consistent with native collagen molecular structure. Importantly, these values are distinctly greater than those associated with collagen denatured via aggressive solvents and gelatin (ΔH_D >-2.11, onset < 37.07, peak < 40.36)[42], suggesting that no denaturation occurred during wet spinning. Indeed, the collagen wet spinning process is associated with an increase in onset and peak denaturation temperatures, as has been observed previously with extruded collagen fibers, suggesting increased molecular interactions between the triple-helical collagen molecules within wet-spun fibers.

6.3.3 Mesh fidelity is dependent on fiber spacing

In order to evaluate the limits of fiber placement resolution, mesh protocols were prepared to deposit single, parallel fibers with spacing of 100, 200, or 400 µm. Both effective fiber spacing and fiber diameter were analyzed on the wet spinning mandrel (fiber diameter was considered because of the tendency of fibers to adhere to each other due to the accumulation of static electricity).

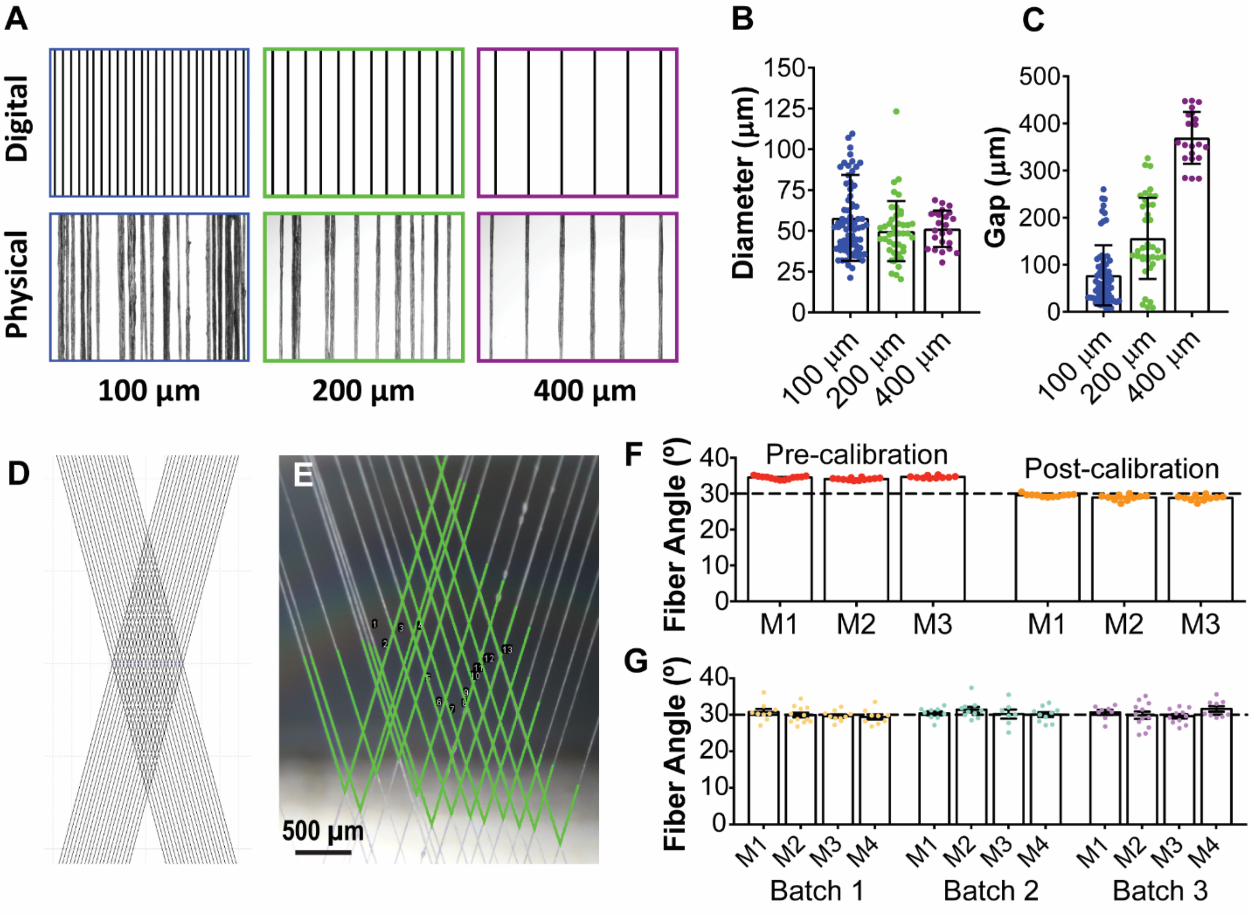

Figure 4. 5: Evaluation of wet spun mesh fidelity. (A) Digital design renderings for parallel fiber meshes with 100, 200, and 400 µm fiber spacing (top) and light microscopy images of physical meshes prepared using these protocols (bottom). (B) Quantitative analysis of parallel fiber fidelity based on diameter and (C) gap measurements of the 100, 200, and 400 µm spaced parallel fiber meshes via image analysis software. Error bars represent standard deviation (SD). (D) Digital design rendering of a 30°, 200 µm fiber spacing mesh. (E) Gross image of wet spun 30°, 200 µm fiber spacing mesh with image analysis fiber angle overlay. (F) Mesh angles produced from the 30°, 200 µm fiber spacing protocol before and after software calibration. (G) Mesh angles produced in each of four meshes from three separate fabrication batches using the 30°, 200 µm fiber spacing protocol.

Results showed that at 100 µm and 200 µm spacing static adhesion occurred, increasing the variability in both gap spacing and effective fiber diameter (Fig 4.5 A, B). Neighboring fiber adhesion was completely eliminated with 400 µm spacing, but lower spacing values may still be desirable in order to achieve higher fiber densities. Effective fiber diameter remained relatively consistent across the 100 µm, 200 µm, and 400 µm protocols, but variability decreased when adhesion was eliminated (57.89±3.09 µm, 49.79±2.81 µm, and 51.26±2.28 µm, respectively). Accuracy and precision of overlapping fiber angle was evaluated. Angled fiber placement is the result of a number of rotation steps on the stepper motor responsible for translational movement, and therefore placement accuracy is primarily dependent on calibration of the software (see methods). Conversely, calibration has no impact on placement precision, and this value is instead dependent on the inherent variability of the collection system and its constituent components, such as the precision of the stepper motor, flexion in the Teflon and acrylic components, and unevenness in the mandrel adhesive surface. Initial fiber angle data collected in the process of calibration (with the target of a 30° fiber angle) found a mean fiber angle of 34.4±0.1 degrees when angles between overlapping fibers were measured via ImageJ. Following calibration, a mean fiber angle of 29.1±0.1 was achieved (Fig 4.5 E). It should be noted that once properly calibrated, the collection system is able to produce meshes with any fiber angle with the same degree of accuracy and precision. Repeated mesh fabrication of the same 30° fiber angle and 200 µm fiber spacing protocol demonstrated a high degree of consistency across fabrication batches (Fig 4.5 F).

6.3.4 Mechanical testing of whole meshes demonstrates composite material anisotropy

To evaluate the impact of simple anisotropic collagen fiber patterns on mechanical anisotropy, collagen microfiber meshes with 30° and 60° fiber angles were prepared as described. Meshes were then captured in each of two orientations (diamond long axis parallel to either the long axis of the mesh window or the short axis of the mesh window, Fig 4.6 A). These meshes were embedded in 50 µL of a 2.0 mg/mL collagen solution, covered with PBS, and stored in culture conditions (37°C, 5% CO_2). After 6 days, constructs were harvested and aluminum t-clips were attached to each end of the construct to facilitate mechanical testing. All samples were evaluated under the same conditions as the single collagen fibers, described previously.

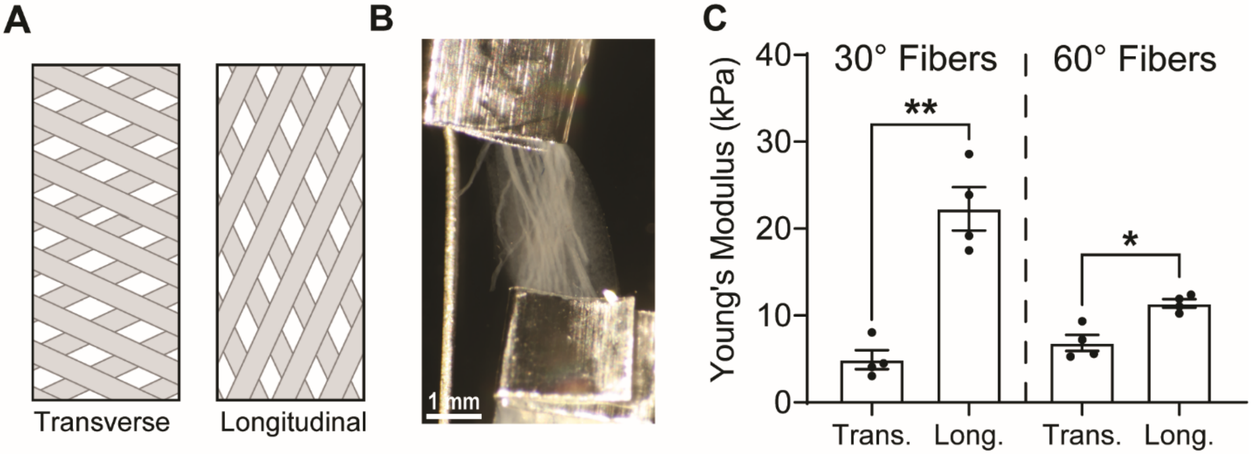

Figure 4. 6: Bidirectional mechanical analysis. (A) Diagram of 30° fiber angle mesh captured in transverse (left) and longitudinal (right) orientations. (B) Gross image of a longitudinal 30° fiber angle mesh during mechanical testing. (C) Young's modulus values for 30° and 60° fiber angle meshes evaluated in both transverse and longitudinal directions. * indicates $p<0.05$, ** indicates $p<0.001$.

Transverse composite fiber samples with a 30° fiber angle have a Young's modulus of 4.92±1.09 kPa while longitudinal samples have a Young's modulus of 22.28±2.50 kPa, representing a statistically significant 4.5-fold change ($p=0.0007$). Transverse fibers samples with a 60° fiber angle have a Young's modulus of 6.85±0.93 kPa while longitudinal samples have a Young's modulus of 11.40±0.48 kPa, representing a statistically significant 1.7-fold change ($p=0.0048$).

6.3.5 Fibrous scaffold composite tissues support resident cell viability

Collagen microfiber constructs were prepared with 50 μL of a casting mix of hiPSC-derived cardiomyocytes (15e6/mL) in 1.2 mg/mL collagen I. Constructs were cultured at 37°C, 5% CO_2 and were fed with cardiomyocyte maintenance media (RPMI+B27+Pen-Strep) every other day. After 6 days of culture constructs were incubated with calcein AM and ethidium homodimer-1 (Live/Dead Assay, Invitrogen) and imaged on a confocal microscope (Olympus FV3000). Replicate constructs were fixed, embedded in frozen blocks, sectioned, and stained with α-actinin, a cardiac marker, and DAPI nuclear stain.

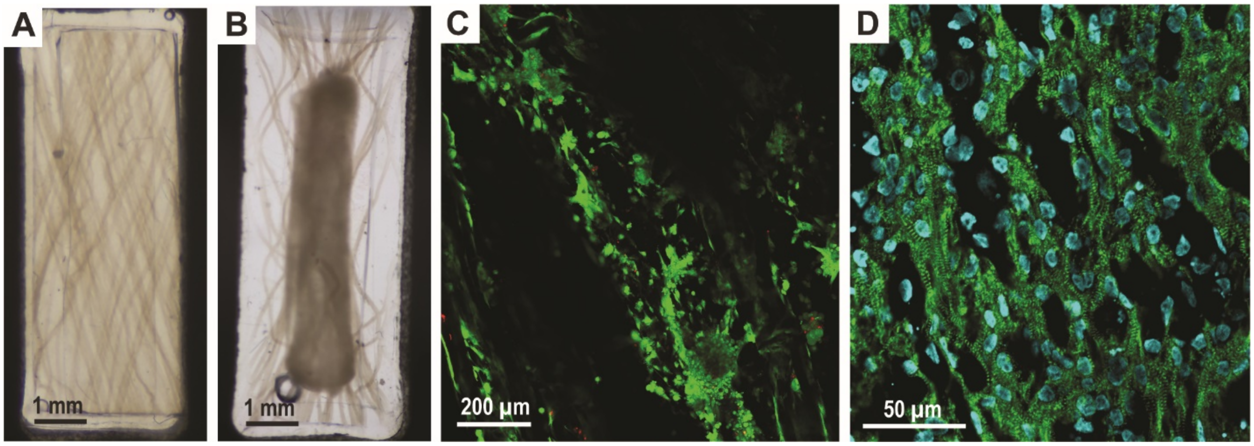

Figure 4. 7: Cells compact the collagen microfiber scaffold to form viable engineered tissue. (A) Uncompacted 30° fiber angle construct immediately after casting. (B) Compacted 30° fiber construct after 6 days in cell culture conditions. (C) Confocal image of live/dead stained collagen microfiber construct after 6 days of culture. Green calcein AM denotes the cytoplasm of live cells while red ethidium homodimer-1 denotes the nuclei of sparse dead cells. (D) Frozen block section of 30° fiber construct after 6 days in cell culture conditions stained with α-actinin (green), a cardiac marker, and DAPI (blue).

Gross images of constructs after 96 hours of culture demonstrate visible construct compaction, the process through which resident cells remodel the hydrogel microenvironment. Constructs compacted to 38.4±2.77% of their initial visible area after 96 hours of culture (n=6) with no failure to compact and form a tissue. Fluorescent live/dead staining revealed dense, viable cardiomyocytes throughout the tissue (Fig 4.7 C). Immunohistochemistry confirmed the cardiomyocyte phenotype of seeded cells in the form of banded α-actinin staining of myofibril z-discs (Fig 4.7 D).

6.4 Discussion

Over the past decade, the critical role of a fibrous ECM microenvironment in cell and tissue function has increased interest in the development of more sophisticated scaffold materials that can better emulate the diverse properties of native, fibrous ECM. Herein, we describe a highly versatile platform for producing scaffolds, tissues, and biomaterials composed of collagen microfibers embedded in a bulk hydrogel material, with bespoke collagen architectures and mechanical properties. By using only tools fabricated at relatively low cost and open source software, we have designed this platform to be accessible to as many researchers as possible because we believe that the applications in tissue engineering and biomaterials research are vast. As we show in this study, embedded collagen microfibers offer a flexible platform for this research due to the availability and relatively low cost of isolation from source tissues, in addition to the high density of cell adhesion sites, robust mechanics, and native molecular structure.

Evaluation of the stability or degradation of a new biomaterial in physiological conditions is critical to understanding material performance in biomedical applications. Importantly, individual collagen microfibers showed more robust mechanical performance with significantly increased Young's modulus, UTS, and strain at failure with increasing incubation time in physiological PBS at 37°C up to 4 days (Fig 4.3 D-F). After 96 hours of incubation the Young's modulus of the non-crosslinked fibers increased to 1.51±0.11 MPa, orders of magnitude greater than both conventional collagen hydrogels used for tissue engineering (0.5-12 kPa[39,43]) as well as most native soft tissues[44–47]. In addition, tensile strain at failure after 96 hours of incubation (37.70±1.85) exceeds the tensile strain regularly experienced by many native soft tissues (including cardiac muscle[48] and tendon[49]). Together these properties provide a mechanical justification for the utility of collagen microfibers as a reinforcing material in a composite soft tissue scaffold.

We hypothesized that molecular self-assembly of collagen could increase mechanical performance and evaluated this hypothesis via electron microscopy. SEM imaging of un-incubated and 5-day incubated collagen microfibers confirmed larger collagen fibrils after incubation, particularly at the surface of the collagen microfibers (Fig 4.4 B). Further TEM imaging confirmed fibril self-assembly with characteristic collagen D-banding at 61.0±2.8 nm periodicity, which agrees with values reported in the literature for native collagen[40,50]. DSC evaluation of hydrated collagen microfibers demonstrated denaturation characteristics consistent with those described in the literature for triple helical collagen. Together, these findings demonstrate that the molecular integrity of the purified collagen has been maintained throughout the isolation and wet spinning process. While previous groups have reported similar findings regarding wet spun collagen microfibers, the modifications to previously described protocols mandated by the mesh collection and embedding strategy described herein prescribed this validation[38,51]. Importantly, the molecular self-assembly that occurs within the collagen microfibers also demonstrates that 1) strength can be increased without chemical crosslinking and 2) the scaffold is composed of molecular building blocks that can be utilized and remodeled by cells in tissues.

Implementation of a composite fiber scaffold for regenerative medicine and tissue engineering requires evaluation of the mesh itself, the composite acellular material, and cell viability upon contact with the biomaterial. Mesh fidelity analyses demonstrate a high degree of both accuracy and precision in fiber angle, and minimal variability in fiber angle between fabrication batches (Fig. 4.4). Mesh fidelity was reduced in meshes with fibers spaced less than 400 μm apart due to static attractions between the fibers during placement, causing fibers to adhere to a neighboring fiber. However, this level of pattern corruption may be acceptable depending on the application. For example, closer fiber spacing may be desirable for applications in tissue scaffolds. Scaffolds composed of fibers ~400 μm apart would ensure that no cell in the fiber plane is more than 200 μm from a fiber with a high degree of homogeneity. Conversely, targeting 200 μm spacing with the approach described herein would ensure that a majority of cells are within 100 μm of a fiber (shown to increase cellular alignment[35]) at the cost of overall mesh uniformity. The impact (positive or negative) of this heterogeneity will depend largely on the intended application and associated tolerances.

With 400 µm spacing effective dry fiber diameters were fairly consistent (51.26±11.16 µm, mean±SD), but this variability also increased when spacing became small due to electrostatic interactions that drew adjacent fibers together (81.85±80.38 for 100 µm, mean±SD). It should be noted that similar collagen wet spinning methods have been used to produce collagen fibers with dry diameters ranging from 20 to 150 µm[38], but the fiber diameter presented here is associated with the wet spinning conditions that were found to minimize fiber breaks during mesh fabrication.

One major advantage of a bespoke fiber architecture is the ability to design anisotropy into the ECM scaffold, such as is found in cardiac muscle, for example. Mechanical analysis performed on acellular 30° meshes captured in both longitudinal and transverse orientations demonstrated the presence of mechanical anisotropy in composite constructs evidenced by a ~4.5:1 ratio between Young's modulus in the longitudinal orientation relative to the transverse orientation, while 60° meshes exhibited a ratio of ~1.7:1 (Fig 4.5). Young's modulus of the 30° composites in the longitudinal direction (22.28±2.50) approached that of native myocardium (30.80±2.71 kPa[39]), demonstrating that this fabrication method can produce composite materials that approach the passive stiffness of native tissues, prior to compaction by resident cells, which is anticipated to further increase the mechanical properties. Perhaps more importantly, the ratio of longitudinal to transverse Young's modulus values for the 60° composites was found to be 1.7:1, which closely approximates the range of anisotropic ratios reported in the literature for left ventricular native myocardium (~1.4:1 to ~2.0:1)[39,52,53].

Beyond the simple scaffold patterns that were evaluated in this study for the purpose of characterizing the capabilities and limitations of this platform, many other, sophisticated designs can be created for a range of applications (Fig A2.9). Arrays of aligned collagen microfibers can be created to emulate native tendon, and non-rectangular shapes can be created to emulate the both structure and mechanics diverse tissues, such as valve leaflets. Finally, we have prepared meshes with up to four layers (Fig A2.9), resulting in a hydrated mesh thickness of ~400 µm, permitting the fabrication of organized, dense fibrous tissues that approach/exceed the diffusion limits for engineered tissues[54–56]. Additional layers or modular assembly may enable thicker tissues if integrated with perfusion of nutrients *in vitro* or a blood supply via vasculature *in vivo*.

Fibrous collagen composite scaffolds are viable tissue scaffolds as we demonstrate with the culture of hiPSC-derived cardiomyocytes on meshes prepared in both parallel and 30° fiber configurations (Fig 4.6). Resident cells rapidly remodeled the bulk hydrogel and exerted stress on the collagen microfibers as shown by their deformation (Fig 4.6A, B). Fluorescent live/dead staining of cellularized constructs showed a high density of viable cardiomyocytes and few dead cells throughout the tissue (Fig 4.6 C), and immunohistochemistry confirmed that the resident cardiomyocytes maintained a striated morphology (Fig 4.6 D).

In spite of the wide variety of scaffold technologies available to tissue engineers today, a compromise must often be made between the desirable cell adhesion and remodeling responses of natural polymers (like triple helical collagen), and the ease of production, mechanical robustness, and molecular durability of synthetic polymers which have rapidly advanced novel fabrication technologies like 3D printing and electrospinning. In many cases the solution takes the form of natural and synthetic copolymers and blends, such as polycaprolactone (PCL)-collagen, collagen/polylactic acid (PLA), and collagen/poly(lactic-co-glyocolic acid)(PLGA)[57–60] in order to benefit from the mechanical integrity of synthetics and the cell-binding sites of collagen. The distinct advantages of incorporating wet spun collagen microfibers into scaffolds presented herein are that it offers precise, customizable structural control and physiologically relevant mechanical robustness without any compromise in terms of cell adhesion site density, remodeling response, and immune response by simply using unadulterated collagen in both a structurally-reinforcing fiber compartment and a bulk hydrogel. These benefits are amplified by the low barrier to entry required for the automated approach provided here.

Automated fabrication systems with high accuracy and precision offer substantial benefits over manual fabrication and assembly methods for both research and therapeutic applications. Even at the bench scale, improvements to reproducibility and time costs are extremely valuable. However, the typically high cost and complexity of automated fabrication for tissue engineering has limited the reach of these technologies in research settings. The simple method of mesh design and automated fabrication presented herein extends the advantages of automated biomaterial fabrication to a wide variety of applications and to users with any level of expertise to increase adoption of the collagen wet-spinning method. Unlike electrospinning methods[61,62], collagen wet spinning is minimally affected by environmental parameters (such as temperature, humidity, and airflow) and therefore can be performed much more cheaply and easily on an open benchtop. Alternatively, minimal modification would be required to adapt the process and device described herein for mesh fabrication in a biosafety cabinet in order to eliminate bioburden concerns. Indeed, the versatile methods described herein may serve as a strong platform for direct application in both tissue engineering and biomaterial research, and also to support further innovation in automated fabrication of customizable collagen materials.

6.5 Conclusions

Collagen microfiber meshes are a desirable platform for tissue engineering and biomaterials research due to the ability to tune both the mechanical properties of individual fibers as well as the composite as a whole with a material – collagen type 1 – that has inherently excellent cell adhesion and remodeling properties. In order to facilitate the use of this technology, we have successfully created a system for preparing composite collagen microfiber scaffolds and biomaterials with a broad range of mechanical properties and applications. By employing low cost, rapid fabrication techniques and accessible software tools, our system serves as a customizable, automated, biomaterial fabrication platform with equally broad accessibility. Adoption of bespoke collagen microfiber scaffolds will benefit biomaterials engineering and fulfill a need for fully natural fibrous materials with defined architecture.

6.6 Acknowledgements

Funding is gratefully acknowledged from Brown University School of Engineering.

6.7 Author Disclosure Statement

No competing financial interests exist.

6.8 References

1. Jafari, M. *et al.* Polymeric scaffolds in tissue engineering: a literature review. *J. Biomed. Mater. Res. B Appl. Biomater.* **105**, 431–459 (2017).
2. Bian, W., Jackman, C. P. & Bursac, N. Controlling the structural and functional anisotropy of engineered cardiac tissues. *Biofabrication* **6**, 024109 (2014).
3. Munarin, F., Kaiser, N. J., Kim, T. Y., Choi, B.-R. & Coulombe, K. L. K. Laser-Etched Designs for Molding Hydrogel-Based Engineered Tissues. *Tissue Eng. Part C Methods* **23**, 311–321 (2017).
4. Engelmayr, G. C. *et al.* Accordion-like honeycombs for tissue engineering of cardiac anisotropy. *Nat. Mater.* **7**, 1003–1010 (2008).
5. Zimmermann, W.-H. *et al.* Engineered heart tissue grafts improve systolic and diastolic function in infarcted rat hearts. *Nat. Med.* **12**, 452–458 (2006).
6. Sugimura, K. & Ishihara, S. The mechanical anisotropy in a tissue promotes ordering in hexagonal cell packing. *Dev. Camb. Engl.* **140**, 4091–4101 (2013).
7. Place, E. S., Evans, N. D. & Stevens, M. M. Complexity in biomaterials for tissue engineering. *Nat. Mater.* **8**, 457–470 (2009).
8. Jeffries, E. M., Allen, R. A., Gao, J., Pesce, M. & Wang, Y. Highly elastic and suturable electrospun poly(glycerol sebacate) fibrous scaffolds. *Acta Biomater.* doi:10.1016/j.actbio.2015.02.005
9. Hwang, P. T. *et al.* Poly(ε-caprolactone)/gelatin composite electrospun scaffolds with porous crater-like structures for tissue engineering. *J. Biomed. Mater. Res. A* n/a-n/a (2015). doi:10.1002/jbm.a.35614

10. Xu, W., Shen, R., Yan, Y. & Gao, J. Preparation and characterization of electrospun alginate/PLA nanofibers as tissue engineering material by emulsion eletrospinning. *J. Mech. Behav. Biomed. Mater.* **65**, 428–438 (2017).

11. Park, K., Ju, Y. M., Son, J. S., Ahn, K.-D. & Han, D. K. Surface modification of biodegradable electrospun nanofiber scaffolds and their interaction with fibroblasts. *J. Biomater. Sci. Polym. Ed.* **18**, 369–382 (2007).

12. Wu, X. *et al.* Preparation of aligned porous gelatin scaffolds by unidirectional freeze-drying method. *Acta Biomater.* **6**, 1167–1177 (2010).

13. Zhang, H. & Cooper, A. I. Aligned Porous Structures by Directional Freezing. *Adv. Mater.* **19**, 1529–1533 (2007).

14. Deville, S. Freeze-Casting of Porous Biomaterials: Structure, Properties and Opportunities. *Materials* **3**, 1913–1927 (2010).

15. Zhang, H. *et al.* Aligned two- and three-dimensional structures by directional freezing of polymers and nanoparticles. *Nat. Mater.* **4**, 787–793 (2005).

16. Madden, L. R. *et al.* Proangiogenic scaffolds as functional templates for cardiac tissue engineering. *Proc. Natl. Acad. Sci.* **107**, 15211–15216 (2010).

17. Bhrany, A. D., Irvin, C. A., Fujitani, K., Liu, Z. & Ratner, B. D. Evaluation of a sphere-templated polymeric scaffold as a subcutaneous implant. *JAMA Facial Plast. Surg.* **15**, 29–33 (2013).

18. Chia, H. N. & Wu, B. M. Recent advances in 3D printing of biomaterials. *J. Biol. Eng.* **9**, 4 (2015).

19. Derakhshanfar, S. *et al.* 3D bioprinting for biomedical devices and tissue engineering: A review of recent trends and advances. *Bioact. Mater.* **3**, 144–156 (2018).

20. Mosadegh, B., Xiong, G., Dunham, S. & Min, J. K. Current progress in 3D printing for cardiovascular tissue engineering. *Biomed. Mater.* **10**, 034002 (2015).

21. Jung, J. P., Bhuiyan, D. B. & Ogle, B. M. Solid organ fabrication: comparison of decellularization to 3D bioprinting. *Biomater. Res.* **20**, 27 (2016).

22. Khorshidi, S. *et al.* A review of key challenges of electrospun scaffolds for tissue-engineering applications. *J. Tissue Eng. Regen. Med.* **10**, 715–738 (2016).

23. Jiang, J. *et al.* Expanded 3D Nanofiber Scaffolds: Cell Penetration, Neovascularization, and Host Response. *Adv. Healthc. Mater.* **5**, 2993–3003 (2016).

24. Vaquette, C. & Cooper-White, J. J. Increasing electrospun scaffold pore size with tailored collectors for improved cell penetration. *Acta Biomater.* **7**, 2544–2557 (2011).

25. Fan, R. *et al.* Optimal elastomeric scaffold leaflet shape for pulmonary heart valve leaflet replacement. *J. Biomech.* **46**, 662–669 (2013).

26. Masoumi, N. *et al.* Tri-layered elastomeric scaffolds for engineering heart valve leaflets. *Biomaterials* **35**, 7774–7785 (2014).

27. Masoumi, N. *et al.* Electrospun PGS:PCL microfibers align human valvular interstitial cells and provide tunable scaffold anisotropy. *Adv. Healthc. Mater.* **3**, 929–939 (2014).

28. Bai, H. *et al.* Biomimetic gradient scaffold from ice-templating for self-seeding of cells with capillary effect. *Acta Biomater.* **20**, 113–119 (2015).

29. Kroehne, V. *et al.* Use of a novel collagen matrix with oriented pore structure for muscle cell differentiation in cell culture and in grafts. *J. Cell. Mol. Med.* **12**, 1640–1648 (2008).

30. Cornwell, K. G. & Pins, G. D. Discrete crosslinked fibrin microthread scaffolds for tissue regeneration. *J. Biomed. Mater. Res. A* **82A**, 104–112 (2007).

31. Yodmuang, S. *et al.* Silk microfiber-reinforced silk hydrogel composites for functional cartilage tissue repair. *Acta Biomater.* **11**, 27–36 (2015).

32. Kumar, V. A. *et al.* Collagen-Based Substrates with Tunable Strength for Soft Tissue Engineering. *Biomater. Sci.* **1**, (2013).

33. Kashiwabuchi, F. *et al.* Development of Absorbable, Antibiotic-Eluting Sutures for Ophthalmic Surgery. *Transl. Vis. Sci. Technol.* **6**, 1–1 (2017).

34. Zhao, S. *et al.* Wound dressings composed of copper-doped borate bioactive glass microfibers stimulate angiogenesis and heal full-thickness skin defects in a rodent model. *Biomaterials* **53**, 379–391 (2015).

35. Chrobak, M. O. *et al.* Design of a Fibrin Microthread-Based Composite Layer for Use in a Cardiac Patch. *ACS Biomater. Sci. Eng.* **3**, 1394–1403 (2017).

36. Caves, J. M. *et al.* The use of microfiber composites of elastin-like protein matrix reinforced with synthetic collagen in the design of vascular grafts. *Biomaterials* **31**, (2010).

37. Rajan, N., Habermehl, J., Coté, M.-F., Doillon, C. J. & Mantovani, D. Preparation of ready-to-use, storable and reconstituted type I collagen from rat tail tendon for tissue engineering applications. *Nat. Protoc.* **1**, 2753–2758 (2007).

38. Caves, J. M. *et al.* Fibrillogenesis in Continuously Spun Synthetic Collagen Fiber. *J. Biomed. Mater. Res. B Appl. Biomater.* **93**, (2010).

39. Kaiser, N. J., Kant, R. J., Minor, A. J. & Coulombe, K. L. Optimizing Blended Collagen-Fibrin Hydrogels for Cardiac Tissue Engineering with Human iPSC-derived Cardiomyocytes. *ACS Biomater. Sci. Eng.* (2018). doi:10.1021/acsbiomaterials.8b01112

40. Baselt, D. R., Revel, J. P. & Baldeschwieler, J. D. Subfibrillar structure of type I collagen observed by atomic force microscopy. *Biophys. J.* **65**, 2644–2655 (1993).

41. Bozec, L., van der Heijden, G. & Horton, M. Collagen Fibrils: Nanoscale Ropes. *Biophys. J.* **92**, 70–75 (2007).

42. Zeugolis, D. I. *et al.* Electro-spinning of pure collagen nano-fibres – Just an expensive way to make gelatin? *Biomaterials* **29**, 2293–2305 (2008).

43. Raub, C., Putnam, A., Tromberg, B. & George, S. Predicting bulk mechanical properties of cellularized collagen gels using multiphoton microscopy. *Acta Biomater.* **6**, 4657–4665 (2010).

44. Cook, C. S. & McDonagh, M. J. N. Measurement of muscle and tendon stiffness in man. *Eur. J. Appl. Physiol.* **72**, 380–382 (1996).

45. Iivarinen, J. T., Korhonen, R. K. & Jurvelin, J. S. Experimental and numerical analysis of soft tissue stiffness measurement using manual indentation device--significance of indentation geometry and soft tissue thickness. *Skin Res. Technol. Off. J. Int. Soc. Bioeng. Skin ISBS Int. Soc. Digit. Imaging Skin ISDIS Int. Soc. Skin Imaging ISSI* **20**, 347–354 (2014).

46. Iivarinen, J. T., Korhonen, R. K., Julkunen, P. & Jurvelin, J. S. Experimental and computational analysis of soft tissue stiffness in forearm using a manual indentation device. *Med. Eng. Phys.* **33**, 1245–1253 (2011).

47. Capulli, A. K., MacQueen, L. A., Sheehy, S. P. & Parker, K. K. Fibrous Scaffolds for Building Hearts and Heart Parts. *Adv. Drug Deliv. Rev.* **96**, 83–102 (2016).

48. Korinek, J. *et al.* Two-Dimensional Strain–A Doppler-Independent Ultrasound Method for Quantitation of Regional Deformation: Validation In Vitro and In Vivo. *J. Am. Soc. Echocardiogr.* **18**, 1247–1253 (2005).

49. Maganaris, C. N. & Paul, J. P. In vivo human tendon mechanical properties. *J. Physiol.* **521**, 307–313 (1999).

50. Cheng, X. *et al.* An electrochemical fabrication process for the assembly of anisotropically oriented collagen bundles. *Biomaterials* **29**, 3278–3288 (2008).

51. Pins, G. D., Christiansen, D. L., Patel, R. & Silver, F. H. Self-assembly of collagen fibers. Influence of fibrillar alignment and decorin on mechanical properties. *Biophys. J.* **73**, 2164–2172 (1997).

52. Park, H. *et al.* The Significance of Pore Microarchitecture in a Multi-Layered Elastomeric Scaffold for Contractile Cardiac Muscle Constructs. *Biomaterials* **32**, 1856–1864 (2011).

53. Neal, R. A. *et al.* Three-Dimensional Elastomeric Scaffolds Designed with Cardiac-Mimetic Structural and Mechanical Features. *Tissue Eng. Part A* **19**, 793–807 (2013).

54. Vollert, I. *et al.* In Vitro Perfusion of Engineered Heart Tissue Through Endothelialized Channels. *Tissue Eng. Part A* **20**, 854–863 (2013).

55. Lovett, M., Lee, K., Edwards, A. & Kaplan, D. L. Vascularization Strategies for Tissue Engineering. *Tissue Eng. Part B Rev.* **15**, 353–370 (2009).

56. Sarig, U. *et al.* Pushing the Envelope in Tissue Engineering: Ex Vivo Production of Thick Vascularized Cardiac Extracellular Matrix Constructs. *Tissue Eng. Part A* **21**, 1507–1519 (2015).

57. Dippold, D. *et al.* Novel approach towards aligned PCL-Collagen nanofibrous constructs from a benign solvent system. *Mater. Sci. Eng. C* **72**, 278–283 (2017).

58. Chakrapani, V. Y., Gnanamani, A., Giridev, V. R., Madhusoothanan, M. & Sekaran, G. Electrospinning of type I collagen and PCL nanofibers using acetic acid. *J. Appl. Polym. Sci.* **125**, 3221–3227 (2012).

59. Haaparanta, A.-M. *et al.* Preparation and characterization of collagen/PLA, chitosan/PLA, and collagen/chitosan/PLA hybrid scaffolds for cartilage tissue engineering. *J. Mater. Sci. Mater. Med.* **25**, 1129–1136 (2014).

60. Sadeghi-Avalshahr, A., Nokhasteh, S., Molavi, A. M., Khorsand-Ghayeni, M. & Mahdavi-Shahri, M. Synthesis and characterization of collagen/PLGA biodegradable skin scaffold fibers. *Regen. Biomater.* **4**, 309–314 (2017).

61. De Vrieze, S. *et al.* The effect of temperature and humidity on electrospinning. *J. Mater. Sci.* **44**, 1357 (2008).

62. Pelipenko, J., Kristl, J., Janković, B., Baumgartner, S. & Kocbek, P. The impact of relative humidity during electrospinning on the morphology and mechanical properties of nanofibers. *Int. J. Pharm.* **456**, 125–134 (2013).

CHAPTER 5: IN VITRO AND IN VIVO CHARACTERIZATION OF COLLAGEN MICROFIBER COMPOSITE CARDIAC TISSUES

8.1 Introduction

Ischemic heart disease (IHD) is responsible for 12.2% of all deaths worldwide[1], making it the leading cause of death in the world and a global health problem. IHD is typically caused by the accumulation of atherosclerotic plaques which either gradually restrict, or rapidly obstruct (in the case of plaque fracture), the coronary arteries, causing downstream tissue ischemia and cell death[2–5]. While surgical interventions can restore blood flow to the previously ischemic region, the development of stiff fibrotic scar combined with the extremely low expansion rate of the native cardiomyocyte population results in a region of stiff, non-contractile tissue, leading to permanently decreased heart function.

The enormous impact of this disease has led to great interest in the development of regenerative treatments that can restore function to heart tissue damaged by ischemia. Recent advances in stem cell biology and tissue engineering have created a viable path for the development of engineered cardiac tissue prepared in vitro, that could be implanted over ischemic regions to restore tissue function. However, current tissue engineering approaches are limited in their ability to emulate the mechanical microenvironment of native myocardium, a defining characteristic of the tissue. Given the role in determining cell phenotype and orientation that can now be attributed to the mechanical microenvironment[6–10], this represents an area of cardiac tissue engineering where innovation is needed.

Native myocardium is defined by an aligned network of cardiomyocytes connected via gap junctions, surrounded by a similarly oriented extracellular matrix. Together, these structures create an anisotropic material (i.e. stiffness in the longitudinal cardiac fiber direction significantly exceeds stiffness in the transverse cardiac fiber direction). Current approaches to creating anisotropy in engineered cardiac tissues either restrict tissue macro dimensions to enable the development of stress fields via tissue compaction along the length of a tissue strip or ring[11–13], or mandate fenestrations throughout the tissue[14–16]. While these approaches succeed in inducing cell alignment and tissue anisotropy, tissue rings and strips are not well suited for use as therapeutic patches and fenestrations reduce the contractile force of the engineered tissue, the primary functional output of all muscle tissue. A recently developed strategy that enables the fabrication of anisotropic cardiac tissues without tissue geometry limitations may offer a more desirable alternative[17].

Herein, we evaluate the in vitro and in vivo performance of mechanically anisotropic cardiac tissues produced using our recently described bespoke collagen microfiber meshes seeded with human induced pluripotent stem cell-derived cardiomyocytes (hiPSC-CMs). Two fibrous mesh designs are tested; a parallel fiber mesh of 100 μm diameter fibers with 200 μm fiber spacing (referred to as "Parallel") and a 30° fiber angle mesh composed of two overlapping layers of 100 μm diameter fibers with 200 μm fiber spacing that form 30° fiber angles (referred to as "30°"). The fibrous tissue designs are compared to fiber-free, "no fiber", control constructs (referred to as "NF"). Additionally, two hydrogel bulk collagen concentrations were evaluated (0.8 mg/mL and 1.2 mg/mL) to study the impact of this parameter of composite tissue development and function. Tissue compaction and immunohistochemical staining for myofilament and gap junction proteins were used to evaluate cardiac tissue development, and passive and active mechanical properties were evaluated in vitro as functional metrics of the contractile engineered cardiac tissue. Finally, fibrous composites were implanted in a rat ischemia/reperfusion model of myocardial infarction to evaluate the degradation and remodeling of the embedded fibers in the cardiac microenvironment. Together these results demonstrate the functional contributions of embedded collagen microfibers in engineered cardiac tissues in vitro and form a foundation for further study of this tunable platform for engineered cardiac tissues.

8.2 Materials and Methods

8.2.1 Cardiomyocyte differentiation

Cardiomyocytes were differentiated from human induced pluripotent stem cells (hiPSCs; GCaMP6 WTC hiPSCs from Bruce Conklin, The Gladstone Institutes) via small molecule modulation of the Wnt signaling pathway as previously described[11,14]. Briefly, hiPSCs cultured on Matrigel-coated 24 well polystyrene tissue culture plates were treated with 4.5 µM Chiron 99021 (Tocris), a glycogen synthase kinase 3 (GSK3) inhibitor at day 0, followed by 5 µM IWP2 (Tocris), a Wnt inhibitor at day 3. Cardiac phenotype, demonstrated by beating behavior, was typically first observed between day 9 and day 14. Cardiomyocytes differentiated from hiPSCs were used for the fabrication of cellularized constructs between differentiation day 13 and 18. Cardiac purity was measured via flow cytometry analysis with a cardiac-specific antibody to cardiac troponin T (cTnT) on every batch of cells used for the preparation of cellularized constructs. Purity was defined by the percentage of cTnT positive cells.

8.2.2 Preparation of collagen microfiber meshes

Collagen microfiber meshes were fabricated via an automated process as described previously[17]. Briefly, collagen I was isolated from rat tail tendons via acetic acid extraction and salt precipitation followed by dilution to a stock concentration of 13 mg/mL. The collagen stock solution was extruded via spinneret into a 1 m length of polyethylene tubing filled with a high viscosity buffer solution (34.5 mM potassium phosphate monobasic, 85.2 mM sodium phosphate dibasic, 135 mM sodium chloride, 29.9 mM HEPES buffer, 8.57 mM polyethylene glycol (PEG) MW 35,000), creating a coaxial flow system. The collagen was precipitated from solution as it traveled the length of the tubing, forming into a collagen hydrogel microfiber that exited into a 250 cm long bath filled with 70% ethanol. Using forceps, the end of the fiber was collected and then placed onto the mandrel of the automated collection device, which consists of two stepper motors that control the translation and rotation of the mandrel, driven by an Arduino microcontroller preloaded with a mesh design protocol. Translation and rotation of the mandrel during collection creates a fiber mesh with the prescribed pattern. Two mesh patterns were considered in this study: a "parallel" mesh pattern defined by parallel collagen microfibers with 200 µm spacing between the fibers, as well as a "30°" mesh pattern defined by two overlapping sets of parallel collagen microfibers with 200 µm spacing between the fibers, such that the overlapping fibers form 30° angles (Fig 5.1 A).

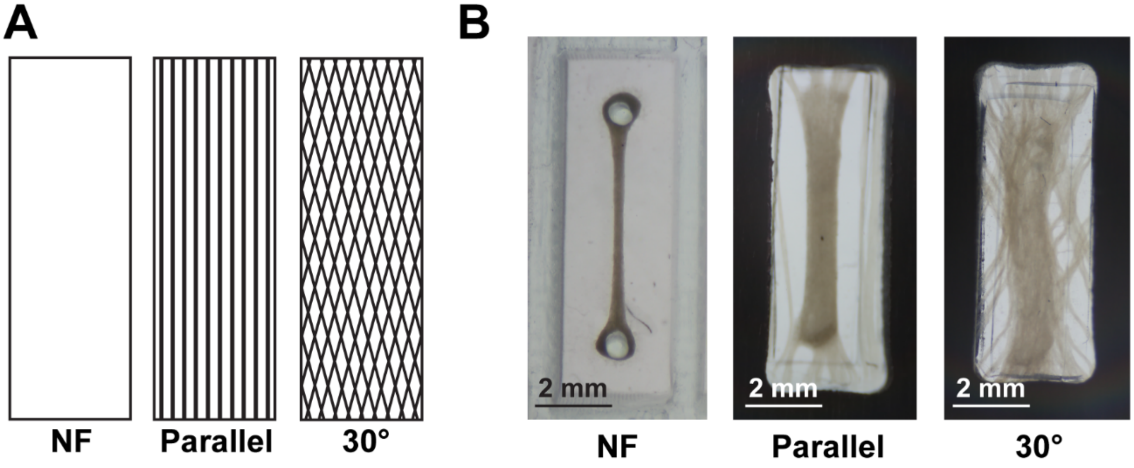

Figure 5. 1: Engineered cardiac tissue construct formats. A) Schematic drawing of "no-fiber" control constructs, parallel fiber constructs, and 30° fiber angle constructs. B) Representative images of the tissue constructs after 10 days in culture conditions.

8.2.3 Fabrication of composite cardiac tissues

Collagen microfiber meshes were collected and embedded in a hydrogel bulk seeded with cardiomyocytes as described previously[17]. Briefly, rigid capture frames with 3 mm x 9 mm windows were fabricated from 3 mm thick 316 stainless steel. 2 mm thick polydimethylsiloxane (PDMS) gaskets with matching dimensions were fabricated and one was paired with each rigid capture frame. Prior to mesh capture, all components of the capture frame system were autoclaved. Using an alignment jig, wet spun collagen microfiber meshes were captured between a pair of the PDMS gaskets, held in place by the stainless steel frames, which were then screwed together with autoclaved 316 stainless steel screws to hold the fibers in place. Prior to casting, press-fit PDMS plugs were inserted into the open window of one of the stainless steel frames, creating a casting basin surrounding the capture mesh, between the plug and the PDMS gaskets. Each captured mesh was placed into the well of an untreated polystyrene six well plate, such that the casting basin faced upwards. hiPSC-CMs were harvested as described previously[11,14,18]. A casting mix of neutralized 0.8 mg/mL or 1.2 mg/mL collagen I and 15e6 cells/mL cardiomyocytes in 1X DMEM was prepared, and 70 µL of the solution was pipetted on top of each captured mesh. Once casting was complete, constructs were placed in a 37°C, 5% CO_2 incubator for 30 minutes to allow the collagen to polymerize. The composite constructs were then covered with a maintenance media of RPMI+B27+1:100 Penicillin/Streptomycin. Stimulator lids were put in place before returning the constructs to the incubator for 10 days of tissue culture (Fig 5.1 B).

Control tissues were prepared identically but were cast in 3 mm x 9 mm PDMS tissue culture molds with 0.5 mm diameter round posts at either end. Cardiomyocyte purity, defined as the cardiac troponin T (cTnT) positive population via fluorescent activated cell sorting (FACS) analysis, averaged 53.8±4.3% (58.0%, 58.2%, and 45.1% for harvest batches 1, 2, and 3, respectively).

8.2.4 Cardiac tissue culture and stimulation

All constructs were stimulated for the duration of the culture period using a C-Pace EP system with six-well C-dish electrode assembly lids (IonOptix). This system is composed of stimulator lids with pairs of carbon electrodes for each well of a six well plate. Carbon electrodes extend into the culture medium and are positioned on opposite sides of the engineered tissues. A ribbon cable connects the stimulator lid to the stimulator bank outside of the incubator. Constructs were field stimulated with a 1 Hz, 10.0 V (5 V/cm), 4.0 ms duration bi-polar pulse train for the full culture period. Constructs were fed every other day with construct maintenance media for the full culture period of 10 days.

8.2.5 Analysis of compaction in engineered cardiac tissues

Constructs were imaged under a dissecting microscope scope (Canon 6D via Olympus SZ40) at the day 10 timepoint, and visible construct area was assessed using image analysis software (ImageJ). Day 10 construct area is reported as a percentage of the known initial construct area based on mold dimensions (27 mm^2).

8.2.6 Active mechanical analysis of engineered cardiac tissues

All mechanical testing was performed in an Aurora Scientific 801C small intact muscle apparatus equipped with a 322C high speed length controller, temperature controlled bath, bipolar platinum stimulation electrodes, and a 5 mN load cell. Both active and passive testing was performed in a 37°C bath of Tyrode's solution (1.8 mM CaCl2, 1.0 mM MgCl2, 5.4 mM KCl, 140 mM NaCl, 0.33 mM NaH2PO4, 10 mM HEPES, 5 mM Glucose). Prior to testing, initial sample thicknesses were measured via micrometer and initial sample lengths were measured via calipers. Samples were mounted for active analysis either with aluminum t-clips or mounted directly to hooks on the lever arm and load cell (identical mounting strategies were used for every sample within each experiment). T-clips are “T” shaped pieces of 0.1 mm thick aluminum foil with two tabs that can be folded over the sample to hold it in place, and a third tab with a hole compatible with the hooks mounted to the lever arm and load cell. Samples were loaded with a 0.1 mN preload prior to each testing protocol. Active mechanical testing was performed by measuring construct contraction force at strains of 5, 10, and 15 percent, held for 120 seconds at each length to allow for stress relaxation and electrically stimulated at 1 Hz during the final 20 seconds of each step to capture twitch contractions. Peak active stress was calculated at 15% strain, normalized for cross-sectional area.

8.2.7 Passive mechanical analysis of engineered cardiac tissues

Passive mechanical analysis was performed following active mechanical analysis under the same physiological conditions (37°C bath of Tyrode’s solution). To permit evaluation at high strains, T-clips were used for analysis of the composite tissues. Samples were loaded with a 0.1 mN preload prior to each testing protocol. Samples were then pulled at a constant strain rate of 10% strain/minute until sample failure. Young’s modulus was calculated from the linear region of each sample’s stress vs. strain curve (usually between 5% and 15% strain).

8.2.8 Immunohistochemistry

Constructs designated for immunohistochemistry were fixed in 4% paraformaldehyde (PF) for 10 minutes at room temperature, stored in PBS, and then embedded in optimal cutting temperature compound (OCT). Frozen blocks samples were sectioned and then stained for DAPI, α-actinin (a cardiomyocyte marker), and connexin 43 (Cx43, a cardiomyocyte gap junction protein). Stained sections were imaged on a confocal microscope (Olympus FV3000).

8.2.9 Evaluation in a rat model of myocardial infarction

Composite and control constructs samples were evaluated in a previously described rat model of myocardial infraction[14] at two weeks post-implantation. All animal procedures were conducted in accordance with the U.S. NIH Policy on Humane Care and Use of Laboratory Animals and the Brown University Institutional Animal Care and Use Committee. Briefly, myocardial infarcts were induced in 8-week old (250 g) Sprague Dawley rats (Charles River Laboratory) by ischemia/reperfusion via a temporary ligation of the left anterior descending (LAD) coronary artery for 60 minutes followed by reperfusion. Four days after the ischemia/reperfusion injury, engineered cardiac tissue constructs were implanted over the ischemia-damaged and blanched region, held in place by sutures. Due to the small dimensions of tissues investigated in this study, two constructs were implanted side by side. Fourteen days after the implant surgery, the animals were sacrificed by pentobarbital overdose (180 mg/kg) and hearts were harvested for histological assessment.

8.2.10 Statistical analysis

All statistical analyses were performed in Prism 8 (GraphPad Inc., San Diego, CA). For comparison between two groups, Student's t-tests were used. For comparisons of more than two groups, one way analysis of variance (ANOVA) with multiple comparisons and Tukey's post-hoc test was used unless otherwise noted. Error bars represent standard error of the mean (SEM). Group differences were considered statistically significant for p-values < 0.05.

8.3 Results

8.3.1 Embedded collagen fiber mesh geometries modulate tissue compaction

The dynamic process of cardiac tissue formation depends upon cells binding to the extracellular matrix and compacting the hydrogel as a precursor to cardiac tissue syncytium development[19]. Therefore, we hypothesized that embedding a collagen fiber mesh, where individual fibers have stiffnesses on the order of 1.5 MPa[17], would decrease compaction in a fiber-orientation-dependent manner. To evaluate the impact of the hydrogel bulk composition, both 0.8 mg/mL and 1.2 mg/mL collagen concentrations were considered. Prior to construct harvest at 10 days, gross images of each cardiac tissue construct were collected to quantify tissue area (Fig 5.1 B). Data normalized to initial area at day 0 shows highly compact tissues with a low percent area.

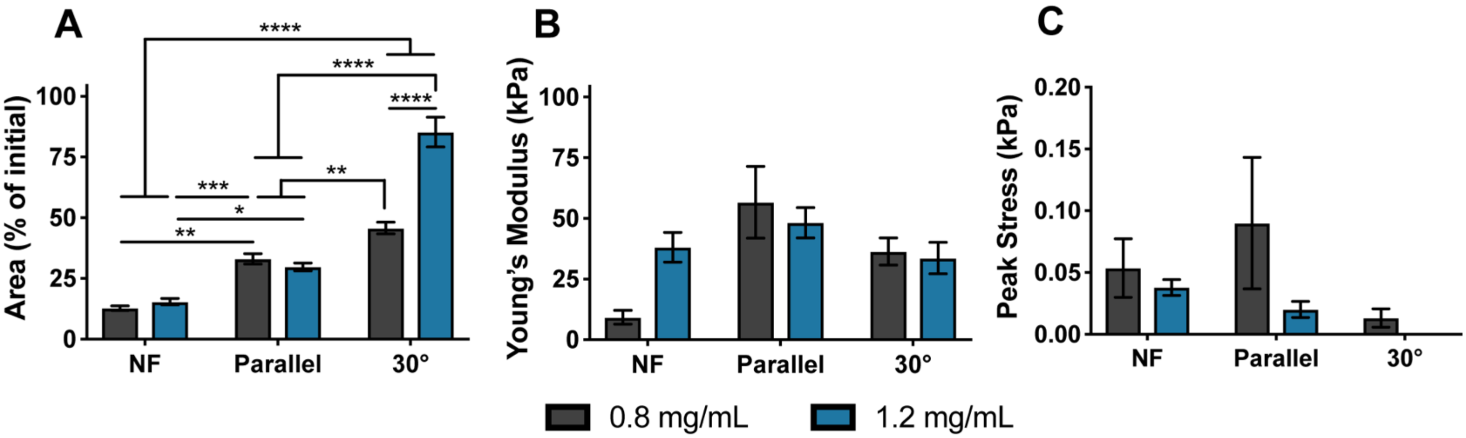

Figure 5. 2: Engineered cardiac tissue compaction and passive and active mechanics. A) Visible construct area relative to initial construct area, B) Young's modulus, and C) Peak contraction stress for cardiac tissue constructs at 10 days. Black and blue bars represent tissues prepared with 0.8 mg/mL and 1.2 mg/mL collagen, respectively. $n \geq 5$ for all groups except for the 0.8 mg/ml NF group where $n = 3$ due to sample breakage during culture as we previously reported[19]. Error bars represent SEM. * indicates $p<0.05$, ** indicates $p<0.01$, *** indicates $p<0.001$, and **** indicates $p<0.0001$.

Significantly greater tissue compaction occurred in all formulations of the control and parallel fiber groups compared to the 30° fiber constructs seeded with both collagen concentrations (45.74±2.40% for 0.8 mg/mL and 85.24±6.12% for 1.2 mg/ml, $p<0.0001$; Fig 5.2 A). Significantly greater compaction was also observed in the constructs without fibers compared to the parallel fiber constructs regardless of bulk hydrogel concentration. These significant differences between composites and controls demonstrate that embedded collagen fibers reduce compaction in an architecture-dependent manner. With respect to hydrogel bulk concentrations, the only significant difference in compaction within a fiber design group was observed with the 30° fiber angle constructs reported above, suggesting that transverse constraint due to fiber orientation significantly impacts compaction and tissue formation.

8.3.2 Embedded collagen microfibers do not significantly alter tissue mechanics

Tensile Young's modulus of engineered cardiac tissue is a metric of both initial scaffold composition, as well as the remodeling phenomena that occur during tissue culture. Final Young's modulus is an important parameter both for evaluating the physiological relevance of engineered cardiac tissue, as well as understanding the mechanical cues this environment is providing to resident cells. All samples were evaluated at a strain rate of 10% strain per minute following stretch to 15% strain via the active mechanics protocol (see section 5.2.6)

Young's modulus was consistent across all design and composition groups with no observed significant differences. The Young's modulus for the 0.8 mg/mL NF group (9.27±2.84 kPa) was nominally lower than for the 1.2 mg/mL NF group (38.09±6.11 kPa) but the difference did not reach significance, likely because of the small number of samples in the 0.8 mg/mL NF group (n=3) due to mechanical failure during culture. Passive stiffness values for the composite groups ranged from 33.64±6.44 kPa (30° with 1.2 mg/mL) to 56.64±14.79 kPa (parallel with 0.8 mg/mL).

Peak twitch stress, defined as the maximum active stress observed in the sample, was evaluated as a functional metric of contractile activity in the engineered cardiac tissues. Peak stress was evaluated at 15% strain during 1 Hz electrical field stimulation for all samples.

No significant differences in peak stress were observed between any of the groups evaluated (Fig 5.2 C). However, the mean peak twitch stress generated by the parallel fiber constructs prepared with 0.8 mg/mL collagen exceeded the peak twitch stress of the control samples prepared with either collagen concentration. This nominal difference can be attributed to two parallel fiber constructs that exceeded the greatest peak stresses generated by the control tissues, yielding peak stress values of 0.117 kPa and 0.553 kPa compared to a maximum NF control group value of 0.088 kPa. These nominal differences failed to satisfy statistical significance due in part to the high degree of variability, particularly in the parallel fiber group. In all cases the nominal mean values for the 30° fiber groups fell below those of both the parallel fiber group and the fiber-free controls.

8.3.3 Immunohistological staining shows mature cardiomyocyte phenotype in parallel fiber constructs

Stiffness, tension, and organization of the engineered cardiac tissue microenvironment has been shown to direct cardiomyocyte phenotype[6,20,21]. Immunohistological staining for markers of cardiomyocyte maturity and organization was used to assess the impact of the scaffold format on resident cardiomyocyte phenotype.

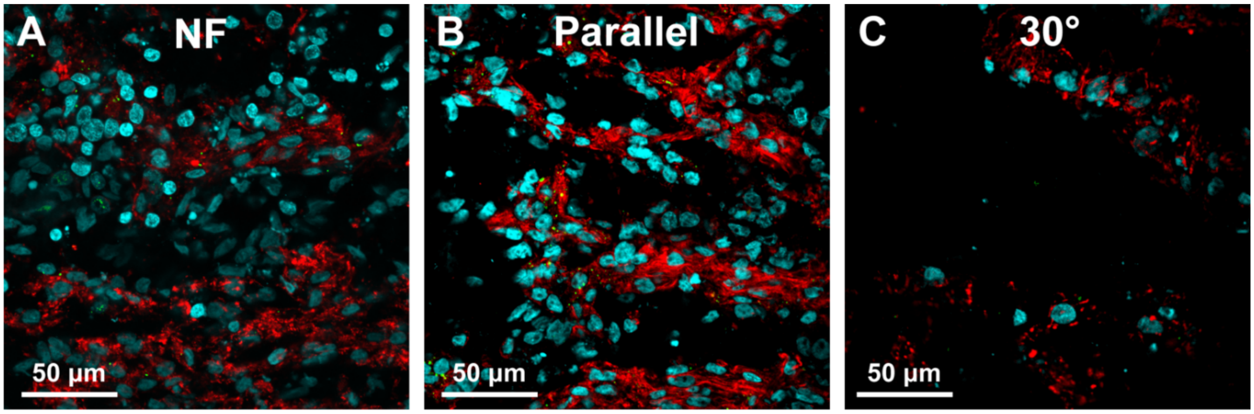

Figure 5. 3: Immunohistochemistry of engineered cardiac tissues. Representative frozen block histology sections of 0.8 mg/mL collagen constructs stained with α-actinin (red), Cx43 (green), and DAPI (blue) for A) control tissues without fibers, B) parallel fiber tissues, and C) 30° fiber angle tissues. All images are presented in the horizontal tissue orientation.

Parallel fiber engineered cardiac tissues and control tissues without fibers stained for α-actinin (a marker of the z-disc of sarcomeres), Cx43 (a cardiac gap junction protein) and DAPI show high densities of α-actinin positive cells with banding characteristics typical of a developing myofilament lattice. In the case of the parallel fiber constructs, α-actinin staining appeared to be aligned parallel to orientation of the embedded collagen microfibers. Punctate Cx43 staining indicates the presence of gap junctions localized between adjacent cells in these tissue groups, supporting our visual identification of uniform beating or syncytium development (Fig 5.3 A, B). Conversely, engineered cardiac tissues prepared with 30° fiber angle meshes do not exhibit the same well-defined α-actinin banding and alignment or clear Cx43 staining, suggesting diminished presence of both myofilament organization and gap junction formation (Fig 5.3 C).

8.3.4 Embedded, uncrosslinked collagen microfibers persist in the cardiac microenvironment after two-weeks

Parallel and 30° composite fiber constructs were implanted in a rat model of myocardial infarction (MI, see section 5.2.9). Remodeling and degradation of the embedded collagen microfibers was assessed at the two-week timepoint. Ultrasound analysis of metrics of cardiac function (fractional shortening and ejection fraction) showed no significant differences post-MI or between groups at the two-week time point (data not shown).

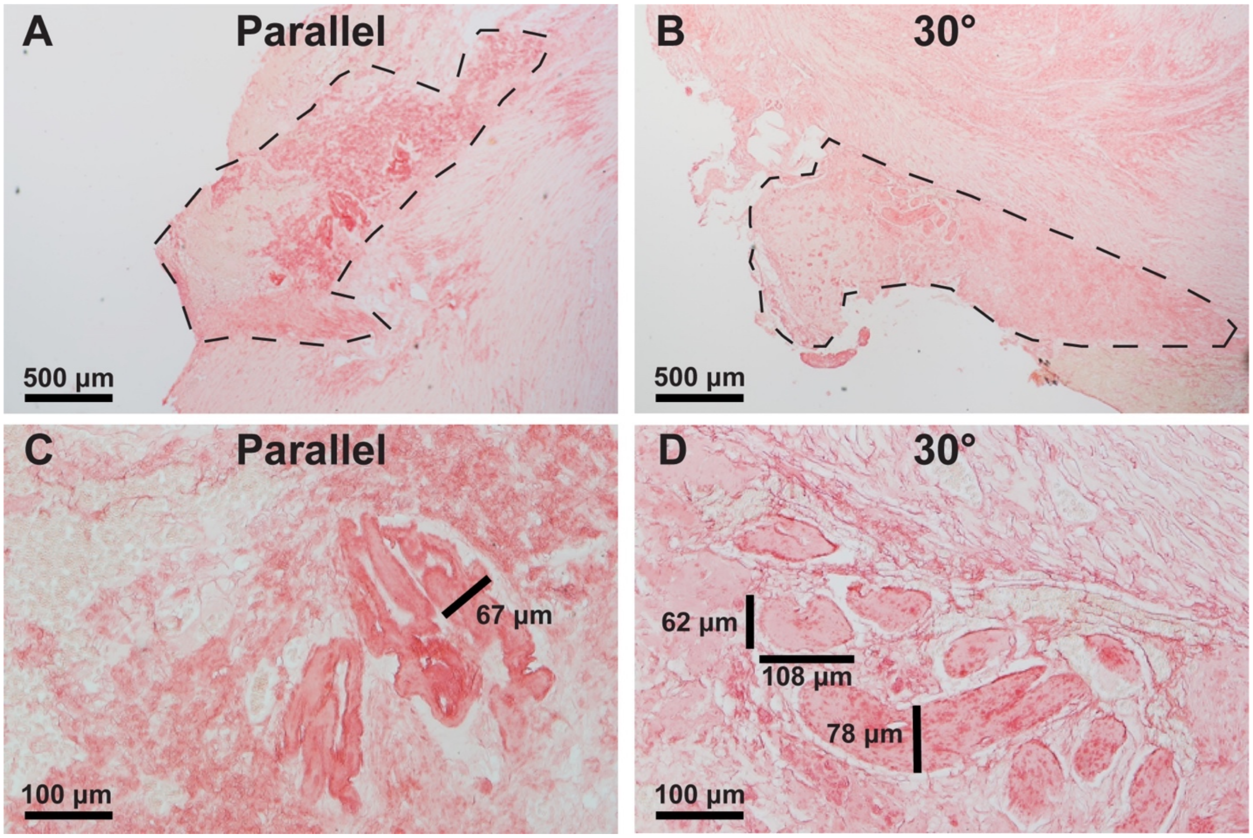

Figure 5. 4: Composite constructs implanted in the cardiac microenvironment. Representative histology images show picosirius red to identify collagen for parallel (A and C) and 30° (B and D) composite constructs implanted in a rat model of myocardial infarction at two weeks post-implantation. Dotted lines outline the composite constructs on the surface of the epicardium. Microfibers are defined by dark red staining and measurements are an assessment of fiber diameter.

After two weeks implanted over an ischemic region of the myocardium, qualitative assessment of fiber integrity by picrosirius red staining of heart sections showed minimal fiber degradation and remodeling. Collagen microfibers were identified in animals implanted with either parallel or 30° fiber angle implants. Collagen microfiber borders appeared to be intact with no evidence of cellular ingrowth into the fibers. Morphometric analyses demonstrated fiber diameters of 60 – 100 µm (Fig 5.4 C, D), which approximate the known diameter of the hydrated collagen wet-spun microfibers (~80 – 100 µm)[22]) and suggest persistence of fibers for >2 weeks in vivo in the heart.

8.4 Discussion

The objective of this study was to evaluate the development and functional performance of engineered cardiac tissues prepared with embedded collagen microfiber meshes, designed to impart mechanical anisotropy in order to improve cardiomyocyte structure and function, and thereby increase force production by the tissue. Anisotropic single-layer parallel fiber and two-layer 30° fiber angle composite tissues were compared to fiber-free tissues for tissue compaction, myofilament development and alignment, and active and passive mechanics at 10 days. Additionally, embedded collagen microfiber degradation and remodeling after 2 weeks in the cardiac microenvironment in a rat model of myocardial infarction were assessed.

Compaction analysis by tissue area showed significant differences between all three fiber groups, and between different collagen concentrations for the 30° fiber angle group. Constructs prepared without fibers exhibited the greatest degree of compaction, even when cast with a higher bulk collagen concentration. In comparison to the parallel fiber constructs, this difference (12.78±0.94% and 15.47±1.31% vs. 33.09±2.15% and 29.78±1.63% of initial area for 0.8 and 1.2 mg/mL collagen, respectively) can be attributed to effective increases in parallel fiber scaffold stiffness in both directions (due to the collagen microfiber bending stiffness in the transverse fiber orientation and tensile stiffness in the longitudinal orientation). Similarly, the further decreased compaction in the 30° fiber constructs compared to the parallel fiber constructs (33.09±2.15% and 29.78±1.63% vs. 45.74±3.40% and 85.24±6.12% for 0.8 and 1.2 mg/mL collagen, respectively) can be attributed to even greater effective stiffness in both transverse and longitudinal directions, as well as the greater number of fibers (two layers of fibers spaced 200 µm apart vs one layer of similarly spaced fibers). While the parallel fiber scaffold design fixed fibers in place only on the top and bottom edge of the gasket frame, minimizing the mechanical contribution of the fibers in the transverse orientation, the diagonal fiber orientation in the 30° fiber angle constructs resulted in fibers fixed in place on all sides of the gasket, enabling tensile fiber stiffness contributions in all directions (Fig 5.1 B).

Assessments of the passive stiffness showed no significant differences between the groups, while previous experiments have shown significantly greater stiffness in similar acellular collagen microfiber composites compared to collagen hydrogels without fibers[19]. This observed normalization of tissue mechanics may be attributed to remodeling and cellular force production directed by the resident cell population. The degree of tissue compaction appears to be inversely related to the predicted acellular stiffness of each of the tissue formats (due to 0, 1, or 2 fiber layers), and tissue compaction is known to greatly increase tissue stiffness by effectively increasing the density of the scaffold polymer[19,23]. In the case of the fibrous composites, compaction results in an increase in fiber density as well. The range of absolute stiffness values for all of the composite construct groups (33.64±6.44 kPa to 56.64±14.79 kPa) as well as the stiffness value for the 1.2 mg/mL no fiber group (38.09±6.11 kPa) closely approximated empirical values for native rat myocardium in the long fiber direction collected using identical methods (30.80±2.71 kPa)[19], while the passive stiffness of the 0.8 mg/mL no fiber group fell short (9.27±2.84 kPa). The high degree of compaction observed in this group, paired with low passive stiffness values and failure due to necking and breaking, are clear indicators that the scaffold composition in these failed tissues was insufficient to support tissue development.

The downstream effects of increased scaffold stiffness leading to reduced tissue compaction was observed via immunohistochemical analysis. Parallel fiber composite and fiber-free control tissues demonstrated good cardiomyocyte phenotype in the form of α-actinin banding and punctate Cx43 staining indicative of contractile lattice development and gap junction formation, respectively. However, the less compacted 30° angle constructs demonstrated poor α-actinin banding and Cx43 staining, indicating poor tissue maturation or development of the cardiomyocyte phenotype. Without sufficient compaction, resident cardiomyocytes may have failed to form cell-cell connections with other resident cells, reducing transmission of cell-cell signaling factors, and thereby limiting tissue development.

The role of compaction in tissue development has been well studied in the field of tissue engineering, particularly with respect to tissue deformation or mechanical failure caused by uncontrolled compaction[23–27]. The accepted paradigm is that scaffold parameters, primarily matrix stiffness, resist tissue compaction while cell mediated protease release, actomyosin contractile forces, and adhesion sites encourage compaction[19,25,28,29]. In the case of engineered cardiac tissue, functional performance is dependent on achieving a maximal density of cardiomyocytes in the engineered tissue to ensure gap junction formation and to maximize contractile force generation, without encouraging so much contraction as to cause tissue failure. In the case of the fibrous composite tissues, the threshold for mechanical failure is effectively increased due to the high tensile strength of the embedded collagen microfibers. This provides good justification for the future evaluation of bulk hydrogel casting mixes for composite tissues with even lower collagen concentrations and higher seeding densities than have been evaluated previously in fiber-free constructs, as these parameters have been empirically linked to increased compaction[19].

Across all cardiomyocyte batches and construct groups evaluated, no significant differences were found in peak twitch stress between fiber-free control tissues and tissues prepared with the embedded collagen microfiber meshes. Notably, the fiber-free constructs yielded the highest percentage of beating and contractile constructs (86% for NF vs 67% for parallel and 44% for 30°), further supporting prior optimization work[19]. In all cases the 30° fiber angle constructs generated nominally lower mean peak stress values than both the fiber-free and the parallel fiber construct groups. However, in two of the three cardiomyocyte batches evaluated, parallel fiber mesh constructs generated the greatest contractile force of all constructs tested, and in one case a parallel fiber mesh produced contractile forces more than five times greater than any construct produced by any other group (0.553 kPa). It is notable that this construct exhibited a greater degree of compaction and the smallest cross-sectional area of any sample in its batch and group. Despite the excellent performance of this tissue, the threshold of statistical significance was not satisfied in part due to high variability, especially in the composite tissue groups.

Variability presents a continuous challenge for the field of tissue engineering due to the complexity and sensitivity of cell mediated tissue development. However, the increased variability associated with the fibrous composites evaluated in this study relative to the fiber-free controls suggests that further refinement of mesh designs as well as the capture, casting, and testing process may yield more consistent results in the future. A first step would be the evaluation of parallel fiber constructs with both increased fiber spacing (which would both reduce resistance to compaction and decrease mesh variability, as previously demonstrated[19]) and decreased hydrogel bulk concentration, as described above, to eliminate insufficient compaction as a failure mode.

Finally, minimally crosslinked collagen microfibers embedded in engineered cardiac tissue and implanted in the cardiac microenvironment in a rat model of myocardial infarction were shown to persist at the two-week timepoint as evidenced by picosirius red staining for collagen (Fig 5.4). Maintenance of microfiber size and the presence of intact borders suggest that these fibers were minimally degraded and remodeled at this timepoint. Other studies have shown degradation of similar collagen microfibers at the 6 week timepoint with a subdermal implantation site[22], but to our knowledge this is the first evaluation of collagen microfibers implanted in this format on the epicardium of the heart. Persistence of these fibers at the two-week timepoint demonstrates an ability to provide structural support in vivo to implanted and host tissue, as well as to maintain biophysical alignment of cardiomyocytes. Persistent, embedded collagen microfibers may also offer utility by guiding invading host endothelial cells to encourage vascularization, as was evaluated in a poly(glycerol sebacate) and poly(ε-caprolactone) format by Gaharwar et. al.[30], or by providing anisotropic reinforcement to the heart following myocardial infarction, which shows promise as a method of improving heart function[31,32].

8.5 Conclusion

In this study we evaluated the in vitro tissue development and functional performance of engineered cardiac tissues prepared with embedded collagen microfiber meshes designed to impart mechanical anisotropy. Microfiber meshes were found to modulate tissue development, decreasing tissue compaction dependent on mesh geometry when compared to control tissues prepared without fiber meshes. Staining for cardiac markers revealed native-like cardiomyocyte phenotypes in constructs prepared with parallel fiber arrays and fiber-free controls, but poor cardiomyocyte phenotypes in composite tissues prepared with a geometry that limited tissue compaction. Although no significant differences in either passive or active mechanical properties were found, the greatest peak twitch contraction stresses were observed in constructs prepared with the embedded collagen microfibers in a parallel array. Together, these results demonstrate a role for embedded collagen microfibers in modulating tissue development and justify further studies to reduce variability and optimize these anisotropic composite cardiac tissues for cardiac regeneration.

8.6 References

1. World Health Organization. *The Global Burden of Disease: 2004 Update*. (2008).
2. Chilton, R. J. Pathophysiology of Coronary Heart Disease: A Brief Review. *J. Am. Osteopath. Assoc.* **104**, 5S-8S (2004).
3. Vaccarino, V. *et al.* Presentation, management, and outcomes of ischaemic heart disease in women. *Nat. Rev. Cardiol.* **10**, 508–518 (2013).
4. Kandaswamy, E. & Zuo, L. Recent Advances in Treatment of Coronary Artery Disease: Role of Science and Technology. *Int. J. Mol. Sci.* **19**, (2018).
5. Kaski Juan-Carlos, Crea Filippo, Gersh Bernard J. & Camici Paolo G. Reappraisal of Ischemic Heart Disease. *Circulation* **138**, 1463–1480 (2018).
6. Jacot, J. G., McCulloch, A. D. & Omens, J. H. Substrate Stiffness Affects the Functional Maturation of Neonatal Rat Ventricular Myocytes. *Biophys. J.* **95**, 3479–3487 (2008).
7. Jacot, J. G., Martin, J. C. & Hunt, D. L. Mechanobiology of Cardiomyocyte Development. *J. Biomech.* **43**, 93 (2010).
8. Boothe, S. D. *et al.* The Effect of Substrate Stiffness on Cardiomyocyte Action Potentials. *Cell Biochem. Biophys.* 1–9 (2016). doi:10.1007/s12013-016-0758-1
9. Kai, D., Prabhakaran, M. P., Jin, G. & Ramakrishna, S. Guided orientation of cardiomyocytes on electrospun aligned nanofibers for cardiac tissue engineering. *J. Biomed. Mater. Res. B Appl. Biomater.* **98B**, 379–386 (2011).
10. Kuppan, P., Sethuraman, S. & Krishnan, U. M. Interaction of human smooth muscle cells with nanofibrous scaffolds: Effect of fiber orientation on cell adhesion, proliferation and functional gene expression. *J. Biomed. Mater. Res. A* n/a-n/a (2014). doi:10.1002/jbm.a.35360
11. Rupert, C. E. & Coulombe, K. L. K. IGF1 and NRG1 Enhance Proliferation, Metabolic Maturity, and the Force-Frequency Response in hESC-Derived Engineered Cardiac Tissues. *Stem Cells International* (2017). doi:10.1155/2017/7648409
12. Eschenhagen, T. *et al.* 3D engineered heart tissue for replacement therapy. *Basic Res. Cardiol.* **97**, I146–I152 (2002).
13. Zimmermann, W.-H. *et al.* Engineered heart tissue grafts improve systolic and diastolic function in infarcted rat hearts. *Nat. Med.* **12**, 452–458 (2006).
14. Munarin, F., Kaiser, N. J., Kim, T. Y., Choi, B.-R. & Coulombe, K. L. K. Laser-Etched Designs for Molding Hydrogel-Based Engineered Tissues. *Tissue Eng. Part C Methods* **23**, 311–321 (2017).
15. Bian, W., Badie, N., Himel IV, H. D. & Bursac, N. Robust T-tubulation and maturation of cardiomyocytes using tissue-engineered epicardial mimetics. *Biomaterials* **35**, 3819–3828 (2014).
16. Engelmayr, G. C. *et al.* Accordion-like honeycombs for tissue engineering of cardiac anisotropy. *Nat. Mater.* **7**, 1003–1010 (2008).
17. Kaiser, N. J., Bellows, J. A., Kant, R. J. & Coulombe, K. L. K. Digital Design and Automated Fabrication of Bespoke Collagen Microfiber Scaffolds. *Tissue Eng. Part C Methods* (In press).
18. Kaiser, N. J., Munarin, F. & Coulombe, K. L. K. Custom Engineered Tissue Culture Molds from Laser-etched Masters. *JoVE J. Vis. Exp.* e57239–e57239 (2018). doi:10.3791/57239
19. Kaiser, N. J., Kant, R. J., Minor, A. J. & Coulombe, K. L. K. Optimizing Blended Collagen-Fibrin Hydrogels for Cardiac Tissue Engineering with Human iPSC-derived Cardiomyocytes. *ACS Biomater. Sci. Eng.* **5**, 887–899 (2019).
20. Jacot, J. G. *et al.* Cardiac Myocyte Force Development during Differentiation and Maturation. *Ann. N. Y. Acad. Sci.* **1188**, 121–127 (2010).
21. Bhana, B. *et al.* Influence of substrate stiffness on the phenotype of heart cells. *Biotechnol. Bioeng.* **105**, 1148–1160
22. Caves, J. M. *et al.* Fibrillogenesis in Continuously Spun Synthetic Collagen Fiber. *J. Biomed. Mater. Res. B Appl. Biomater.* **93**, (2010).
23. Ogle, B. M. & Mooradian, D. L. The Role of Vascular Smooth Muscle Cell Integrins in the Compaction and Mechanical Strengthening of a Tissue-Engineered Blood Vessel. *Tissue Eng.* **5**, 387–402 (1999).

24. Wang, H. *et al.* Necking and failure of constrained 3D microtissues induced by cellular tension. *Proc. Natl. Acad. Sci. U. S. A.* **110**, 20923–20928 (2013).
25. Turlier, H. & Maître, J.-L. Mechanics of tissue compaction. *Semin. Cell Dev. Biol.* **47**–**48**, 110–117 (2015).
26. Fernandez, P. & Bausch, A. R. The compaction of gels by cells: a case of collective mechanical activity. *Integr. Biol. Quant. Biosci. Nano Macro* **1**, 252–259 (2009).
27. Han, E., Ge, C., Chen, A. C., Schumacher, B. L. & Sah, R. L. Compaction Enhances Extracellular Matrix Content and Mechanical Properties of Tissue-Engineered Cartilaginous Constructs. *Tissue Eng. Part A* **18**, 1151–1160 (2012).
28. van Vlimmeren, M. A. A., Driessen-Mol, A., Oomens, C. W. J. & Baaijens, F. P. T. An In Vitro Model System to Quantify Stress Generation, Compaction, and Retraction in Engineered Heart Valve Tissue. *Tissue Eng. Part C Methods* **17**, 983–991 (2011).
29. Brugmans, M. M. C. P., Driessen-Mol, A., Rubbens, M. P., Cox, M. A. J. & Baaijens, F. P. T. Poly-ε-caprolactone scaffold and reduced in vitro cell culture: beneficial effect on compaction and improved valvular tissue formation. *J. Tissue Eng. Regen. Med.* **9**, E289-301 (2015).
30. Gaharwar, A. K., Nikkhah, M., Sant, S. & Khademhosseini, A. Anisotropic poly (glycerol sebacate)-poly (ϵ-caprolactone) electrospun fibers promote endothelial cell guidance. *Biofabrication* **7**, 015001 (2014).
31. Caggiano, L. R., Lee, J.-J. & Holmes, J. W. Surgical reinforcement alters collagen alignment and turnover in healing myocardial infarcts. *Am. J. Physiol.-Heart Circ. Physiol.* **315**, H1041–H1050 (2018).
32. Fomovsky Gregory M., Clark Samantha A., Parker Katherine M., Ailawadi Gorav & Holmes Jeffrey W. Anisotropic Reinforcement of Acute Anteroapical Infarcts Improves Pump Function. *Circ. Heart Fail.* **5**, 515–522 (2012).

CHAPTER 6: DISCUSSION

10.1 Overview

As the leading cause of death in the world, IHD is a healthcare challenge with global impact. Cardiac ischemia causes rapid cell and tissue death that, due to the heart's own inability to regenerate and the lack of currently available restorative treatment, permanently reduces heart function, leading to decreased quality of life for affected patients[1–4]. Leveraging recent advances in hiPSC biology, engineered cardiac tissue therapies offer great potential as curative treatments, restoring lost function by replacing damaged tissue with healthy tissue. However, conventional approaches produce engineered cardiac tissue that fails to emulate the native cardiac microenvironment and that generates contractile forces much smaller than those produced by native adult tissue. We hypothesized that improved emulation of the anisotropic mechanical microenvironment of native myocardium via embedded collagen microfiber geometries would result in improved cardiac tissue function, leading us to develop a tunable collagen microfiber platform for engineered cardiac tissue.

This thesis work describes the research, design, development, and optimization of a platform for creating engineered cardiac tissues with customizable embedded collagen microfiber meshes. In Aim 1, I first characterized the relationship between scaffold components and cell population factors in simple blended collagen and fibrin cardiac tissues and identified cardiac tissue fabrication parameters that yielded the most desirable results in terms of tissue stiffness, contractile force, and twitch kinetics. In Aim 2, I designed, developed, and characterized an automated process for the fabrication of collagen microfiber meshes with tunable designs, as well as a process for embedding these meshes in a cellularized hydrogel bulk (based on our prior experiments), thereby creating a tunable composite material platform compatible with use as a tissue scaffold. Finally, in Aim 3, I created engineered cardiac tissues using this novel platform and characterized the performance of these tissues in vitro, as well as the immune response and degradation in the cardiac environment in an in vivo pilot study.

10.2 Major Results and Conclusions

10.2.1 Specific Aim 1: *Identify optimal conditions for creating engineered cardiac tissues in a simple hydrogel format by characterizing the impact of scaffold composition and cell population on tissue development and function*

Acknowledging the diversity of hydrogel scaffold compositions that have been cited in the cardiac tissue engineering literature[5–11], we aimed to not only identify a scaffold composition that yielded the most desirable engineered cardiac tissues in terms of tensile stiffness and active force production from our iPSC-derived cardiomyocyte source, but to also understand how both scaffold parameters and cell population parameters impacted these outcomes. We hypothesized that both hydrogel composition (due to adhesion site availability, remodeling characteristics, and stiffness) and cell population (due to protease production, focal adhesion development, and cell number) would influence tissue development and function. To evaluate this hypothesis, we first studied how five factors related to the fabrication of blended collagen and fibrin hydrogels (collagen concentration, fibrin concentration, aprotinin concentration, time in culture, and temperature during polymerization) influenced the stiffness properties of these materials. In contrast to similar studies, we considered both the tensile and compressive stiffness of these materials as native myocardium experiences both tensile and compressive forces in vivo. Evaluation of acellular hydrogels revealed that hydrogels within this design space could exceed the compressive stiffness values of native adult rat myocardium (3.73±0.91 kPa for the stiffest acellular blended hydrogel group vs. 2.67±0.61 kPa for native myocardium), but did not approach native tensile stiffness values (3.48±0.33 kPa in the stiffest acellular blended hydrogel group vs. 16.58±1.85 kPa and 30.80±2.71 kPa in the transverse and longitudinal directions for native myocardium, respectively). Importantly, aprotinin concentration was found to have no significant impact on hydrogel stiffness, and collagen and fibrin were identified as primary contributors to both compressive and tensile stiffness.

The role of collagen and fibrin in cardiac tissue development were then evaluated in concert with seeding density (a parameter related to cell number) as well as cell purity (which was incorporated through repeated experimental trials with different batches of iPSC-CMs with purity identified via FACs analysis) in a three level RSM experiment. Three trials were performed with independent unpurified cardiomyocyte populations, each prepared as 42 individual constructs, and a statistically significant, unifying model was identified. Increased tissue compaction (a precursor to functional tissue development) was associated with high fibrin concentrations and initial seeding density, while increased collagen concentration was associated with decreased compaction. Cell purity was found to increase compaction up to a point (40% - 50% cTnT$^+$), but decreased compaction was associated with higher purity cardiomyocytes (60.2% cTnT$^+$). This result aligns with a recent study by Zimmerman and colleagues, which evaluated fibroblast doping into seeding populations of purified cardiomyocytes, and found optimal tissue function with a 40-75% cardiomyocyte population[12]. However, only two of the 39 groups prepared in this experiment generated contractile forces (both groups were prepared with high purity cardiomyocytes and low fibrin concentration), demonstrating that compaction was not the only critical factor in syncytium formation.

To further investigate the role of these scaffold and cell parameters in yielding actively contractile engineered cardiac tissues, a fourth trial was conducted with lactate purified cardiomyocytes with a purity of 75.5% cTnT$^+$. In this final trial, 9 of the 13 groups evaluated yielded beating constructs. Interestingly, in this final trial, increased fibrin concentrations were associated with decreased compaction, peak twitch stress (an active contractile force metric), and passive stiffness. Increased collagen concentrations were associated with decreased compaction and peak twitch stress, but increased Young's modulus, while increased seeding densities were associated with increased compaction, peak twitch stress, and passive stiffness. Of the groups empirically evaluated, the greatest active force production (0.544±0.142 kPa) and passive stiffness values (21.79±5.64 kPa) were observed in the groups prepared with 1.2 mg/mL collagen, no fibrin, and 15e6 cells/mL. Notably, this formulation approximates the collagen concentration reported by Zimmerman and Murry (1.25 mg/mL and 0.8 to 1.2 mg/mL, respectively), but recommends a seeding density falling between what was utilized by these groups (3e6 cells/mL and 20e6 cells/mL)[8,10]. However, it is likely that cell source, cell line, and other factors have a substantial impact on tissue development and function, so greater value to the broader field likely lies in the observed trends rather than absolute values.

The RSM statistical model generated from this trial predicted even greater peak twitch stress values from constructs prepared with 0.8 mg/mL collagen, no fibrin, and 15e6 cells/mL. However, constructs prepared with this composition failed due to necking and breaking caused by actomyosin cytoskeletal forces that exceed the stiffness of the surrounding matrix, before the 6 day timepoint – a practical limitation beyond the predictive capabilities of the RSM model[13].

In conclusion for Aim 1, we succeeded in generating statistical models that describe the role of both blended collagen and fibrin hydrogel scaffolds and iPSC-CM populations in *engineered cardiac tissue development (as evaluated by tissue compaction) and function (as evaluated by active force generation and passive stiffness). Cell purity, collagen concentration, and fibrin concentration were found to predominate tissue compaction in unpurified cardiomyocyte populations, with increased compaction associated with increased fibrin concentrations and cell purity, and decreased compaction associated with collagen concentration. However, active contractile force generation was found to occur only rarely in low purity cardiomyocyte populations. In high purity cardiomyocyte populations, fibrin was found to have an inverted role, resulting in decreased compaction and compromising tissue contractile function. The greatest active force production and passive stiffness was achieved with high purity cardiomyocytes (≥60%) in 1.2 mg/mL collagen with 15e6 cells/mL.*

10.2.2 **Specific Aim 2:** ***Design, fabricate, and characterize a device and process capable of producing collagen microfiber meshes, embedded in a collagen hydrogel bulk, that demonstrate anisotropic mechanical properties and are compatible with tissue culture***

Conventional engineered cardiac tissues deviate substantially from the native myocardial mechanical niche through the utilization of simple, isotropic hydrogel scaffold materials with acellular stiffnesses on the order of 0.5 – 2.0 kPa[5–10]. Conversely, native myocardium is known to exhibit significant mechanical anisotropy with stiffness in the long fiber direction on the order of 10 – 100 kPa[14–18] and an anisotropic ratio between 1.4 and 2.0[14,18,19]. Given the important role of the mechanical microenvironment in defining cell phenotype[16,20–22], cell alignment[23–26], and even differentiation pathway[27,28], recent approaches have attempted to create anisotropic tissues by leveraging stresses exerted by resident cells to create aligned stress fields and incorporating fenestrations[17,26,29,30]. However, these approaches impart restrictions on tissue geometry and reduce tissue density with the presence of fenestrations, adding an obstacle to the development of a functional cardiac tissue patch with physiologically relevant contractile function.

With the goal of improving the physiological relevance of the scaffold platform that we use for our engineered cardiac tissues and advancing the scaffold options available to tissue engineers, we leveraged what we discovered about simple hydrogel scaffolds for cardiac tissues in the development of a scaffold platform with tunable mechanical anisotropy. We hypothesized that emulating the mechanical anisotropy that defines native myocardium via an embedded mesh material may improve the alignment and phenotype of resident cardiomyocytes in our engineered tissues without requiring compromise on tissue shape. In order to evaluate this hypothesis and study the relationship between anisotropic mechanical cues and cardiac tissue function and development, we first needed to develop the technology to create such a scaffold material. Collagen microfibers prepared via wet spinning presented desirable characteristics for this approach including small fiber diameters (≤100 μm), relatively high stiffness values (>1 MPa), good cell adhesion and remodeling properties, and known degradation pathways[31–33].

We designed and fabricated a device consisting of a rotating and translating collection mandrel capable of organizing wet spun fibers into defined patterns during mesh collection. The device was driven by two stepper motors (one controlling mandrel rotation and the other translation using two timing belt pulley systems), both of which were driven by an Arduino microcontroller with a motor controller and LCD user interface. Importantly, the device was designed to utilize laser-cut and off-the-shelf parts whenever possible in order to minimize costs and maximize potential utility by other research groups. In addition, software tools were developed to allow for the convenient design of mesh patterns and the translation of these patterns into a format compatible with fabrication via the Arduino microcontroller. The collagen microfiber wet spinning process itself was also refined and optimized to improve compatibility with the automated fabrication process and to reduce or eliminate failure modes during collection. To permit collection and embedding of fabricated meshes in engineered tissues, an autoclavable capture system consisting of stainless-steel frames and screws, PDMS gaskets and plugs, alignment jigs, and a related tissue fabrication process were similarly developed.

To evaluate the mechanical properties of the wet spun collagen microfibers, a critical property for the intended application of mechanical signaling in engineered tissues, individual collagen microfibers were evaluated after 0 to 96 hours of incubation in PBS at 37°C. Fibers produced using this process exhibited tensile stiffness values of 1.51±0.11 MPa after 96 hours of incubation, significantly greater than the tensile stiffness values observed in the acellular collagen and fibrin hydrogels evaluated in aim 1 ($\leq$ 3.48±0.33 kPa). Strain at break values for these fibers after 96 hours of incubation was 37.70±1.85%, exceeding the maximum physiological strain values experienced by native myocardium (<25% in adults[34] and children[35]). Importantly, tensile stiffness, strain at break, and ultimate tensile stress values all increased over time in culture, providing evidence of collagen self-assembly. SBF and TEM imaging provided further evidence for collagen self-assembly (an indicator of molecular collagen integrity) in the form of fibril development and characteristics D-banding after time in culture conditions. Finally, DSC analysis confirmed denaturation temperatures in wet-spun collagen fibers consistent with unprocessed collagen stock and values reported in the literature for unadulterated collagen[36]. Together, this data indicates that the collagen in the collagen microfiber has not been significantly denatured by the wet spinning and collection process, and therefore is likely to retain the desirable characteristics of native collagen.

To characterize the resolution and fidelity limitations of the collection device, a series of parallel fiber patterns with known fiber spacing were prepared and analyzed. Image analysis of these meshes showed decreasing variability associated with increased fiber spacing. Patterns targeting 100, 200, and 400 μm spacing yielded actual fiber spacing of 77.49±63.80 μm, 181.0±122.7 μm, and 369.2±55.16 μm (mean ± standard deviation), respectively. Much of this variability is attributed to static attraction between adjacent fibers causing fiber displacement during collection. Similar analysis of overlapping fiber angle showed low variability both among the four meshes generated in a single batch, as well as across three batches (29.93±2.07, 30.53±2.32, and 30.35±2.60 degrees with a 30° angle target).

Mechanical analysis of acellular composites prepared with 30° and 60° fiber angles in both long and transverse fiber orientations exhibited statistically significant anisotropic stiffness values (4.92±1.09 kPa vs. 22.28±2.50 kPa for the 30° constructs and 6.85±0.93 kPa vs. 11.40±0.48 kPa for the 60° constructs), yielding anisotropic ratios of 4.5 and 1.7 for the two designs, respectively. The 60° design therefore approaches the values for native myocardium anisotropic stiffness reported in the literature of 1.4 – 2.0[14,18,19]. The viability of these composite materials as tissue scaffolds was verified by fluorescent live/dead stain and confocal imaging, which showed very few detectable dead cells, as well as immunohistochemistry which confirmed the presence of α-actinin in organized bands – a marker of cardiomyocytes.

In conclusion for Aim 2, we designed and built a system capable of preparing collagen microfibers from a high concentration collagen stock and organized these fibers into meshes based on prescribed patterns prepared digitally. This system produced meshes with fiber spacing parameters as small as 100 μm, though placement precision increased up to 400 μm spacing due to static forces exerted by the fibers on their neighbors. Overlapping fiber angles were consistent *within ± 1°, even between wet spinning batches. Embedded mesh composite materials prepared with this method exhibited statistically significant stiffness anisotropy, and 60° mesh composites exhibited anisotropic properties comparable to native myocardium. These composites were demonstrated to be viable tissue culture platforms in terms of maintaining both cell viability as well as the phenotype of resident cardiomyocytes.*

10.2.3 **Specific Aim 3: *Evaluate the performance of engineered cardiac tissues prepared with anisotropic composite scaffolds* in vitro *and* in vivo.**

The conventional cardiac tissue engineering paradigm of cardiomyocytes seeded in a homogenous hydrogel bulk offers limited control over microenvironmental mechanical signals that can induce alignment and modulate tissue development and function[28,37–39], as well as limited parity with the mechanics of native tissue. Alternative approaches that address anisotropy impose restrictions on tissue shape, limiting the utility of these platforms for the development of therapeutic cardiac tissue patches[10,17,26,30]. To address this need with respect to the broader tissue engineering field, we previously developed and characterized an automated system and complementary process for preparing collagen microfiber meshes and embedding these meshes in a hydrogel bulk seeded with cells. The final step in the development of our platform for engineered cardiac tissues with tunable anisotropy was the characterization of composite cardiac tissues in vitro and in vivo in order to evaluate the impact that our embedded collagen microfibers fiber format has on cardiac tissue development and function.

To maximize the anisotropic signal provided by the embedded collagen microfibers, we selected parallel and 30° fiber angle meshes for characterization in comparison to conventionally prepared engineered cardiac tissues without fibers. Based on our early experiments that highlighted the impact of collagen concentration and hydrogel stiffness on tissue development and compaction, we chose to evaluate all three of these tissue formats with both 0.8 mg/mL and 1.2 mg/mL collagen[14]. In all cases, tissues were seeded with 15e6 hiPSC-CMs/mL, a parameter also based on our previous optimization work.

We observed that the greatest impact on construct development and function was effected through the modulation of the tissue compaction process, with significant differences in final construct size between the three design groups. This process, through which resident cells remodeling their surrounding microenvironment, is known to be integral to the development of functional cardiac tissues in vitro, but achieving consistent results continues to pose a challenge to tissue engineering researchers[13,40,41]. Within this study, low collagen concentration (0.8 mg/mL) fiber-free constructs failed due to uncontrolled compaction, while fibrous constructs prepared with the same hydrogel and cell composition did not, suggesting practical utility in constructs with embedded microfibers. Interestingly, the boundary conditions of the collagen microfibers appeared to play a major role in tissue compaction, which may have utility in directing the shape of compacted tissue constructs.

Poorly compacted tissues prepared with 30° angle fibers exhibited poor cardiomyocyte phenotype and maturity compared to the positive cardiomyocyte markers observed in the more compact fiber-free and parallel fiber groups. This result was attributed to the effectively lower cardiomyocyte density in the uncompacted constructs resulting in decreased cell-cell signaling and syncytium development, a phenomena our group has studied previously[14]. In spite of these differences in compaction, no significant difference was found between groups in terms of passive stiffness, likely due to the increased compaction found in the fiber-free tissues and decreased compaction found in the fiber-dense 30° angle composite tissues.

Active force analysis also found no significant difference across the sample groups, though there did appear to be a nominal positive trend with the parallel fiber constructs due to a small number of highly contractile tissues. This result merits both further investigation of collagen microfiber composites for creating engineered tissues, as well as the sources of variability that cause such unstable results in the fibrous format. One approach would be to evaluate parallel fiber mesh designs with increased fiber spacing, which would serve to both decrease variability in fiber placement (as shown previously[42]), and to reduce compaction load in the tissue.

Finally, parallel and 30° fiber constructs were evaluated in a rat model of myocardial infarction. Stained heart sections harvested at the two-week timepoint showed dark collagen staining with dimensions similar to those of the embedded wet spun collagen microfibers, suggesting minimal degradation at this early timepoint. While further studies are needed to assess fiber degradation in this environment at later timepoints, this result serves as an early positive indicator for the potential use of collagen microfibers as a therapeutic tool for cardiac applications. Passive anisotropic mechanical reinforcement of the heart following an ischemic event has been shown to improve heart function[43], and persistent microfibers may also have utility as a vehicle for a therapeutic cell or drug delivery.

In conclusion for Aim 3, we characterized parallel and 30° fiber angle constructs in vitro, evaluating tissue compaction and immunohistochemical markers of cardiac maturity as developmental outputs, and passive and active mechanical properties as functional outputs. Embedded collagen microfibers demonstrated a clear impact on these developmental tissue responses, modulating both tissue compaction and cardiomyocyte maturity. Passive mechanical analysis showed that both composite designs and 1.2 mg/mL fiber-free tissues all approached the *tensile stiffness of native myocardium in the long fiber orientation after 10 days in culture conditions. While no significant differences were found in terms of active mechanics, the individual constructs that performed best overall were prepared with parallel collagen microfibers, justifying further investigation into both the functional properties of these tissues as well as the sources of variability. Embedded collagen microfibers persisted on the surface of the rat heart at the two-week timepoint, demonstrating potential utility as therapeutic tool.*

10.3 Future Directions

The goal of this thesis work was to develop a scaffold platform for engineered cardiac tissue development with tunable anisotropic mechanical properties in order to emulate the anisotropic properties of native myocardium and to understand the influence that scaffold anisotropy has on cardiac tissue development and functional metrics of tissue performance. The work presented herein accomplishes these goals of both developing the tools and processes necessary to fabricate a mechanically anisotropic engineered cardiac tissue, as well as the evaluation of functional performance metrics associated with this scaffold platform both in vitro and in vivo. However, this work represents only a fraction of what could ultimately be explored with this tool. The mesh designs utilized in this work were selected to maximize differences between test groups in order to understand how general mesh characteristics influenced cardiac tissue development and performance, and it is likely that other designs could be fabricated to achieve increased physiological relevance or better engineered tissue performance. Similarly, small tissue dimensions were chosen for these evaluation studies to increase the number of groups and samples that could be evaluated given resource limitations with respect to scaffold components and cardiomyocyte production. However, the technology described herein is compatible with much larger construct dimensions (up to 4 cm x 4 cm without mandrel modification), which offers utility for the evaluation of tissues that would be appropriately sized for a human or large animal heart. Finally, modification of the collagen microfibers may enable the release of signaling factors, either for the benefit of the tissue in vitro or for a therapeutic benefit for the patient in vivo.

10.3.1 Alternative Mesh Designs

The 30° angle and parallel fiber mesh designs constructs were selected for in vitro and in vivo evaluation in order to have clear differentiation between test groups and to evaluate any difference in functional metrics of tissue performance associated with fully aligned fibers vs. angled overlapping fibers. However, the mesh design and automated fabrication technique described herein is capable of producing far more sophisticated designs which may either improve the function of engineered cardiac tissues prepared using this format or may have utility as in replicating the anisotropic or structural characteristic of tissues other than myocardium.

Computational modeling offers a convenient approach to understand quantitatively how design parameters (such as fiber angle, fiber spacing, and fiber diameter) contribute to the effective mechanical properties of the composite. Other mesh parameters, such as alternating spacing parameters between adjacent fibers and tri-directional fiber layers could also be considered (Fig A2.9). This type of model could be used to define a design space for targeted composite mechanical properties, such as anisotropic ratio or stiffness. Alternatively, a DOE approach could be used to empirically evaluate how these same mesh parameters influence tissue compaction and syncytium development - phenomena that may be too complex for constitutive models. This kind of evaluation may lead to mesh designs that yield desirable characteristics in an engineered tissue format but would otherwise not have been considered. Applying both of these approaches in concert would enable informed selection of the DOE experiment space, supported by empirical data collection.

Meshes intended to emulate the extracellular matrix structure and mechanical properties of tendon and valve leaflets have already been fabricated in order to demonstrate the versatility of the fabrication platform (Fig A2.9). However, these meshes have not yet been seeded with cells and cultured in order to evaluate the performance of these composite scaffold tissues in comparison to those prepared with other scaffold technologies. It is possible that tissue engineering and biomaterials applications beyond the scope of cardiac tissue engineered would also benefit from the utility of this composite scaffold material.

10.3.2 Macroscale Meshes

An important advantage of the embedded mechanotransductive guidance cues associated with this collagen microfiber scaffold platform is that tissues of any size can be made (respecting thickness limitations associated with nutrient diffusion into avascular engineered tissues), while avoiding the need for performance-impeding fenestrations. Without any modification, the process described herein could be used to prepare macroscale meshes (>2 cm x 2 cm) appropriate for therapeutic use on either a large animal or human heart. While cardiac tissue engineering is likely still many years away from the first studies in humans, this format enables early in vitro and large animal evaluation of functional cardiac tissue metric that are expected to be dependent on graft size, including electrical conductivity, absolute contractile force generation, and graft uniformity. Utilizing a such a scaffold fabrication system with intrinsic scalability for early in vitro and in vivo characterization also mitigates risks and challenges that would be associated with the scale-up of other scaffold modalities that require manual manipulation (such as suture placement) or are more sensitive to environmental factors (such as humidity and air flow)[44–46].

10.3.3 Drug Release

While the collagen microfibers embedded in composite tissues have been demonstrated to improve the passive mechanical properties and interact positively with resident cell populations, they may be able to serve a secondary purpose through the controlled release of growth and signaling factors that would improve tissue function. Collagen hydrogels have been studied in the past as small molecule and protein drug release vectors, and have shown significant promise due to their biocompatibility and tunable degree of crosslinking and pore size[47–49]. The relatively high concentration of the collagen microfibers described in this system may make them particularly well suited for this application. Other approaches for drug release from collagen hydrogels have utilized liposomes sequestered in the collagen matrix to slow drug release[50,51] or have embedded drug loaded alginate microspheres inside a collagen hydrogel to further modulate drug release kinetics[52], a strategy that could easily be employed with the described wet spun collagen microfiber format.

Embedded collagen microfibers could be loaded with angiogenic growth factors, such as VEGF, FGF, and/or TGFβ, to encourage vascularization necessary for graft survival following implant. Alternatively, fibers loaded with factors that encourage cardiac phenotype or maturity, such as IGF1 and NRG1 may promote tissue function in vitro and in vivo[6]. Finally, drug loaded fibers may also have utility as in vitro models, enabling the preparation of cell culture systems with the 3D patterned cytokine or chemotactic factor gradients, which are known to play a important roles in tissue biology[53]. Such systems have been used to study tumor metastasis[54], create tissue engineered cartilage[55], and the differentiation of neural progenitor cells[56], among other applications.

10.4 Final Conclusions and Broader Impact

This thesis describes a comprehensive approach to the development, implementation, and evaluation of a novel scaffold platform for engineered cardiac tissues. First, a robust design of experiments approach was used to understand which parameters of blended collagen and fibrin hydrogels influence both compressive and tensile stiffness. The blended acellular hydrogels were shown to have compressive stiffness values that approximated those of native myocardium, but tensile stiffness values that deviated greatly from native myocardium. Once critical parameters that influence stiffness were identified, these factors (collagen concentration and fibrin concentration) were further investigated along with cellularized scaffold parameters (seeding density and cell purity) in order to define the relationship between these factors and their impact on tissue development and functional cardiac tissue metrics (active and passive contractile force). Optimal conditions were identified for the production of engineered cardiac tissues from iPSC-derived CMs.

Next, a process was developed to create engineered cardiac tissues with embedded collagen microfiber meshes with custom geometry, enabling the fabrication of cardiac tissues with tunable anisotropy. To support this process, an automated collection device was designed, fabricated, and characterized. Products of the process itself were also characterized to confirm the integrity of the collagen in the microfibers, define the mechanical properties of both individual fibers as well as mesh composites, and evaluate the suitability of the composites as scaffolds for engineered cardiac tissues. The collagen microfibers were shown to maintain chemical and physical markers of collagen integrity following the wet spinning process, and were also found to possess mechanical properties that made them well suited for the composite scaffold application. Acellular 30 degree and 60 degree composite materials were shown to exhibit mechanical anisotropy, and cardiomyocyte-seeded composites confirmed cell viability, tissue development, and maintenance of the cardiomyocyte phenotype with the scaffold platform.

Finally, composite tissues prepared with the anisotropic scaffold platform were evaluated both in vitro and in vivo. Embedded collagen microfibers were shown to impact cardiac tissue development by modulating compaction, a key factor in tissue development. Histological evaluation of in vitro constructs confirmed the critical role of tissue compaction on tissue development based on markers of cardiomyocyte maturity. Passive mechanical analysis of fiber-free and composite tissues showed no difference in stiffness, emphasizing the major role resident cells play in modulating tissue mechanical properties. Active analysis of all tissue groups also showed no difference in force production, though the individual tissues that produced the greatest forces were prepared with aligned collagen microfibers, suggesting that there may be a positive force production response to aligned fibers that could be realized either by evaluating large samples sizes, or by mitigating the high degree of variability associated with the fiber constructs. In vivo analysis in a rat model of myocardial infraction demonstrated the persistence of embedded collagen microfibers on the surface of the rat heart at the two week timepoint, demonstrating a the potential of these fibers as a persistent therapeutic platform in the cardiac context.

Beyond the cardiac tissue engineering application considered herein, the embedded collagen microfiber platform may have more immediate utility in other therapeutic applications. Acellular mesh materials are used presently in broad array of surgical applications, including hernia repair and breast reconstruction, and bioactive materials are desirable for these indications due to their ability to promote tissue ingrowth compared to synthetics, which improves patient comfort and reduces the risk of harboring latent infections[57–59]. The impressive mechanical properties of the collagen microfibers described herein, with the potential to further increase these properties via crosslinking may be especially well suited for these applications, which currently rely on donor tissue that is both challenging to source and highly variable[60,61]. Collagen microfibers composites in this application would have the competitive advantage of readily available source materials, tunable mechanical properties, and a clear pathway to GMP production and FDA regulatory approval based on other collagen based products that are already commercially available[62,63].

In the longer term, the method described herein may be further refined to provide more precise control over tissue development and thereby provide utility for the field of tissue engineering as a whole. The iterative process of materials technology development has in recent years led to hollow electrospun fibers[64,65], nanoscale 3D printing[66,67], and hydrogels with precisely controlled micropatterned pores[68], all of which have diverse applications for tissue engineering research and beyond and were not possible only a decade ago. Therefore, the work presented here is most fully utilized not just for its immediate potential research and therapeutic applications, but also as an intermediary for what is to come.

10.5 References

1. Chilton, R. J. Pathophysiology of Coronary Heart Disease: A Brief Review. *J. Am. Osteopath. Assoc.* **104**, 5S-8S (2004).
2. Moran, A. E. *et al.* Assessing the Global Burden of Ischemic Heart Disease. *Glob. Heart* **7**, 315–329 (2012).
3. Vaccarino, V. *et al.* Presentation, management, and outcomes of ischaemic heart disease in women. *Nat. Rev. Cardiol.* **10**, 508–518 (2013).

4. Moryś, J. M., Bellwon, J., Höfer, S., Rynkiewicz, A. & Gruchała, M. Quality of life in patients with coronary heart disease after myocardial infarction and with ischemic heart failure. *Arch. Med. Sci. AMS* **12**, 326–333 (2016).

5. Ye, K. Y., Sullivan, K. E. & Black, L. D. Encapsulation of Cardiomyocytes in a Fibrin Hydrogel for Cardiac Tissue Engineering. *J. Vis. Exp. JoVE* (2011). doi:10.3791/3251

6. Rupert, C. E. & Coulombe, K. L. K. IGF1 and NRG1 Enhance Proliferation, Metabolic Maturity, and the Force-Frequency Response in hESC-Derived Engineered Cardiac Tissues. *Stem Cells International* (2017). doi:10.1155/2017/7648409

7. Zimmermann, W.-H. *et al.* Tissue Engineering of a Differentiated Cardiac Muscle Construct. *Circ. Res.* **90**, 223–230 (2002).

8. Tulloch, N. L. *et al.* Growth of Engineered Human Myocardium with Mechanical Loading and Vascular Co-culture. *Circ. Res.* **109**, 47–59 (2011).

9. Tiburcy, M., Meyer, T., Soong, P. L. & Zimmermann, W.-H. Collagen-based engineered heart muscle. *Methods Mol. Biol. Clifton NJ* **1181**, 167–176 (2014).

10. Zimmermann, W.-H. *et al.* Engineered heart tissue grafts improve systolic and diastolic function in infarcted rat hearts. *Nat. Med.* **12**, 452–458 (2006).

11. Wendel, J. S., Ye, L., Zhang, P., Tranquillo, R. T. & Zhang, J. J. Functional Consequences of a Tissue-Engineered Myocardial Patch for Cardiac Repair in a Rat Infarct Model. *Tissue Eng. Part A* **20**, 1325–1335 (2014).

12. Tiburcy, M. *et al.* Defined Engineered Human Myocardium with Advanced Maturation for Applications in Heart Failure Modelling and Repair. *Circulation* **135**, 1832–1847 (2017).

13. Wang, H. *et al.* Necking and failure of constrained 3D microtissues induced by cellular tension. *Proc. Natl. Acad. Sci. U. S. A.* **110**, 20923–20928 (2013).

14. Kaiser, N. J., Kant, R. J., Minor, A. J. & Coulombe, K. L. Optimizing Blended Collagen-Fibrin Hydrogels for Cardiac Tissue Engineering with Human iPSC-derived Cardiomyocytes. *ACS Biomater. Sci. Eng.* (2018). doi:10.1021/acsbiomaterials.8b01112

15. Kaiser, N. J. & Coulombe, K. L. K. Physiologically inspired cardiac scaffolds for tailored in vivo function and heart regeneration. *Biomed. Mater.* **10**, 034003 (2015).

16. Jacot, J. G., Martin, J. C. & Hunt, D. L. Mechanobiology of Cardiomyocyte Development. *J. Biomech.* **43**, 93 (2010).

17. Engelmayr, G. C. *et al.* Accordion-like honeycombs for tissue engineering of cardiac anisotropy. *Nat. Mater.* **7**, 1003–1010 (2008).

18. Neal, R. A. *et al.* Three-Dimensional Elastomeric Scaffolds Designed with Cardiac-Mimetic Structural and Mechanical Features. *Tissue Eng. Part A* **19**, 793–807 (2013).

19. Park, H. *et al.* The Significance of Pore Microarchitecture in a Multi-Layered Elastomeric Scaffold for Contractile Cardiac Muscle Constructs. *Biomaterials* **32**, 1856–1864 (2011).

20. Boothe, S. D. *et al.* The Effect of Substrate Stiffness on Cardiomyocyte Action Potentials. *Cell Biochem. Biophys.* 1–9 (2016). doi:10.1007/s12013-016-0758-1

21. Bhana, B. *et al.* Influence of substrate stiffness on the phenotype of heart cells. *Biotechnol. Bioeng.* **105**, 1148–1160

22. Discher, D. E., Janmey, P. & Wang, Y. Tissue Cells Feel and Respond to the Stiffness of Their Substrate. *Science* **310**, 1139–1143 (2005).

23. Arora, A., Kothari, A. & Katti, D. S. Pore orientation mediated control of mechanical behavior of scaffolds and its application in cartilage-mimetic scaffold design. *J. Mech. Behav. Biomed. Mater.* doi:10.1016/j.jmbbm.2015.06.033

24. Kai, D., Prabhakaran, M. P., Jin, G. & Ramakrishna, S. Guided orientation of cardiomyocytes on electrospun aligned nanofibers for cardiac tissue engineering. *J. Biomed. Mater. Res. B Appl. Biomater.* **98B**, 379–386 (2011).

25. Aubin, H. *et al.* Directed 3D cell alignment and elongation in microengineered hydrogels. *Biomaterials* **31**, 6941–6951 (2010).

26. Bian, W., Jackman, C. P. & Bursac, N. Controlling the structural and functional anisotropy of engineered cardiac tissues. *Biofabrication* **6**, 024109 (2014).

27. Floren, M. *et al.* Human mesenchymal stem cells cultured on silk hydrogels with variable stiffness and growth factor differentiate into mature smooth muscle cell phenotype. *Acta Biomater.* doi:10.1016/j.actbio.2015.11.051

28. Bai, S. *et al.* Silk scaffolds with tunable mechanical capability for cell differentiation. *Acta Biomater.* doi:10.1016/j.actbio.2015.04.004

29. Naito, H. *et al.* Optimizing Engineered Heart Tissue for Therapeutic Applications as Surrogate Heart Muscle. *Circulation* **114**, I-72-I–78 (2006).

30. Munarin, F., Kaiser, N. J., Kim, T. Y., Choi, B.-R. & Coulombe, K. L. K. Laser-Etched Designs for Molding Hydrogel-Based Engineered Tissues. *Tissue Eng. Part C Methods* **23**, 311–321 (2017).

31. Caves, J. M. *et al.* Fibrillogenesis in Continuously Spun Synthetic Collagen Fiber. *J. Biomed. Mater. Res. B Appl. Biomater.* **93**, (2010).

32. Pins, G. D., Christiansen, D. L., Patel, R. & Silver, F. H. Self-assembly of collagen fibers. Influence of fibrillar alignment and decorin on mechanical properties. *Biophys. J.* **73**, 2164–2172 (1997).

33. Caves, J. M. *et al.* Elastin-like protein matrix reinforced with collagen microfibers for soft tissue repair. *Biomaterials* **32**, 5371–5379 (2011).

34. Yingchoncharoen, T., Agarwal, S., Popović, Z. B. & Marwick, T. H. Normal Ranges of Left Ventricular Strain: A Meta-Analysis. *J. Am. Soc. Echocardiogr.* **26**, 185–191 (2013).

35. Levy, P. T. *et al.* Reference Ranges of Left Ventricular Strain Measures by Two-Dimensional Speckle Tracking Echocardiography in Children: A Systematic Review and Meta-Analysis. *J. Am. Soc. Echocardiogr. Off. Publ. Am. Soc. Echocardiogr.* **29**, 209-225.e6 (2016).

36. Zeugolis, D. I. *et al.* Electro-spinning of pure collagen nano-fibres – Just an expensive way to make gelatin? *Biomaterials* **29**, 2293–2305 (2008).

37. Jacot, J. G., McCulloch, A. D. & Omens, J. H. Substrate Stiffness Affects the Functional Maturation of Neonatal Rat Ventricular Myocytes. *Biophys. J.* **95**, 3479–3487 (2008).

38. Bourget, J.-M., A., F., Germain, L., Guillemette, M. & Veres, T. Alignment of Cells and Extracellular Matrix Within Tissue- Engineered Substitutes. in *Advances in Biomaterials Science and Biomedical Applications* (ed. Pignatello, R.) (InTech, 2013).

39. Guilak, F., Butler, D. L., Goldstein, S. A. & Baaijens, F. P. T. Biomechanics and mechanobiology in functional tissue engineering. *J. Biomech.* **47**, 1933–1940 (2014).

40. Fernandez, P. & Bausch, A. R. The compaction of gels by cells: a case of collective mechanical activity. *Integr. Biol. Quant. Biosci. Nano Macro* **1**, 252–259 (2009).

41. van Vlimmeren, M. A. A., Driessen-Mol, A., Oomens, C. W. J. & Baaijens, F. P. T. An In Vitro Model System to Quantify Stress Generation, Compaction, and Retraction in Engineered Heart Valve Tissue. *Tissue Eng. Part C Methods* **17**, 983–991 (2011).

42. Kaiser, N. J., Bellows, J. A., Kant, R. J. & Coulombe, K. L. K. Digital Design and Automated Fabrication of Bespoke Collagen Microfiber Scaffolds. *Tissue Eng. Part C Methods* (In press).

43. Fomovsky Gregory M., Clark Samantha A., Parker Katherine M., Ailawadi Gorav & Holmes Jeffrey W. Anisotropic Reinforcement of Acute Anteroapical Infarcts Improves Pump Function. *Circ. Heart Fail.* **5**, 515–522 (2012).

44. Chrobak, M. O. *et al.* Design of a Fibrin Microthread-Based Composite Layer for Use in a Cardiac Patch. *ACS Biomater. Sci. Eng.* **3**, 1394–1403 (2017).

45. De Vrieze, S. *et al.* The effect of temperature and humidity on electrospinning. *J. Mater. Sci.* **44**, 1357 (2008).

46. Pelipenko, J., Kristl, J., Janković, B., Baumgartner, S. & Kocbek, P. The impact of relative humidity during electrospinning on the morphology and mechanical properties of nanofibers. *Int. J. Pharm.* **456**, 125–134 (2013).

47. Fujioka, K., Maeda, M., Hojo, T. & Sano, A. Protein release from collagen matrices. *Adv. Drug Deliv. Rev.* **31**, 247–266 (1998).

48. Friess, W. Collagen – biomaterial for drug delivery. *Eur. J. Pharm. Biopharm.* **45**, 113–136 (1998).

49. Radu, F. A., Bause, M., Knabner, P., Lee, G. W. & Friess, W. C. Modeling of Drug Release from Collagen Matrices. *J. Pharm. Sci.* **91**, 964–972 (2002).

50. Weiner, A. L., Carpenter-Green, S. S., Soehngen, E. C., Lenk, R. P. & Popescu, M. C. Liposome–Collagen Gel Matrix: A Novel Sustained Drug Delivery System. *J. Pharm. Sci.* **74**, 922–925 (1985).

51. Wang, G., Babadağli, M. E. & Uludağ, H. Bisphosphonate-Derivatized Liposomes to Control Drug Release from Collagen/Hydroxyapatite Scaffolds. *Mol. Pharm.* **8**, 1025–1034 (2011).

52. Liu, W., Griffith, M. & LI, F. Alginate microsphere-collagen composite hydrogel for ocular drug delivery and implantation. *J. Mater. Sci. Mater. Med.* **19**, 3365–3371 (2008).

53. Badylak, S. F. & Nerem, R. M. Progress in tissue engineering and regenerative medicine. *Proc. Natl. Acad. Sci.* **107**, 3285–3286 (2010).

54. Albritton, J. L. & Miller, J. S. 3D bioprinting: improving in vitro models of metastasis with heterogeneous tumor microenvironments. *Dis. Model. Mech.* **10**, 3–14 (2017).

55. Gadjanski, I. Recent advances on gradient hydrogels in biomimetic cartilage tissue engineering. *F1000Research* **6**, (2018).
56. Park, J. Y. *et al.* Differentiation of neural progenitor cells in a microfluidic chip-generated cytokine gradient. *Stem Cells Dayt. Ohio* **27**, 2646–2654 (2009).
57. Nafisi, N. *et al.* Application of Human Acellular Breast Dermal Matrix (ABDM) in Implant-Based Breast Reconstruction: An Experimental Study. *Aesthetic Plast. Surg.* **41**, 1435–1444 (2017).
58. Baylón, K. *et al.* Past, Present and Future of Surgical Meshes: A Review. *Membranes* **7**, (2017).
59. Elango, S., Perumalsamy, S., Ramachandran, K. & Vadodaria, K. Mesh materials and hernia repair. *BioMedicine* **7**,
60. Aamodt, J. M. & Grainger, D. W. Extracellular Matrix-based Biomaterial Scaffolds and the Host Response. *Biomaterials* **86**, 68–82 (2016).
61. Craft, R. O. *et al.* Does size matter? Technical considerations of a regenerative tissue matrix for use in reconstructive surgery. *Can. J. Plast. Surg. J. Can. Chir. Plast.* **19**, 51–52 (2011).
62. Zaulyanov, L. & Kirsner, R. S. A review of a bi-layered living cell treatment (Apligraf ®) in the treatment of venous leg ulcers and diabetic foot ulcers. *Clin. Interv. Aging* **2**, 93–98 (2007).
63. Kehoe, S., Zhang, X. F. & Boyd, D. FDA approved guidance conduits and wraps for peripheral nerve injury: A review of materials and efficacy. *Injury* **43**, 553–572 (2012).
64. Xue, J., Xie, J., Liu, W. & Xia, Y. Electrospun Nanofibers: New Concepts, Materials, and Applications. *Acc. Chem. Res.* **50**, 1976–1987 (2017).
65. Li, L. *et al.* Electrospun hollow nanofibers for advanced secondary batteries. *Nano Energy* **39**, 111–139 (2017).
66. Zhu, W. *et al.* 3D printing of functional biomaterials for tissue engineering. *Curr. Opin. Biotechnol.* **40**, 103–112 (2016).
67. Kankala, R. K. *et al.* Fabrication of arbitrary 3D components in cardiac surgery: from macro-, micro- to nanoscale. *Biofabrication* **9**, 032002 (2017).
68. Liu, S.-H., Zhang, H.-G., Li, S., Sun, C.-Y. & Hu, Q.-X. A Facile Strategy for Fabricating Tissue Engineering Scaffolds with Sophisticated Prevascularized Networks for Bulk Tissue Regeneration. *Macromol. Mater. Eng.* **0**, 1800642

APPENDIX 1: SUPPLEMENTAL ANALYSIS OF BLENDED COLLAGEN AND FIBRIN HYDROGELS

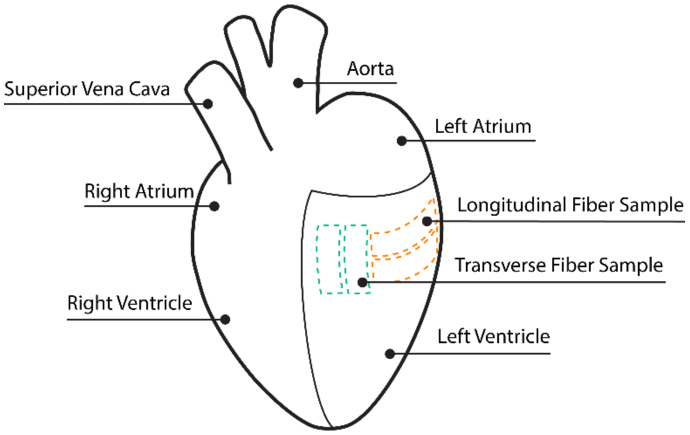

Figure A1. 1: Native rat myocardium sample collection. Longitudinal fiber samples approximately 2 mm x 10 mm (orange) were collected from the left ventricle myocardial layer with the long axis aligned with cardiac muscle fibers. Conversely, transverse fiber samples with the same dimensions (green) were collected from the left ventricle myocardial layer with the long axis perpendicular to cardiac muscle fibers.

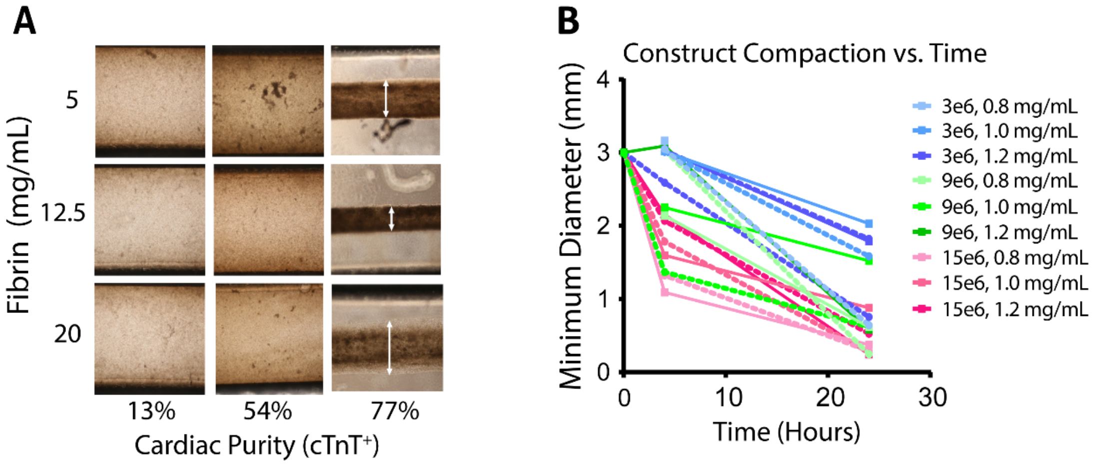

Figure A1. 2: Compaction of cellularized hydrogel constructs over time. (A) Phase microscopy images of blended 2 mg/mL collagen and fibrin hydrogels after 144 hours of incubation under cell culture conditions. Fibrin concentration is indicated on the y-axis, and cTnT$^+$ percentage (a measure of hiPSC-derived cardiomyocyte purity) is indicated on the x-axis. Double headed arrows indicate the construct midpoint diameter that was measured. No fibrinolytic inhibitor was used in this single experiment. (B) Scatterplot of collagen-only 49.71% cTnT$^+$ cardiac construct diameter at the narrowest point is shown through culture time. Replicates prepared under the same conditions are paired by color and have solid and dashed lines. The legend indicates cell seeding density per mL and collagen concentration.

Group	**Collagen (mg/mL)**	**Fibrin (mg/mL)**	**Seeding Density ($1x10^6$ cells/mL)**
1	0.8	0	12
2	0.8	4	9
3	0.8	8	12
4	1.2	0	9
5	1.2	4	12
6	1.2	8	9
7	1.6	0	12
8	1.6	4	9
9	1.6	8	12
10	0.8	4	15
11	1.2	0	15
12	1.2	8	15
13	1.6	4	15

Table A1. 1: Response surface model groups. Collagen, fibrin, and seeding density factor levels that defined each group. Note that group 5 was considered a center point for the Box-Behnken design format and was replicated across each of the two six well plates required for each experiment.

Experiment	**cTnT$^+$ (%)**	**SMA$^+$ (%)**	**cTnT$^+$ and SMA$^+$ (%)**	**SMA$^+$ only (%)**
Unpurified 1	60.24	25.94	18.74	7.20
Unpurified 2	24.4	51.17	8.11	43.06
Unpurified 3	30.23	18.31	9.41	8.90
Lactate Purified	75.5	54.1	51.1	3.00

Table A1. 2: Flow cytometry analysis of iPSC-derived cardiomyocytes.

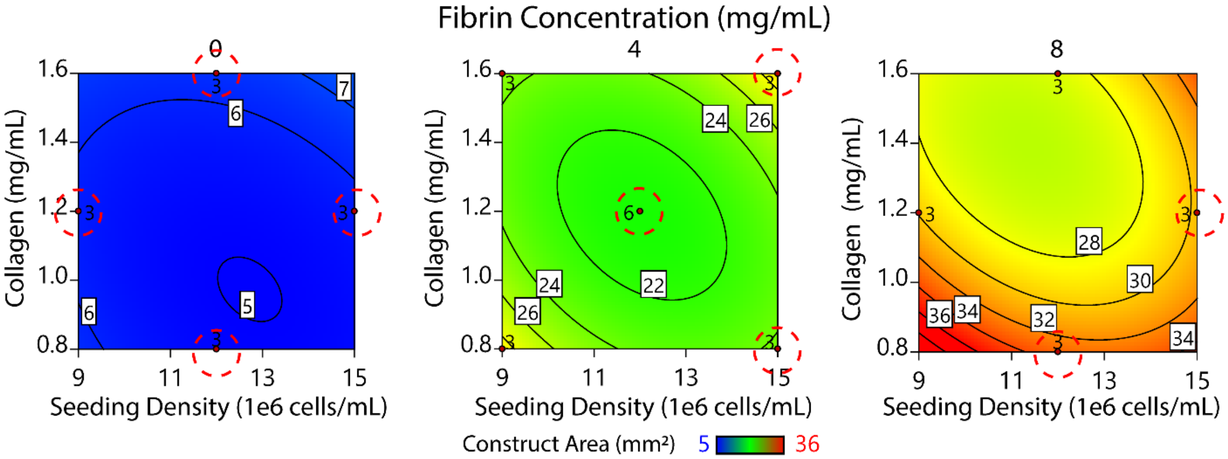

Figure A1. 3: Contour plots describing predicted construct compaction with lactate purified cardiomyocytes (75% cTnT$^+$) after 72 hours of culture with respect to fibrin concentration (major x-axis), collagen concentration (minor y-axes), and seeding density (minor x-axes). Contour labels indicate the predicted construct two-dimensional area in mm^2 after 72 hours of culture. Red dots and adjacent numbers indicate the number of empirical data replicates for a corresponding factor set, as prescribed by the Box-Behnken design. Red dashed circles indicate uniformly beating groups.

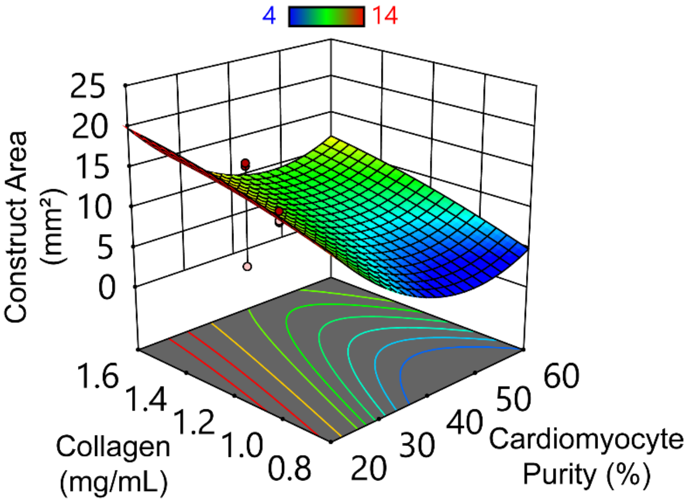

Figure A1. 4: Response surface model for unpurified construct compaction at 72 hours with 8 mg/mL fibrin. Red dots indicate experimental sample value greater than the model prediction and pink dots indicate experimental sample values less than the model prediction. Cardiomyocyte purity is a defined as the percentage of cTnT$^+$ cells.

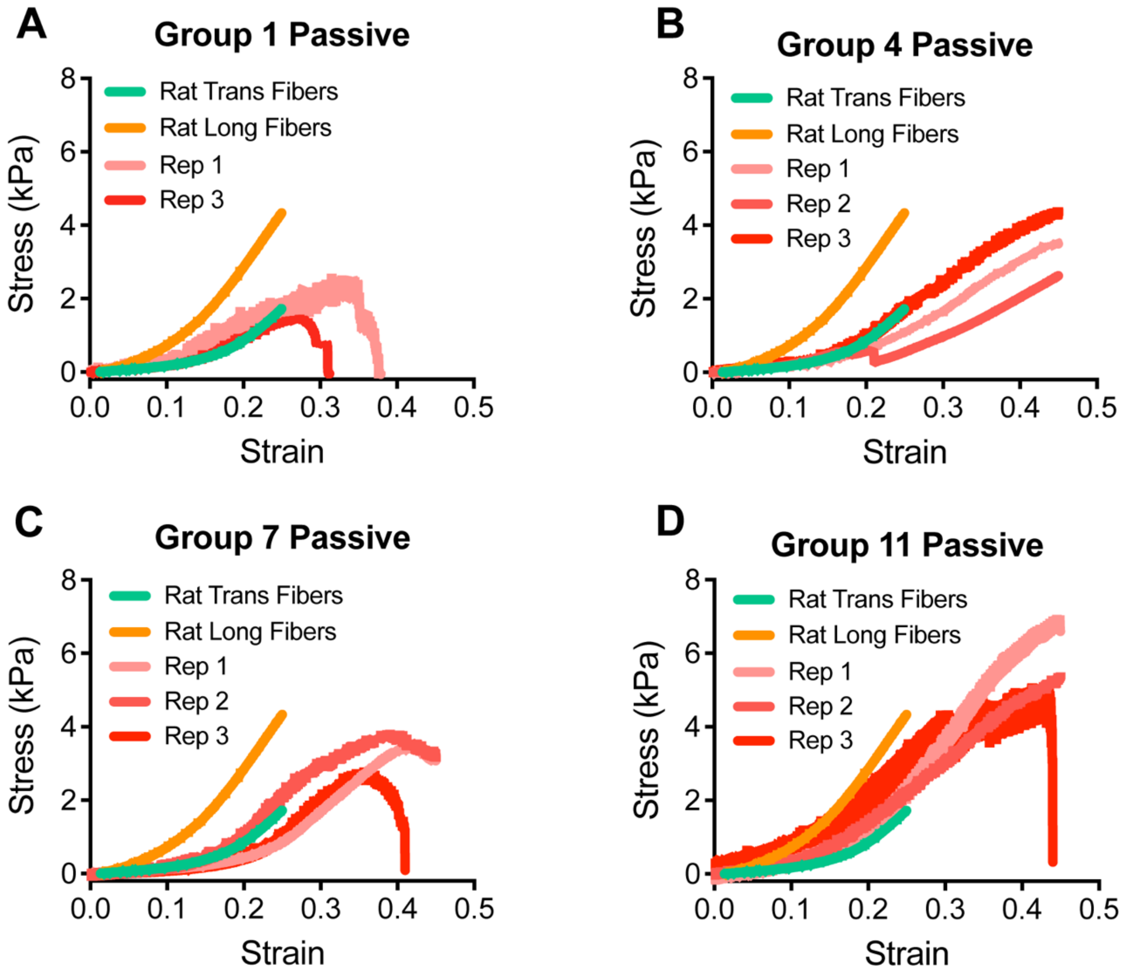

Figure A1. 5: Passive mechanical analysis of lactate purified constructs. Green and orange traces represent stress/strain curves of native rat myocardium in the transverse and longitudinal fiber orientations (replicated from Figure 2C), respectively. Red shaded traces represent individual samples from Group 1 (A), Group 4 (B), Group 7 (C), and Group 11 (D). Increased "thickness" of some traces is a result of autonomous construct beating. All native and engineered tissues were tested at a constant strain rate of 10% strain/min.

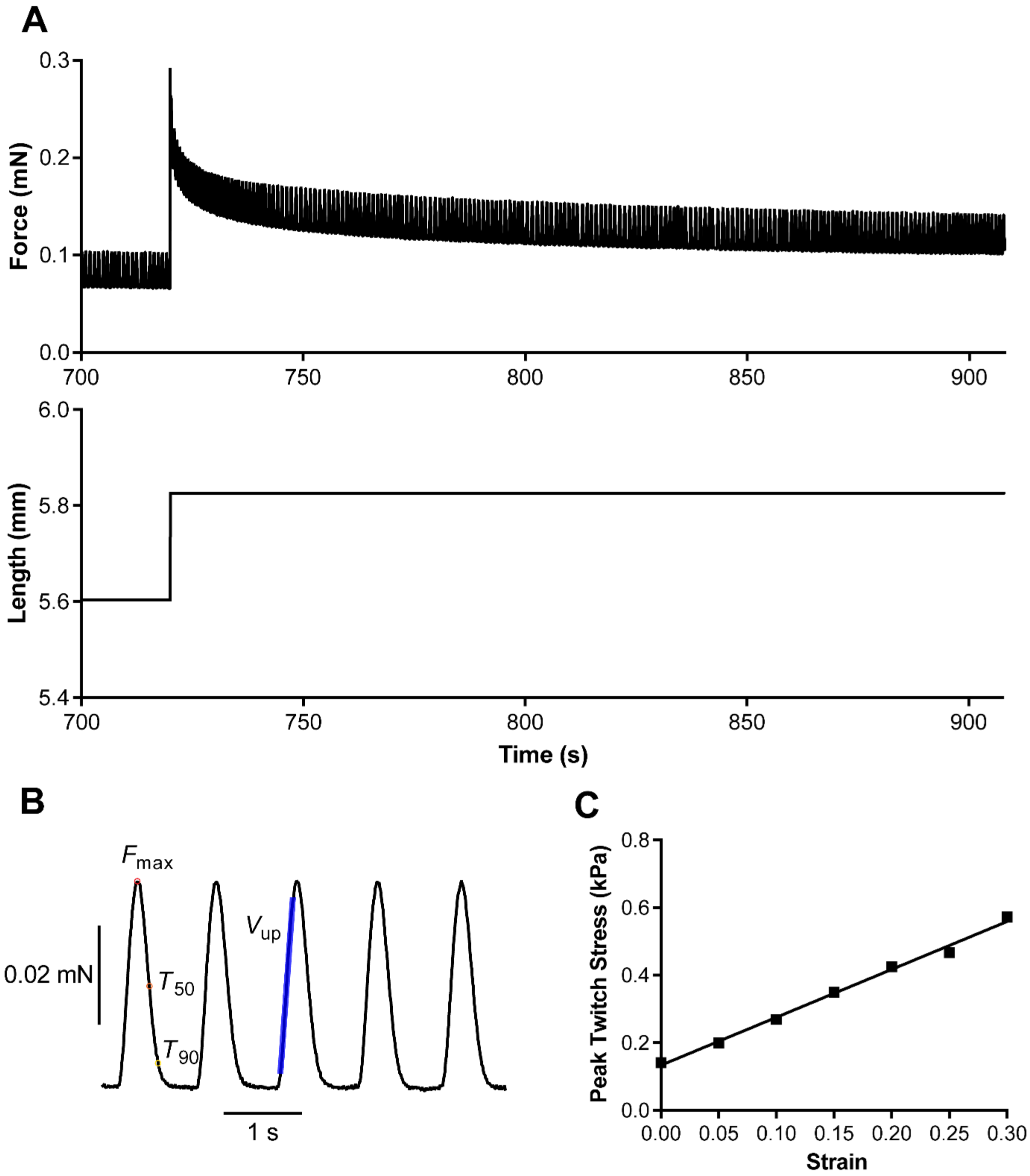

Figure A1. 6: Representative active mechanics analysis of lactate purified groups. (A) Raw force and length vs time traces at maximum strain (30%) during 1 Hz stimulation. (B) Active contraction raw data trace shows peak force (F_{max}), which is normalized to cross-sectional area to calculate stress, upstroke velocity (V_{up}), and points used to calculate relaxation time to 50% and 90% relaxation (T_{50} and T_{90}, respectively). Values are summarized in Table 3 at maximum (30%) strain. (C) Force-length relationship for one example tissue is shown as maximum twitch stress vs. strain at each of seven length positions ($R^2 = 0.99$).

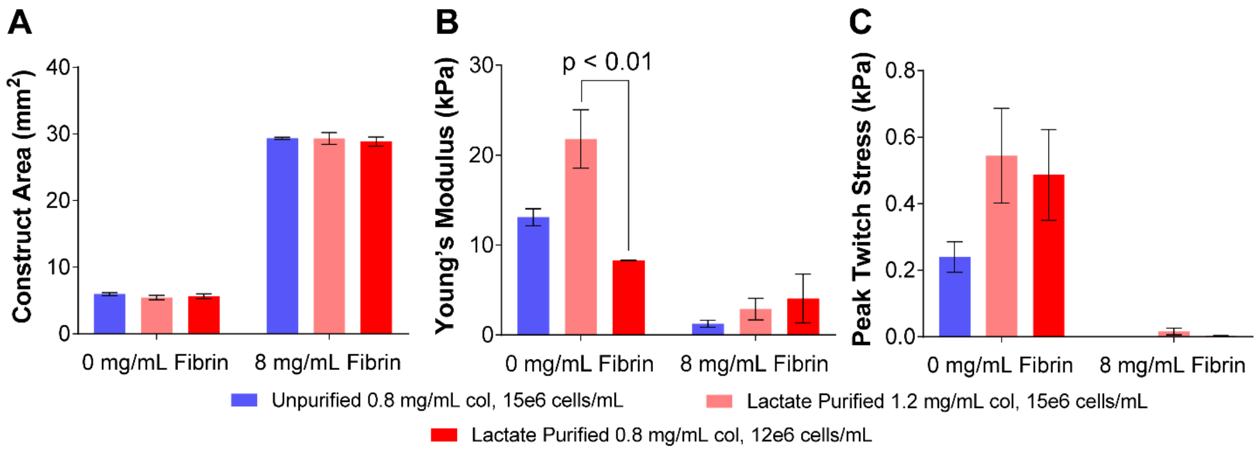

Figure A1. 7: Constructs prepared with high purity, unpurified iPSC-cardiomyocytes (84.6% cTnT$^+$) compared to select lactate purified cardiomyocyte (75.5% cTnT$^+$) groups. Lactate purified Group 1, Group 3, Group 11, and Group 12 are described above by formulation factor levels to facilitate comparison. (A) Construct area after 72 hours in culture conditions. (B) Young's modulus and (C) Peak stress after 6 days in culture conditions.

Source	Sum of squares	df	Mean Square	F-value	p-value	
Model	34.36	6	5.73	13.40	< 0.0001	significant
A-Fibrin	3.84	1	3.84	8.99	0.0046	
B-Collagen	1.57	1	1.57	3.67	0.0624	
D-Polymerization Temp	2.28	1	2.28	5.34	0.0260	
E-Time in Culture Conditions	19.15	1	19.15	44.80	< 0.0001	
AE	5.79	1	5.79	13.54	0.0007	
DE	1.73	1	1.73	4.05	0.0507	
Residual	17.52	41	0.4274			
Lack of Fit	2.96	9	0.3292	0.7234	0.6841	not significant
Pure Error	14.56	32	0.4550			
Cor Total	51.89	47				

Table A1. 3: Acellular compression model fit. df, degrees of freedom.

Factor	Coefficient Estimate	df	Standard Error	95% CI Low	95% CI High
Intercept	1.42	1	0.0944	1.23	1.61
A-Fibrin	0.2830	1	0.0944	0.0924	0.4735
B-Collagen	0.1808	1	0.0944	-0.0098	0.3714
D-Polymerization Temp	0.2180	1	0.0944	0.0275	0.4086
E-Time in Culture Conditions	0.6316	1	0.0944	0.4410	0.8222
AE	0.3472	1	0.0944	0.1567	0.5378
DE	0.1900	1	0.0944	-0.0006	0.3806

Table A1. 4: Acellular compression model coefficients.

Source	Sum of squares	df	Mean Square	F-value	p-value	
Model	863.75	14	61.70	9.69	< 0.0001	significant
A-Cell Number	29.85	1	29.85	4.69	0.0326	
B-Collagen Concentration	251.80	1	251.80	39.54	< 0.0001	
C-Fibrin Concentration	80.62	1	80.62	12.66	0.0006	
D-Cell Purity	320.60	1	320.60	50.34	< 0.0001	
AB	8.11	1	8.11	1.27	0.2616	
AC	5.10	1	5.10	0.8016	0.3726	
AD	25.60	1	25.60	4.02	0.0474	
BC	31.26	1	31.26	4.91	0.0288	
BD	1.20	1	1.20	0.1883	0.6652	
CD	1.79	1	1.79	0.2806	0.5974	
A^2	67.26	1	67.26	10.56	0.0015	
B^2	12.80	1	12.80	2.01	0.1591	
C^2	20.99	1	20.99	3.30	0.0722	
D^2	150.49	1	150.49	23.63	< 0.0001	
Residual	687.75	108	6.37			
Lack of Fit	150.06	24	6.25	0.9768	0.5041	not significant
Pure Error	537.68	84	6.40			
Cor Total	1551.49	122				

Table A1. 5: Unpurified 72 hour compaction model fit.

Factor	Coefficient Estimate	df	Standard Error	95% CI Low	95% CI High
Intercept	7.35	1	0.9650	5.43	9.26
A-Cell Number	-0.6576	1	0.3037	-1.26	-0.0556
B-Collagen Concentration	1.92	1	0.3051	1.31	2.52
C-Fibrin Concentration	-1.08	1	0.3049	-1.69	-0.4804
D-Cell Purity	-3.18	1	0.4478	-4.07	-2.29
AB	0.4820	1	0.4271	-0.3645	1.33
AC	-0.3825	1	0.4272	-1.23	0.4643
AD	-0.7637	1	0.3809	-1.52	-0.0088
BC	0.9470	1	0.4274	0.0998	1.79
BD	0.1668	1	0.3845	-0.5952	0.9289
CD	-0.2045	1	0.3861	-0.9699	0.5608
A^2	1.54	1	0.4747	0.6018	2.48
B^2	-0.6732	1	0.4748	-1.61	0.2680
C^2	0.8620	1	0.4748	-0.0791	1.80
D^2	5.60	1	1.15	3.31	7.88

Table A1. 6: Unpurified 72 hour compaction model coefficients.

Source	Sum of squares	df	Mean Square	F-value	p-value	
Model	20.90	9	2.32	86.24	< 0.0001	significant
A-Cell Number	0.0000	1	0.0000	0.0008	0.9779	
B-Collagen Concentration	0.0006	1	0.0006	0.0234	0.8794	
C-Fibrin Concentration	16.42	1	16.42	609.76	< 0.0001	
AB	0.0798	1	0.0798	2.96	0.0948	
AC	0.0008	1	0.0008	0.0306	0.8621	
BC	0.1295	1	0.1295	4.81	0.0357	
A^2	0.1260	1	0.1260	4.68	0.0381	
B^2	0.1243	1	0.1243	4.62	0.0394	
C^2	3.34	1	3.34	124.22	< 0.0001	
Residual	0.8616	32	0.0269			
Lack of Fit	0.1652	3	0.0551	2.29	0.0988	not significant
Pure Error	0.6963	29	0.0240			
Cor Total	21.76	41				

Table A1. 7: Lactate purified 72 hour compaction model fit.

Factor	Coefficient Estimate	df	Standard Error	95% CI Low	95% CI High
Intercept	3.04	1	0.0670	2.90	3.18
A-Cell Number	-0.0009	1	0.0335	-0.0692	0.0673
B-Collagen Concentration	0.0051	1	0.0335	-0.0631	0.0733
C-Fibrin Concentration	0.8271	1	0.0335	0.7589	0.8953
AB	0.0815	1	0.0474	-0.0149	0.1780
AC	0.0083	1	0.0474	-0.0882	0.1048
BC	-0.1039	1	0.0474	-0.2004	-0.0074
A^2	0.1146	1	0.0530	0.0067	0.2224
B^2	0.1138	1	0.0530	0.0059	0.2217
C^2	-0.5903	1	0.0530	-0.6981	-0.4824

Table A1. 8: Lactate purified 72 hour compaction model coefficients.

Source	**Sum of squares**	**df**	**Mean Square**	**F-value**	**p-value**	
Model	1206.24	3	402.08	15.76	< 0.0001	significant
A-Cell Number	77.57	1	77.57	3.04	0.0895	
B-Collagen Concentration	409.18	1	409.18	16.04	0.0003	
C-Fibrin Concentration	670.54	1	670.54	26.29	< 0.0001	
Residual	943.72	37	25.51			
Lack of Fit	361.74	9	40.19	1.93	0.0880	not significant
Pure Error	581.98	28	20.79			
Cor Total	2149.96	40				

Table A1. 9: Lactate purified Young's modulus model fit.

Factor	Coefficient Estimate	df	Standard Error	95% CI Low	95% CI High
Intercept	8.60	1	0.7896	7.00	10.20
A-Cell Number	1.80	1	1.03	-0.2910	3.89
B-Collagen Concentration	4.22	1	1.05	2.09	6.36
C-Fibrin Concentration	-5.41	1	1.05	-7.54	-3.27

Table A1. 10: Lactate purified Young's modulus model coefficients.

Source	Sum of squares	df	Mean Square	F-value	p-value	
Model	73.44	6	12.24	30.85	< 0.0001	significant
A-Cell Number	5.39	1	5.39	13.60	0.0008	
B-Collagen Concentration	0.6841	1	0.6841	1.72	0.1977	
C-Fibrin Concentration	49.49	1	49.49	124.73	< 0.0001	
AC	0.6395	1	0.6395	1.61	0.2126	
BC	0.9568	1	0.9568	2.41	0.1295	
C^2	16.27	1	16.27	41.01	< 0.0001	
Residual	13.89	35	0.3968			
Lack of Fit	2.16	6	0.3597	0.8893	0.5154	not significant
Pure Error	11.73	29	0.4045			
Cor Total	87.33	41				

Table A1. 11: Lactate purified peak active stress model fit.

Factor	Coefficient Estimate	df	Standard Error	95% CI Low	95% CI High
Intercept	-4.18	1	0.1485	-4.49	-3.88
A-Cell Number	0.4741	1	0.1286	0.2131	0.7352
B-Collagen Concentration	-0.1688	1	0.1286	-0.4299	0.0922
C-Fibrin Concentration	-1.44	1	0.1286	-1.70	-1.18
AC	-0.2308	1	0.1818	-0.6000	0.1383
BC	0.2824	1	0.1818	-0.0868	0.6515
C^2	1.26	1	0.1964	0.8590	1.66

Table A1. 12: Lactate purified peak active stress model coefficients.

APPENDIX 2: SUPPLEMENTAL DOCUMENTATION FOR WET SPINNING DEVICE ASSEMBLY AND USE

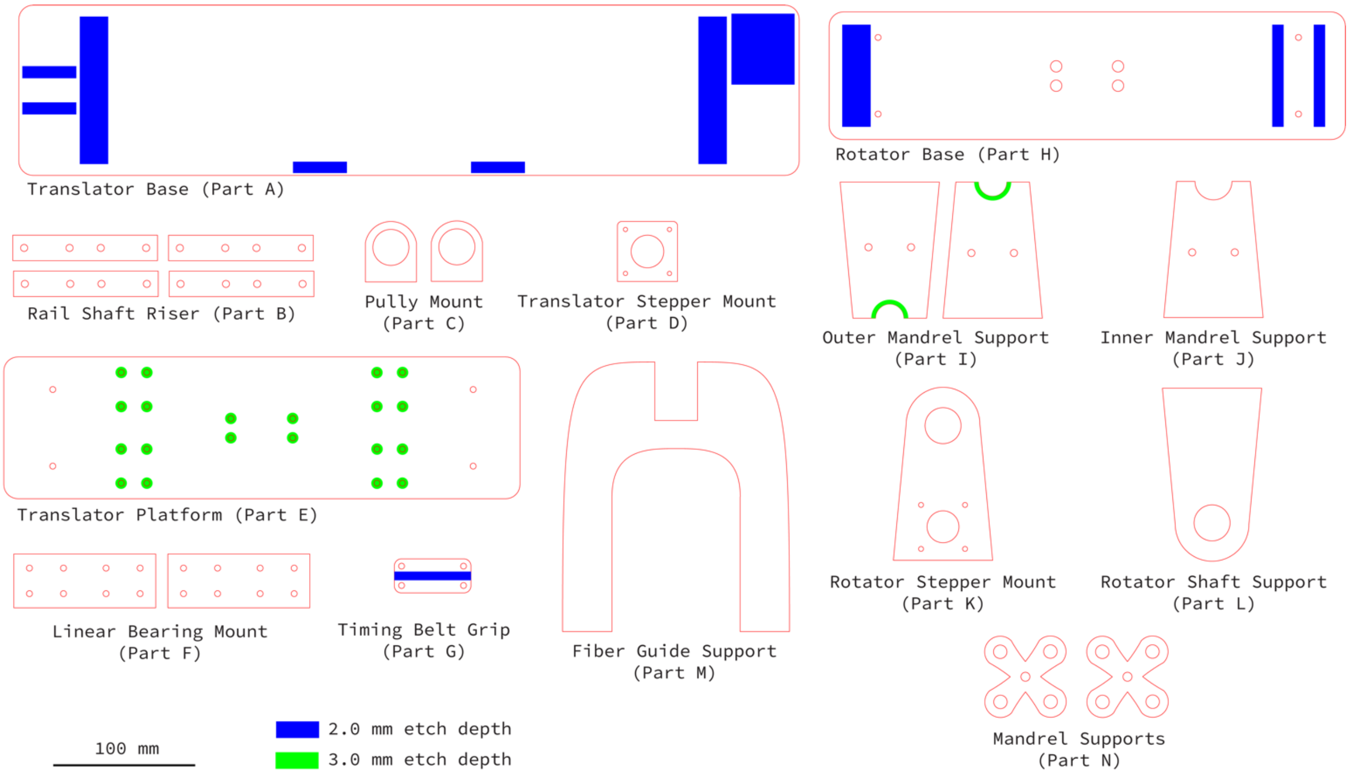

Figure A2. 1: Laser cut acrylic parts for fiber collector and mandrel . Use the provided .ai files when laser cutting.

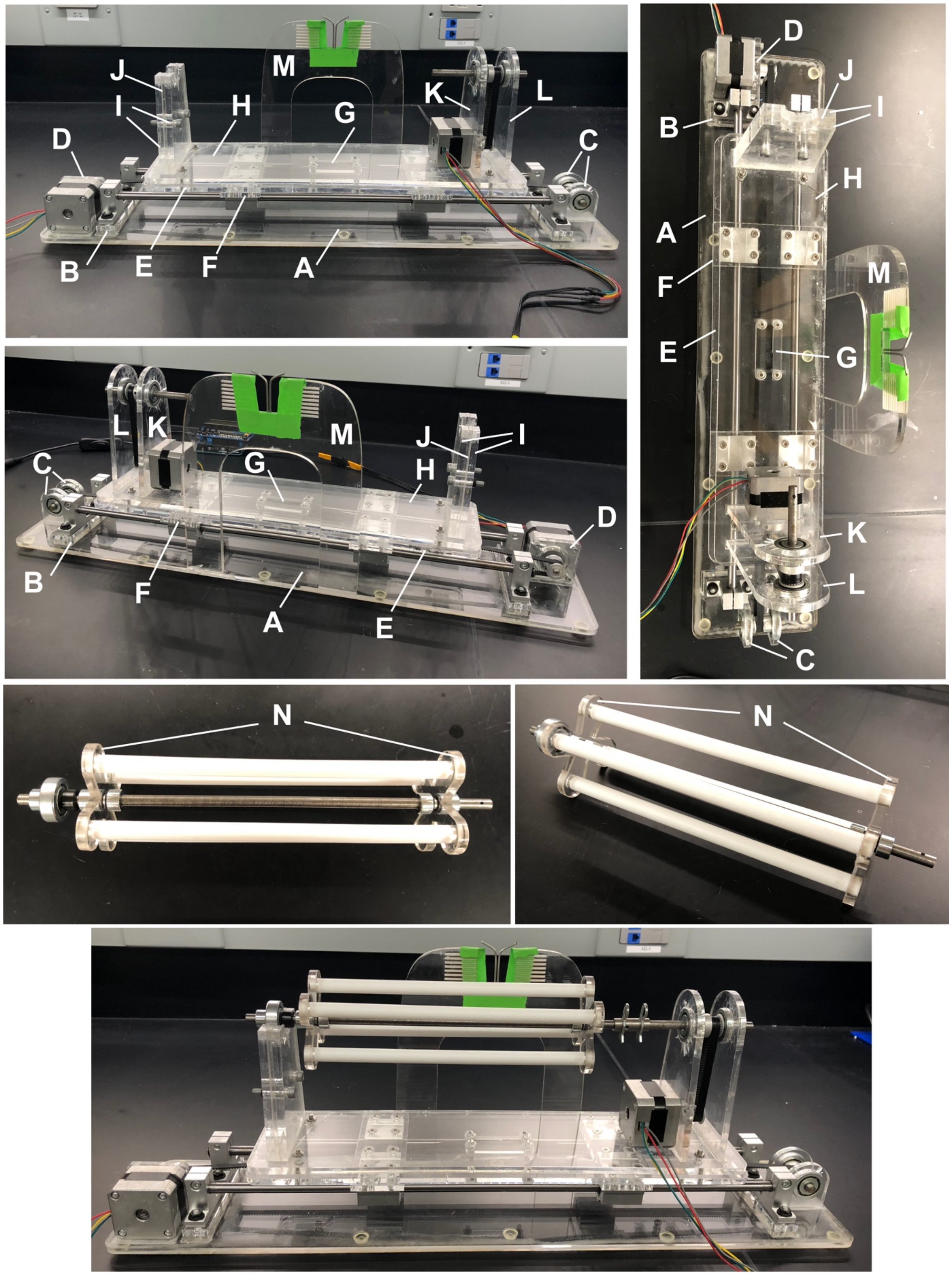

Figure A2. 2: Reference images for fiber collector and mandrel. Letters refer to Fig. S1.

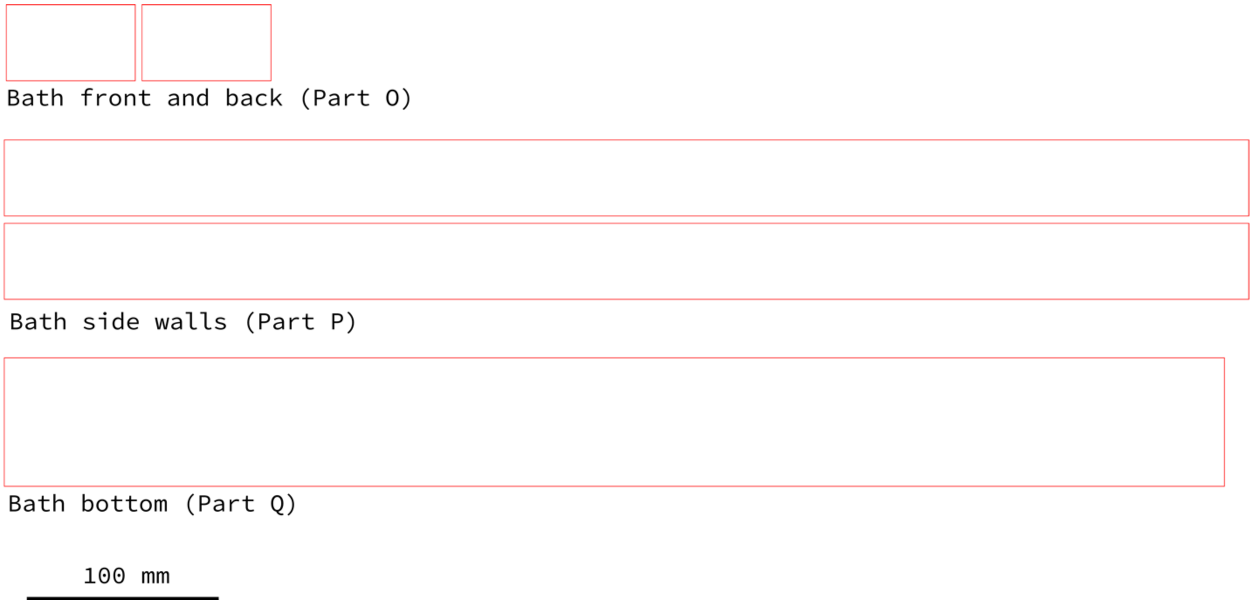

Figure A2. 3: Laser cut acrylic parts for wet spinning bath (for reference only). Use the provided .ai files when laser cutting.

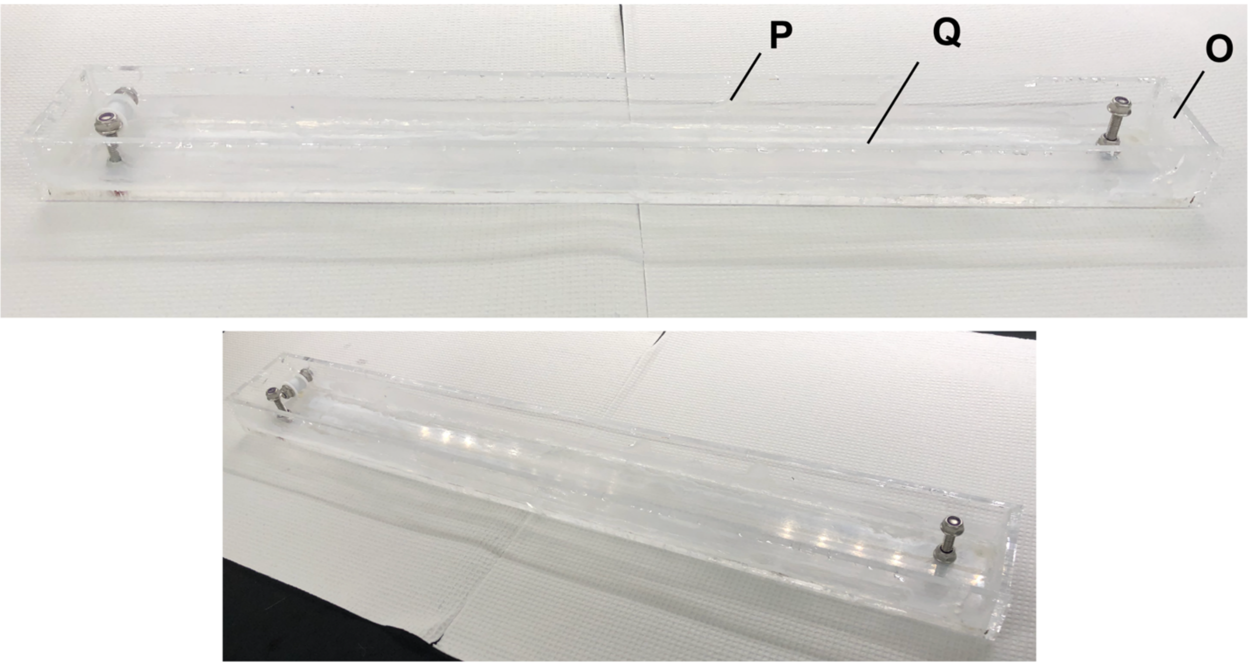

Figure A2. 4: Reference images for wet spinning bath. Letters reference Fig S3. Note that the metal fixtures visible in these images are unnecessary for the methods described in this manuscript.

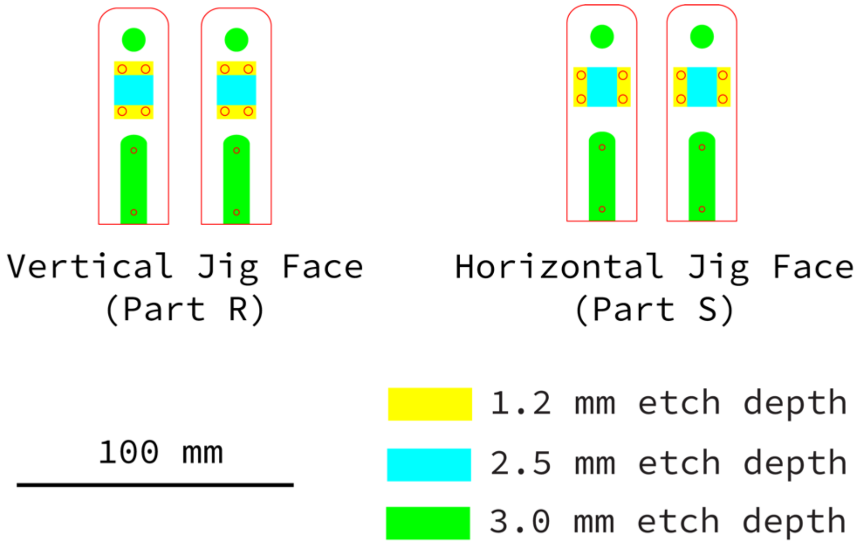

Figure A2. 5: Laser cut acrylic parts for alignment jig (for reference only). Use the provided .ai files when laser cutting.

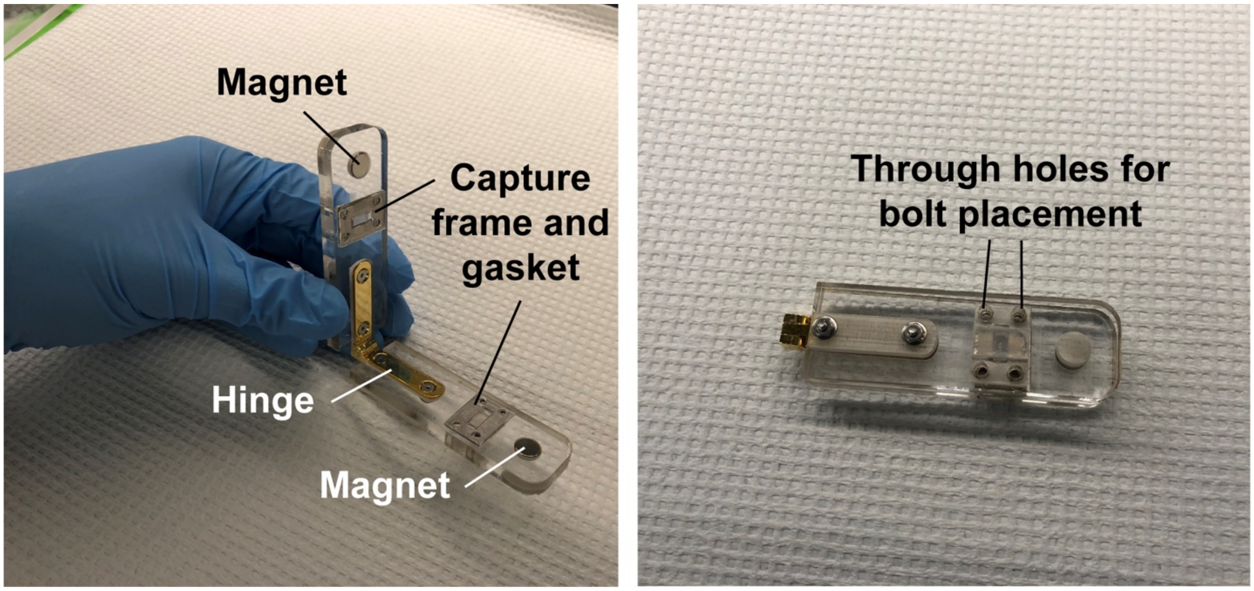

Figure A2. 6: Reference images for alignment jig.

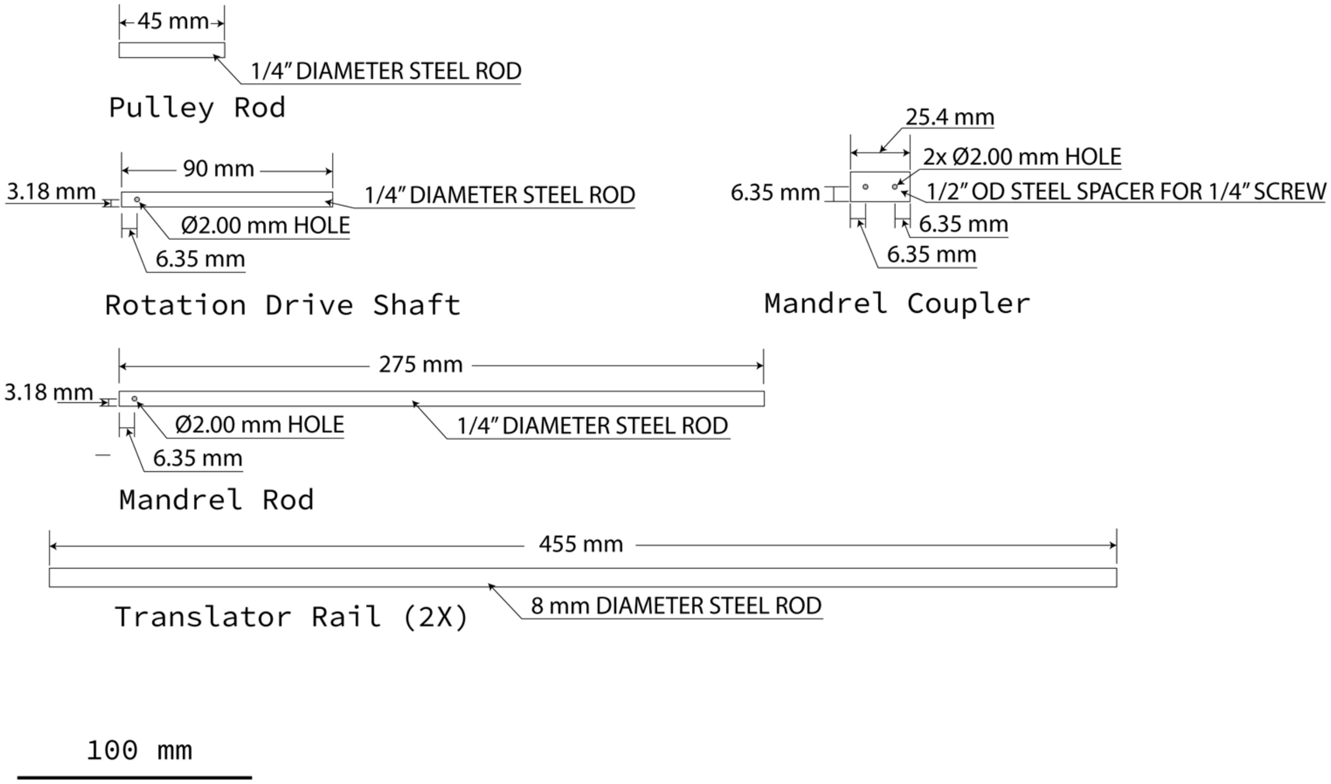

Figure A2. 7: Design plans for machined steel fiber collector parts.

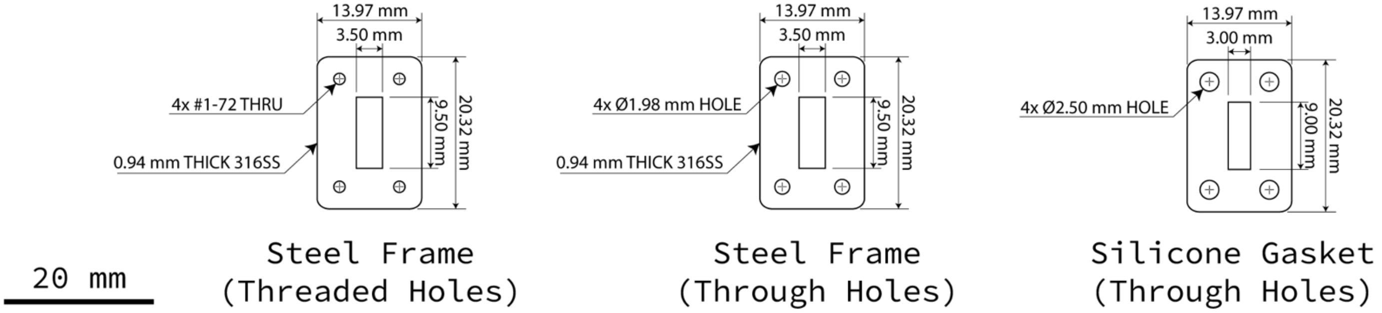

Figure A2. 8: Design plans for steel frames and silicone gaskets.

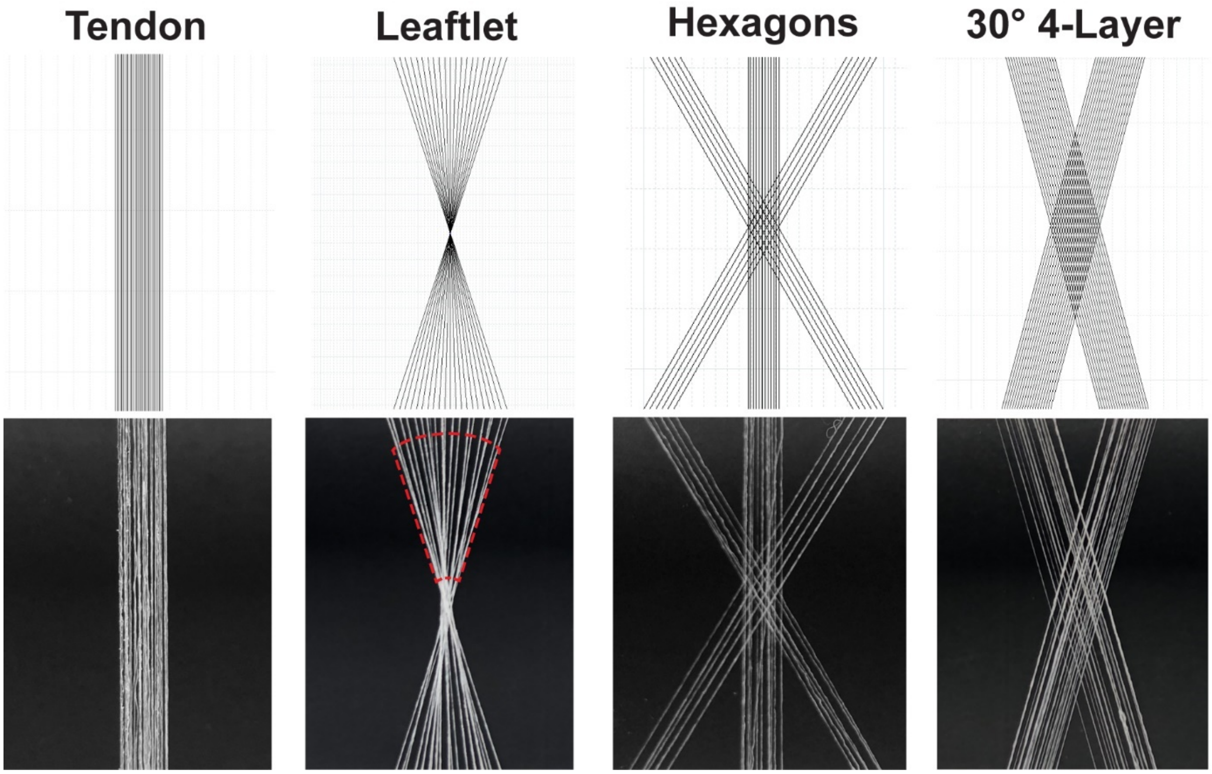

Figure A2. 9: Digital designs and gross images of assorted mesh patterns.

Part	Vendor	Part Number	Quantity
<u>Fiber Collector and Mandrel</u>			
Linear Rail Shaft Guide/Support - 8 mm diameter -SK8	Adafruit	1182	4
Linear Bearing Platform (Small) - 8mm Diameter - SC8UU	Adafruit	1179	4
Stepper motor - NEMA-17 size - 200 steps/rev, 12V 350mA	Adafruit	324	2
Adafruit Motor/Stepper/Servo Shield for Arduino v2 Kit - v2.3	Adafruit	1438	1
RGB LCD Shield Kit w/16x2 Character Display	Adarfruit	716	1
Arduino UNO R3	Arduino	A000066	1
In-line power switch for 2.1mm barrel jack	Adafruit	1125	1
9V DC 1000mA regulated switching power adapter	Adafruit	63	1
Waterproof Polarized 4-Wire Cable Set	Adafruit	744	2
Shield stacking headers for Arduino (R3 Compatible)	Adafruit	85	1
Aluminum GT2 Timing Pulley - 6mm Belt - 20 Tooth 5mm Bore	Adafruit	1251	1
Aluminum GT2 Timing Pulley - 6mm Belt - 20 Tooth 8mm Bore	Adafruit	1252	1
Timing Belt GT2 Profile - 2mm pitch - 6mm wide 1164mm long	Adafruit	1184	1
Steel Ball Bearing Plain Open for 1/4" Shaft Diameter, 1" OD, 5/16" Width	McMaster-Carr	6383K22	6
Set Screw Shaft Collar for 1/4" Diameter, Black-Oxide Steel	McMaster-Carr	9414T6	10
Linear Motion Shaft, 1055 Carbon Steel, 8mm Diameter, 600 mm Long	McMaster-Carr	6112K46	2

Mcl and XL Series Timing-Belt Pulley 1/4" Belt Width, 0.685 OD, 20 Teeth	McMaster-Carr	1375K39	2
Multipurpose 4140/4142 Alloy Steel, Rod 1/4", 2 ft	McMaster-Carr	8927K18	2
Trapezoidal Tooth Urethane Timing Belt, .080" Pitch, Trade Size 90mxl, 7.2" Outer Circle, 1/4" Wide	McMaster-Carr	1679K86	1
Tube Made of Teflon® PTFE, 3/8" OD x 1/4" ID 2 ft	McMaster-Carr	8547K11	4
Polyurethane Rubber Adhesive-Back Bumper, Domed, 7/16" OD, 13/64" High, Durometer 50A, Clear	McMaster-Carr	95495K673	1
Oil-Resistant Buna-N O-Ring, 1/16 Fractional Width, Dash Number 008	McMaster-Carr	9452K16	1
18-8 Stainless Steel Unthreaded Spacer, 1/2" OD, 1" Long, for 1/4" Screw Size	McMaster-Carr	92320A669	1
18-8 Stainless Steel Hairpin Cotter Pin, for 3/8" to 1/2" Clevis Diameter, 5/64" Wire Diameter	McMaster-Carr	92391A135	1
Class 12.9 Socket Head Cap Screw, Zinc-Coated Alloy Steel, M5 Thread, 25mm Long, .8mm Pitch	McMaster-Carr	95263A402	10
Uncoated Class 8 Steel Serrated-Flange Locknut M5x0.8 Thread, 11.2mm Flange Diameter, 4.3mm Overall Height	McMaster-Carr	94920A300	10
Coated Alloy Steel Socket Head Cap Screw M3 Thread, 10 mm Long	McMaster-Carr	91274A105	8
18-8 Stainless Steel Low-Profile Socket Head Screws M4 x 0.7 mm Thread, 16 mm Long	McMaster-Carr	92855A416	24
Type 18-8 Stainless Steel Thin Hex Nut - DIN 439B M4x0.7 Thread Size, 7mm Wide, 2.2mm High	McMaster-Carr	90710A035	8
Alignment Jig			
HIGHPOINT Side Rail Hinge Solid Brass	Woodcraft	161694W	2
316 Stainless Steel Hex Drive Flat Head Screw 82 Degree Countersink Angle, 2-56 Thread Size, 3/8" Long	McMaster-Carr	90585A120	8
18-8 Stainless Steel Hex Nut 2-56 Thread Size	McMaster-Carr	91841A003	8
316 Stainless Steel Washer for Number 2 Screw Size, 0.094" ID, 0.25" OD	McMaster-Carr	90107A003	8
High-Pull Rare Earth Magnetic Disc **Neodymium, 0.1" Thick, 1/4"** Diameter	McMaster-Carr	5862K52	4
Collection Frames			
18-8 Stainless Steel Socket Head Screw 1-72 Thread Size, 1/4" Long	McMaster-Carr	92196A066	4/frame set

Table A2. 1: List of required parts for fiber collector and wet spinning bath, alignment jig, and collection frames.